On the evolution of gas clouds exposed to AGN radiation I. Three-dimensional radiation hydrodynamic simulations

doi: 10.1093/mnras/stu1271

Monthly Notices of the ROYAL ASTRONOMICAL SOCIETY
MNRAS **443,** 2018–2048 (2014) doi:10.1093/mnras/stu1271

On the evolution of gas clouds exposed to AGN radiation – I. Three-dimensional radiation hydrodynamic simulations

D. Namekata,* M. Umemura and K. Hasegawa
Center for Computational Sciences, University of Tsukuba, 1-1-1 Tennodai, Tsukuba 305-8577 Ibaraki, Japan

Accepted 2014 June 23. Received 2014 June 23; in original form 2014 February 10

ABSTRACT

We perform three-dimensional radiation hydrodynamic simulations of uniform dusty gas clouds irradiated by an active galactic nucleus (AGN) to investigate the dependence of evolution of clouds on the ionization parameter $\mathcal{U}$ and the Strömgren number $\mathcal{N}_{\rm S}$. We find that the evolution can be classified into two cases depending on $\mathcal{U}$. In low $\mathcal{U}$ cases ($\mathcal{U} \approx 10^{-2}$), the evolution is mainly driven by photoevaporation. An approximately spherically symmetric evaporation flow with velocity of $100-150\,{\rm km\,s^{-1}}$ is launched from the irradiated face. The cloud is compressed by a D-type shock losing its mass due to photoevaporation and is finally turned into a dense filament by $t \lesssim 1.5t_{\rm sc}$. In high $\mathcal{U}$ cases ($\mathcal{U} \approx 5 \times 10^{-2}$), radiation pressure suppresses photoevaporation from the central part of the irradiated face, reducing photoevaporation rate. An evaporation flow from the outskirts of the irradiated face is turned into a high-velocity ($\lesssim$500 km s^{-1}) gas wind because of radiation pressure on dust. The cloud is swept by a radiation pressure-driven shock and becomes a dense gas disc by $t \approx t_{\rm sweep}$. Star formation is expected in these dense regions for both cases of $\mathcal{U}$. We discuss the influences of the AGN radiation on the clumpy torus. A simple estimate suggests that the clumps are destroyed in time-scales shorter than their orbital periods. For the clumpy structure to be maintained over long period, the incident radiation field needs to be sufficiently weaken for most of the clumps, or, some mechanism that creates the clumps continuously is needed.

Key words: hydrodynamics – radiative transfer – methods: numerical – ISM: clouds – galaxies: active.

1 INTRODUCTION

Active galactic nuclei (AGNs) are one of the most brightest objects in the Universe and their bolometric luminosities can be as high as $\approx 10^{47}$ erg s^{-1} (e.g. Croom et al. 2002; Dietrich & Hamann 2002). Most of their radiation is emitted in the optical/ultraviolet (UV) wavelength as well as in the X-ray wavelength and is enable to ionize and heat surrounding interstellar medium (ISM) or intragalatic medium (IGM). Therefore, radiation from the AGNs, along with relativistic jets, are believed to have a great impact on evolution and formation of galaxies. One of pieces of indirect evidence supporting this is provided by a comparison between theoretical predictions of galaxy luminosity function and observational data (e.g. Benson et al. 2003).

The activities of AGNs are maintained through mass accretion on to supermassive black holes (SMBHs). The accreting matter is considered to flow from a dusty molecular torus which surrounds the SMBH. Its existence is suggested in the unified scheme of AGNs (e.g. Antonucci 1993; Urry & Padovani 1995) and is supported by indirect observational evidence such as polarized light from Seyfert galaxies (e.g. Young et al. 1995, 1996; Smith et al. 2002, 2004, 2005). A theoretical consideration (Krolik & Begelman 1988) and spectral energy distribution (SED) modellings of emission from the AGN torus (Nenkova, Ivezić & Elitzur 2002; Dullemond & van Bemmel 2005; Hönig et al. 2006; Nenkova et al. 2008a,b) suggest that the AGN torus consists of a number of dense gas clumps. This is called the clumpy torus model. The physical properties of the gas clumps and the maintenance mechanism of the clumpy structure are currently unknown. The molecular gas in the AGN tori also must come from outer parts of host galaxies such as bulges and galactic discs or from outside the host galaxies. Several scenarios are proposed for mass supply process towards the galactic centres. In large scales ($r \gtrsim 1$ kpc), (1) tidal torque driven by major and the minor merger (e.g. Hernquist 1989; Barnes & Hernquist 1991; Mihos & Hernquist 1996; Taniguchi 1999; Kendall, Magorrian & Pringle 2003; Saitoh & Wada 2004; Cattaneo et al. 2005), (2) non-axisymmetric perturbations by stellar bars or spiral arms (e.g. Athanassoula 1992), (3) viscous torque on giant molecular clouds (e.g. Fukunaga 1983, 1984a,b), (4) magnetic stress

*E-mail: namektds@gmail.com

by the magnetic rotational instability (e.g. Milosavljević 2004) is suggested. In the outer part of AGN torus (a few pc $\lesssim r \lesssim$ several tens of pc), Wada (2002) and Wada, Papadopoulos & Spaans (2009) demonstrated numerically that supernova-driven turbulence enhances mass inflow towards the centre (see also Schartmann et al. 2009, 2010). Such a process is investigated semi-analytically by Kawakatu & Wada (2008, 2009). Krolik & Begelman (1988) suggested that kinetic viscosity by clump–clump collisions induces angular momentum transfer in the AGN torus and drives inward flow. A possibility of mass supply by gas clumps is also investigated for our Galaxy (e.g. Sanders 1998; Nayakshin, Cuadra & Springel 2007; Bonnell & Rice 2008; Wardle & Yusef-Zadeh 2008; Hobbs & Nayakshin 2009; Namekata & Habe 2011). However, it is not well understood how these gas supply processes (at different scales) are affected by the AGN when it increases its activity. This question must be related to maintenance mechanism of the AGN activity.

In this context, Wada (2012) performed recently 3D radiation hydrodynamic (RHD) simulations of a circumnuclear gas disc (its size is $r \lesssim 30$ pc) in an AGN hosting galaxy taking into account X-ray heating and radiation pressure on gas. He showed that a geometrically and optically thick torus can be naturally formed by hydrodynamic interaction between the back-flow of a biconical gas outflow, which is launched from the inner part of the disc ($r \leq$ a few pc) in a vertical direction by the radiation force, and the disc gas. He also showed that the gas accretion is not stopped completely by the radiation feedback. Because the gas accretion rate to the central parsec is one order magnitude smaller than the gas accretion rate required to maintain the AGN luminosity, he suggested that the AGN activity is intrinsically intermittent or that there are other mechanisms that enhance the mass accretion to the centre.

A complementary approach to understand the effects of the AGN radiation on the gas supply processes is to investigate evolution of optically thick dense clouds in detail, because they are expected to play a main role in gas supply process even under strong radiation field. Especially, survival time and star formation properties (initial mass function and star formation rate) of such clouds are quite important information, since the survival time can be related to the efficiency of angular momentum transfer and star formation and stellar feedback affect not only the gravitational stability of the gas clouds but also that of the galactic gas disc by consuming gas or inputting energy. It is difficult to investigate these important properties by global simulations.

Evolution of an cloud irradiated by an AGN has been studied by several authors. Early studies investigated the effects of radiation pressure on line-emitting clouds in QSOs by ignoring hydrodynamic effects entirely (e.g. Williams 1972; Mathews 1974, 1976, 1982, 1986; McKee & Tarter 1975; Weymann 1976; Mathews & Blumenthal 1977; Blumenthal & Mathews 1979; Krolik, McKee & Tarter 1981). Pier & Voit (1995) investigated hydrodynamic properties of photoevaporation wind from AGN-irradiated dusty gas clouds by solving the steady-state wind equation assuming spherical symmetry. They showed that radiation pressure force suppresses the photoevaporation by confining the evaporation flow to near the cloud surface if thermal sputtering of dust is inefficient and that the dusty clouds on eccentric orbits can penetrate well inside the inner edge of the torus because the photoevaporation time is longer than the orbital period. Recently, Schartmann, Krause & Burkert (2011) performed two-dimensional RHD simulations of a dusty gas cloud falling towards the galactic centre ignoring self-gravity and showed that the clouds can be destroyed by hydrodynamic instabilities generated by the complex interplay between the radiation pressure and the ram pressure. Hocuk & Spaans (2010, 2011) showed numerically the possibility that the X-ray heating from the AGN makes the initial mass function (IMF) top heavy. More recently, Proga et al. (2014) investigated the dependences of the evolution of an irradiated cloud on the properties of type of opacity (absorption dominated or scattering dominated) and the optical thickness of the cloud by performing two-dimensional RHD simulations taking into account both absorption and scattering, but ignoring photoionization and self-gravity.

As already mentioned, a large fraction of the AGN radiation is emitted in the optical/UV wavelength. Most of these photons must be absorbed by neutral atomic hydrogen in an irradiated face of gas clouds and thereby photoevaporation should occur. Because an ionized gas has temperature of $(1-3) \times 10^4$ K, evaporation must be stronger than thermal expansion driven by X-ray heating shown in Hocuk & Spaans (2010, 2011). Thus, photoevaporation due to H I ionization can play an important role in evolution of the gas clouds. In addition, radiation pressure also plays a great impact on evolution of the gas clouds as already shown by Schartmann et al. (2011). However, it is not clear how these processes affect evolution of the gas clouds when they operate simultaneously, because no hydrodynamic simulation that includes both processes has been carried out. Therefore, in this paper, we perform 3D RHD simulations of gas clouds exposed to an AGN taking into account non-equilibrium chemistry of e^-, p, H_I, H_2 and dust, in order to study combined effects of the photoevaporation and the radiation pressure on the evolution of the clouds without enforcing spherical symmetry. Especially, we clarify the dependences of the survival times of the clouds on the optically thickness of the cloud and the incident radiation field strength, because such information can be useful when we consider the gas supply processes. Effects of star formation and stellar feedbacks are investigated in a subsequent paper.

This paper is organized as follows. In Section 2, we explain our models and basic assumptions. In Section 3, we describe the detail of the numerical methods. In Section 4, we show our numerical results. Evolution of irradiated clouds is explained here and we show the dependence of survival time on the radiation field strength and the optical depth of the clouds. In Section 5, we discuss star formation in the clouds and give some implications for gas clumps in AGN tori. Finally, we summarize this paper in Section 6.

2 MODEL

2.1 Basic assumptions and model parameters

Fig. 1 shows a schematic illustration of our model. To make the analysis easy, we assume that a gas cloud is an initially uniform sphere and consists of neutral molecular hydrogen. The gas cloud is placed at the distance of r from the AGN and r is chosen so that the radiation is almost plane-parallel. The gas cloud is initially at rest. The gravitational potential of the host galaxy and the SMBH is not considered for simplicity except for model SC00-3D-ff which is explained later. We do not take into account star formation and stellar feedback processes in the gas cloud. The simulation is started when the AGN radiation is turned on. Such an abrupt increase of luminosity will occur when the AGN just becomes active or when the gas cloud moves in the clumpy torus from a shadow region, where most of the AGN radiation is shielded by other gas clouds, to a region near the surface of the torus. We numerically follow

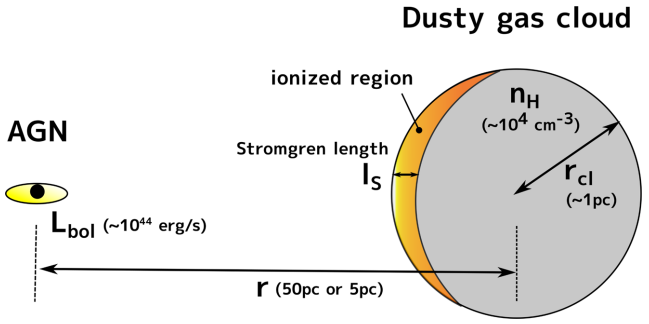

Figure 1. A schematic illustration of our model. The system is described by four parameters: the cloud radius $r_{\rm cl}$, the hydrogen number density of the cloud $n_{\rm H}$, the distance between the AGN and the centre of the cloud r, and the bolometric luminosity of the AGN $L_{\rm bol}$. Typical values for the parameters assumed in this study are also shown in the parentheses. The surface layer to a depth of the Strömgren length, $l_{\rm S}$, at the irradiated side of the cloud will be photoionized.

the evolution of the cloud taking into account self-gravity of gas and absorption of direct radiation from AGN, until the numerical timestep becomes prohibitively small. Scattering of photons and transfer of diffuse (scattered and re-emitted) photons are not taken into account in this study.

The basic parameters that control the system are the cloud radius $r_{\rm cl}$, the hydrogen number density of the cloud $n_{\rm H}$, the distance of the cloud centre from the AGN r and the bolometric luminosity of the AGN $L_{\rm bol}$ (see Fig. 1). Thus, the number of free parameters is 4. It is not practical to quest the entire four-dimensional parameter space. Instead, we investigate the dependence on two parameters that we consider important, the ionization parameter $\mathcal{U}$ and the Strömgren number $\mathcal{N}_{\rm S}$. They are defined by

$$\mathcal{U} = \frac{F_{\rm ion}}{cn_{\rm H}}, \tag{1}$$

$$\mathcal{N}_{\rm S} = \frac{2r_{\rm cl}}{l_{\rm S}}, \tag{2}$$

where $F_{\rm ion}$ is the number flux of ionizing photon and is defined as

$$F_{\rm ion} = \frac{1}{4\pi r^2}\int_{\nu_{\rm L}}^{\infty}\frac{L_{\nu'}}{h\nu'}\,{\rm d}\nu', \tag{3}$$

where L_ν is the monochromatic luminosity of the AGN, h is the Planck constant and $\nu_{\rm L}$ is the frequency at the Lyman limit. c is the speed of light, $l_{\rm S}$ is the Strömgren length (see Fig. 1) defined by

$$l_{\rm S} = \frac{F_{\rm ion}}{\alpha_{\rm B} n_{\rm H}^2}, \tag{4}$$

where $\alpha_{\rm B} \approx 2.59 \times 10^{-13}\,{\rm cm^3\,s^{-1}}$ is the case B recombination coefficient at the gas temperature of 10^4 K (Hui & Gnedin 1997). The Strömgren number $\mathcal{N}_{\rm S}$ represents what fraction of gas in the cloud is photoionized and therefore corresponds to the *effective* optical depth of the gas cloud for the photoionization of $H_{\rm I}$, whereas the ionization parameter $\mathcal{U}$ is the ratio of the photon number density to the hydrogen number density and is an indicator of the strength of incident radiation fields. The latter can be understood by considering the ratio of the radiation energy density to the thermal energy density in a fully ionized region which are formed at an irradiated surface of the gas cloud. The thermal energy density in the fully ionized gas is given by

$$e_{\rm th} = \frac{3}{2}(n_{\rm e}+n_{\rm p})k_{\rm B}T_{\rm gas} = 3n_{\rm H}k_{\rm B}T_{\rm gas}. \tag{5}$$

On the other hand, the radiation energy density is given by

$$e_{\rm rad} = \frac{L_{\rm bol}}{4\pi r^2 c}. \tag{6}$$

The ratio of both values is written as

$$\frac{e_{\rm rad}}{e_{\rm th}} = \frac{L_{\rm bol}}{4\pi r^2 c n_{\rm H}}\frac{1}{3k_{\rm B}T_{\rm gas}} \tag{7}$$

$$\approx \frac{1\,{\rm eV}}{3k_{\rm B}T_{\rm gas}}\left(\frac{\mathcal{U}}{1.5\times10^{-2}}\right)\left(\frac{h\nu_{\rm ion}}{44\,{\rm eV}}\right)\left(\frac{{\rm BC_{ion}}}{1.5}\right), \tag{8}$$

where $h\nu_{\rm ion}(\equiv h\int_{\nu_{\rm L}}^{\infty}\nu' L_{\nu'}\,{\rm d}\nu'/\int_{\nu_{\rm L}}^{\infty}L_{\nu'}\,{\rm d}\nu')$ is the mean-energy of ionizing photon and ${\rm BC_{ion}}(\equiv L_{\rm bol}/L_{\rm ion})$ is the bolometric correction factor. The normalizations for $h\nu_{\rm ion}$ and ${\rm BC_{ion}}$ are based on the adopted SED (see Section 2.2 and Table 2). Thus, the ratio $e_{\rm rad}/e_{\rm th}$ is proportional to $\mathcal{U}$. In the fully ionized gas, the gas temperature is in the range of $1-3\times10^4$ K and can be considered to be a constant.[1] Therefore, higher $\mathcal{U}$ directly implies stronger radiation fields. Similar conclusion can be obtained by an order estimation of the force balance in the fully ionized region. The pressure-gradient acceleration is of the order of

$$|\boldsymbol{a}_{\rm p}| = \frac{\nabla p}{\rho} \sim \frac{p}{\rho l_{\rm S}} \tag{9}$$

$$\approx \frac{2n_{\rm H}k_{\rm B}T_{\rm gas}}{m_{\rm H}n_{\rm H}l_{\rm S}}. \tag{10}$$

The order of the radiative acceleration can be estimated as

$$|\boldsymbol{a}_{\rm rad}| \sim \frac{L_{\rm bol}}{4\pi r^2 c}\frac{1}{m_{\rm H}n_{\rm H}l_{\rm S}}. \tag{11}$$

The ratio becomes

$$\frac{|\boldsymbol{a}_{\rm rad}|}{|\boldsymbol{a}_{\rm p}|} = \frac{L_{\rm bol}}{4\pi r^2 c n_{\rm H}}\frac{1}{2k_{\rm B}T_{\rm gas}} \tag{12}$$

$$\approx \frac{1\,{\rm eV}}{2k_{\rm B}T_{\rm gas}}\left(\frac{\mathcal{U}}{1.5\times10^{-2}}\right)\left(\frac{h\nu_{\rm ion}}{44\,{\rm eV}}\right)\left(\frac{{\rm BC_{ion}}}{1.5}\right). \tag{13}$$

Again, the ratio is proportional to $\mathcal{U}$. According to these order estimation, it is expected that the radiation pressure becomes important when $\mathcal{U}$ is larger than $\approx$0.05.

In this paper, we investigate two cases of $\mathcal{U}$ (5.2×10^{-2} and 1.3×10^{-2}). This choice is motivated by the discussion above, that is, we expect that the radiation pressure plays an more important role in the evolution of the cloud for the case of $\mathcal{U}=5.2\times10^{-2}$ than $\mathcal{U}=1.3\times10^{-2}$. Thus, this range of $\mathcal{U}$ is sufficient to examine relative importance of the photoevaporation and the radiation pressure (but, a larger $\mathcal{U}$ case is also investigated in this study; see next paragraph). For each of $\mathcal{U}$, three different values (5, 10 and 20) of $\mathcal{N}_{\rm S}$ are examined. In reality, there are more optically thick clouds than $\mathcal{N}_{\rm S}=20$. As we will discuss in Section 5.4, gas clumps in AGN tori can have $\mathcal{N}_{\rm S}>10^4$. Unfortunately, it is impossible to numerically resolve such extremely optically thick clouds in the current computational power. Therefore, we use the results of these runs to investigate the dependence of the cloud evolution on the optical depth and attempt to predict the fates of larger $\mathcal{N}_{\rm S}$ clouds based on the derived dependence. For the given $\mathcal{U}$ and $\mathcal{N}_{\rm S}$, an arbitrary realization is possible. In this study, we

[1] Note that this temperature range is true only for the small range of $\mathcal{U}$ investigated in this study ($\mathcal{U}\approx0.01-0.2$; see Table 1). The maximal temperature that fully ionized gas can reach is the Compton temperature ($\sim10^7$ K).

Table 1. Simulation runs.

Model family	Model name	$\mathcal{U}$	$\mathcal{N}_S$[a]			L_{bol}	r	n_H	r_{cl}	M_{cl}	Ω	r_J^b
			Near	Centre	Far	(erg s^{-1})	(pc)	(cm^{-3})	(pc)	($M_\odot$)	(sr)	
Low-$\mathcal{U}$	L05	1.3×10^{-2}	5.085	5.111	5.136	1.25×10^{44}	50	10^4	0.125	2.022	1.96×10^{-5}	23.9
	L10	1.3×10^{-2}	10.12	10.22	10.32	1.25×10^{44}	50	10^4	0.250	16.18	7.85×10^{-5}	5.98
	L20	1.3×10^{-2}	20.04	20.44	20.85	1.25×10^{44}	50	10^4	0.500	129.4	3.14×10^{-4}	1.50
High-$\mathcal{U}$	H05	5.2×10^{-2}	5.009	5.111	5.213	5.0×10^{44}	50	10^4	0.5	129.4	3.14×10^{-4}	1.50
	H10	5.2×10^{-2}	9.816	10.22	10.63	5.0×10^{44}	50	10^4	1.0	1035	1.26×10^{-3}	0.374
	H20	5.2×10^{-2}	18.83	20.44	22.11	5.0×10^{44}	50	10^4	2.0	8284	5.03×10^{-3}	0.093
SC	SC00-3D	0.17	12.10	18.92	27.24	1.04×10^{44}	5	6×10^4	1.0	6213	0.127	0.062

[a]We show the Strömgren number $\mathcal{N}_S$ at three different positions in a cloud. The subentries 'near', 'centre' and 'far' correspond to the positions at distances of $r - r_{cl}$, r and $r + r_{cl}$ from the AGN, respectively. A small difference between $\mathcal{N}_S$ at three positions means that the incident radiation field is effectively plane-parallel.

[b]The ratio of total thermal energy to gravitational energy ($r_J \equiv E_{th}/|E_{grv}|$, where $E_{th} = \frac{1}{\gamma_{eff}-1}\frac{k_B T_{gas}}{\mu m_H} M_{cl}$ and $E_{grv} = -\frac{3}{5}\frac{GM_{cl}^2}{r_{cl}}$). For a critically stable cloud, r_J is written as $\frac{5}{\pi^2 \gamma_{eff}(\gamma_{eff}-1)}$ and $r_J = 0.91$ if the cloud consists of a molecular hydrogen only ($\gamma_{eff} = 7/5$). If r_J of a cloud is much smaller than unity, the cloud must be bounded by its self-gravity. As a reference, we show the Jeans length for typical parameter values: $\lambda_J \approx 1.34\,\mathrm{pc}\,(\gamma_{eff}/\frac{7}{5})^{1/2}(\mu/2)^{-1/2}(T_{gas}/10^2\,\mathrm{K})^{1/2}(n_H/10^4\,\mathrm{cm}^{-3})^{-1/2}$.

assume that $n_H = 10^4\,\mathrm{cm}^{-3}$ and $r = 50\,\mathrm{pc}$ for all the models except model SC00-3D. For $\mathcal{U} = 1.3 \times 10^{-2}$ and 5.2×10^{-2}, we assume $L_{bol} = 1.25 \times 10^{44}$ and $5 \times 10^{44}\,\mathrm{erg\,s^{-1}}$, respectively. Then, r_{cl} is uniquely determined if $\mathcal{N}_S$ is given. The choice of n_H is intended to mimic physical conditions similar to molecular cores in the Galaxy. Table 1 summarizes the simulation runs. As shown in the table, the Jeans ratio r_J of models L05, L10, L20 and H05 are larger than unity, and therefore, they are initially stable for their self-gravity. We note that n_H can affect the evolution of the clouds independently of M_{cl}, since the thermodynamic nature of the gas depends on n_H.

Model SC00-3D in Table 1 is the run with almost the same calculation conditions as the run SC00 in Schartmann et al. (2011, see table 2 in their paper) and has a more higher $\mathcal{U}$ than high-$\mathcal{U}$ models. The major differences between ours and theirs are as follows. First, ours is a 3D simulation, while their simulation is 2D. Therefore, the dynamical response to the tidal force by the external gravities is expected to be different between ours and theirs. Secondly, the self-gravity of gas and the photoionization are taken into account in our simulation. On the other hand, these effects are not considered in their study. This also may affect the evolution of the cloud. The comparison between SC00-3D and SC00 will be useful to investigate effects of these differences on the evolution of cloud. The detail of the simulation conditions is explained in Section 4.4.

In order to compare different runs, it may be useful to use time normalized by a characteristic time-scale. Here, we introduce two characteristic time-scales. Since the irradiated gaseous layer of the gas cloud is expected to expand in the direction of the AGN, one of characteristic time-scale can be the sound (rarefaction wave) crossing time t_{sc} defined as

$$t_{sc} = \frac{2r_{cl}}{c_s^{irr}} = 7 \times 10^4\,\mathrm{yr}\left(\frac{r_{cl}}{1\,\mathrm{pc}}\right)\left(\frac{c_s^{ion}}{28.75\,\mathrm{km\,s^{-1}}}\right)^{-1}, \quad (14)$$

where c_s^{irr} is the sound speed of the irradiated gas layer. Here, we normalize it by the sound speed of fully ionized pure hydrogen gas of $T_{gas} = 30\,000\,\mathrm{K}$. Another can be the sweeping time of the shocked layer which is formed at the irradiated side of the cloud due to the back reaction of the photoevaporation flow or the radiation pressure (see Section 4). If we assume that (i) only the radiation pressure force is important, and (ii) all the radiation is absorbed in this shocked layer, the motion of the shocked layer can be modelled as $\mathrm{d}(\rho S R v)/\mathrm{d}t = |\boldsymbol{F}_{rad}|S$, where S is surface area, R is the position of the layer, v is the velocity of the layer, $|\boldsymbol{F}_{rad}| = L_{bol}/(4\pi r^2 c)$ is the radiation pressure force acting on the unit area. In this razor-thin approximation, the velocity of the shocked layer is

$$\begin{aligned} v_{sh}^{app} &= \sqrt{\frac{|\boldsymbol{F}_{rad}|}{\rho}} \\ &= 9.4\,\mathrm{km\,s^{-1}}\left(\frac{L_{bol}}{1.25 \times 10^{44}\,\mathrm{erg\,s^{-1}}}\right)^{0.5} \\ &\quad \times \left(\frac{r}{50\,\mathrm{pc}}\right)^{-1}\left(\frac{n_H}{10^4\,\mathrm{cm}^{-3}}\right)^{-0.5}. \end{aligned} \quad (15)$$

Using the approximate relation $L_{bol}/(4\pi r^2) \approx \mathrm{BC}_{ion} h \nu_{ion} \mathcal{U}$, we can rewrite equation (15) into

$$v_{sh}^{app} = \sqrt{\frac{\mathrm{BC}_{ion} h \nu_{ion} \mathcal{U}}{m_H}}. \quad (16)$$

Thus, v_{sh}^{app} is a function of $\mathcal{U}$ only for a fixed SED. The sweeping time is given by

$$\begin{aligned} t_{sweep} &= \frac{2r_{cl}}{v_{sh}^{app}} \\ &= 2.13 \times 10^5\,\mathrm{yr}\left(\frac{r_{cl}}{1\,\mathrm{pc}}\right)\left(\frac{L_{bol}}{1.25 \times 10^{44}\,\mathrm{erg\,s^{-1}}}\right)^{-0.5} \\ &\quad \times \left(\frac{r}{50\,\mathrm{pc}}\right)\left(\frac{n_H}{10^4\,\mathrm{cm}^{-3}}\right)^{0.5}. \end{aligned} \quad (17)$$

2.2 AGN SED

We assume the SED given by Nenkova et al. (2008a) except for SC00-3D models,

$$\lambda F_\lambda \propto \begin{cases} (\lambda/\lambda_h)^{1.2}, & \lambda < \lambda_h \\ 1, & \lambda_h \le \lambda \le \lambda_u \\ (\lambda/\lambda_u)^{-p}, & \lambda_u \le \lambda \le \lambda_{RJ} \\ (\lambda_u/\lambda_{RJ})^p(\lambda/\lambda_{RJ})^{-3}, & \lambda_{RJ} \le \lambda \end{cases}, \quad (18)$$

where $\lambda_h = 0.01\,\mu\mathrm{m}$, $\lambda_u = 0.1\,\mu\mathrm{m}$, $\lambda_{RJ} = 1\,\mu\mathrm{m}$ and $p = 0.5$. For SC00 model, we use the same SED as used in Schartmann et al.

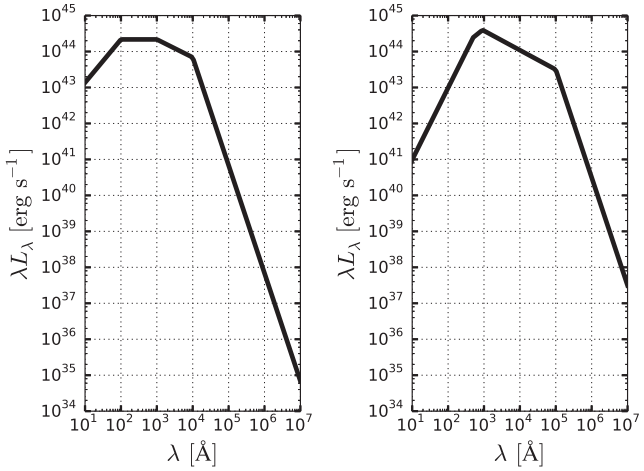

Figure 2. Model SEDs of AGN for $L_{\rm bol} = 10^{45}$ erg s^{-1}. The left-hand panel shows the model SED by Nenkova et al. (2008a) and the right-hand panel shows the one by Schartmann et al. (2011).

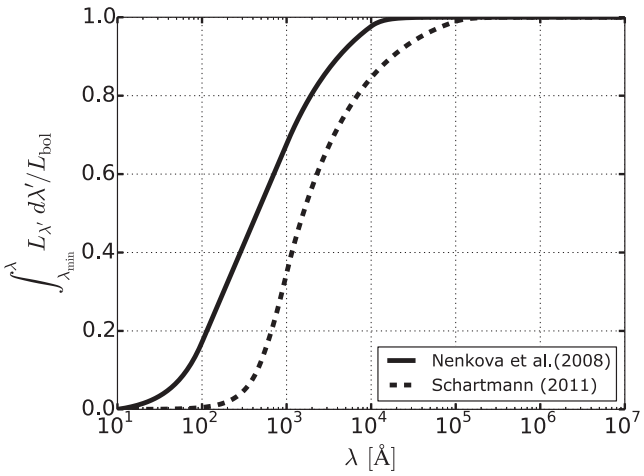

Figure 3. $\int_{\lambda_{\rm min}}^{\lambda} L_{\lambda'} {\rm d}\lambda'/L_{\rm bol}$ for the model SEDs (solid: Nenkova et al. 2008a, dashed: Schartmann et al. 2011), where $\lambda_{\rm min} = 10$ [Å].

(2011, see Schartmann et al. 2005 for details):

$$\lambda F_\lambda \propto \begin{cases} \lambda^2, & \lambda < 500\,{\rm Å} \\ \lambda^{0.8} & 500\,{\rm Å} \le \lambda \le 912\,{\rm Å} \\ 19\lambda^{-0.54} & 912\,{\rm Å} \le \lambda \le 10\,\mu{\rm m} \\ \lambda^{-3} & 10\,\mu{\rm m} \le \lambda \end{cases}. \quad (19)$$

The profiles and $\int_{\lambda_{\rm min}}^{\lambda} L_{\lambda'} {\rm d}\lambda'/L_{\rm bol}$ for the both SEDs are shown in Figs 2 and 3, respectively, and the properties of the SEDs are summarized in Table 2. In this study, we take into account the wavelength range of [10 Å, 10^7 Å] and assume isotropic radiation.

2.3 ISM and dust model

We assume that an ISM consists of e^-, p^+, H_I, H_2, and dust and assume that gas and dust are dynamically coupled. For simplicity, we ignore helium and metals. The effects of helium and metals are briefly discussed in Section 5. The chemical reactions and radiative processes considered in this study are summarized in Tables 3 and 4, respectively. In this paper, we denote the number of hydrogen nuclei as $n_{\rm H}$ and it is calculated by $n_{\rm H} = n_{\rm p} + n_{\rm H_I} + 2n_{\rm H_2}$.

Table 2. Properties of the model SEDs.

SED	BC$_{\rm ion}$ [a]	$h\nu_{\rm ion}$ (eV) [b]
Nenkova et al. (2008a)	1.514	44.03
Schartmann et al. (2011)	3.201	22.27

[a] Bolometric correction factor, BC$_{\rm ion}$, which is defined as $L_{\rm bol}/L_{\rm ion}$, where $L_{\rm ion} \equiv \int_{h\nu_{\rm L}}^{\infty} L_{\nu'}\,{\rm d}\nu'$ and $\nu_{\rm L}$ is the frequency at the Lyman limit.
[b] Mean-energy of ionizing photon, $h\nu_{\rm ion}$, which is defined as $h\int_{\nu_{\rm L}}^{\infty} \nu' L_{\nu'}\,{\rm d}\nu' / \int_{\nu_{\rm L}}^{\infty} L_{\nu'}\,{\rm d}\nu'$.

The effective specific heat ratio $\gamma_{\rm eff}$ of gas is computed from

$$\frac{1}{\gamma_{\rm eff} - 1} = \sum_i \frac{X_i}{\gamma_i - 1}, \quad (20)$$

where γ_i is the specific heat ratio of species i, X_i is the number fraction of species i defines as

$$X_i = \frac{n_i}{n_{\rm tot}}, \quad (21)$$

$$n_{\rm tot} = \frac{\rho}{\mu m_{\rm H}}, \quad (22)$$

where ρ is the mass density of gas and μ is the mean molecular weight relative to the mass of hydrogen atom $m_{\rm H}$. We assume $\gamma_i = 5/3$ except for $\gamma_{\rm H_2}$, for which we use

$$\frac{1}{\gamma_{\rm H_2} - 1} = \frac{1}{2}\left[5 + 2x^2 \frac{e^x}{(e^x - 1)^2}\right], \quad (23)$$

where $x = 6100\,{\rm K}/T_{\rm gas}$ (Landau & Lifshitz 1980; see also Yoshida et al. 2006).

We assume that dust consists of amorphous silicon whose composition is $MgFeSiO_4$ and whose density is 3.36 g cm^{-3} (Laor & Draine 1993). We do not consider a size distribution of dust for simplicity. We control the mass abundance of dust by the parameter $f_{\rm gr}$, which is the dust mass per hydrogen nuclei mass. Using $f_{\rm gr}$, the number density of dust is expressed as

$$n_{\rm gr} = \frac{f_{\rm gr} m_{\rm H}}{\frac{4}{3}\pi\rho_{\rm gr} a_{\rm gr}^3} n_{\rm H} \equiv \mathcal{A}_{\rm gr} n_{\rm H}, \quad (24)$$

where $a_{\rm gr}$ is the radius of a dust particle. In all the simulations, we assume $a_{\rm gr} = 0.05\,\mu$m and $f_{\rm gr} = 0.01$, leading to $\mathcal{A}_{\rm gr} \approx 9.5 \times 10^{-12}$.

The optical constants of dust, such as the absorption efficiency $\mathcal{Q}_{\rm abs}(\nu, a)$ and the scattering efficiency $\mathcal{Q}_{\rm sca}(\nu, a)$ are taken from Laor & Draine (1993).[2] We show the wavelength dependence of the absorption coefficient per hydrogen nuclei $\alpha_{\rm abs/H}(\lambda)$ in Fig. 4.

Gas and dust exchange their thermal energy each other through collisions. The rate of change of thermal energy is written as

$$\Lambda_{\rm g-gr} = n_{\rm gr} n_{\rm H} \sigma_{\rm gr} \left(\frac{8k_{\rm B}T_{\rm gas}}{\pi m_{\rm H}}\right)^{1/2} \overline{\alpha}_T 2k_{\rm B}(T_{\rm gr} - T_{\rm gas}), \quad (25)$$

where $\sigma_{\rm gr}$ is the geometrical cross-section of a dust particle, $T_{\rm gr}$ is the dust temperature, $T_{\rm gas}$ is the gas temperature, and $\overline{\alpha}_T$ is the

[2] Professor Draine kindly publishes the optical constants of dust calculated in Draine & Lee (1984) and Laor & Draine (1993) in his site http://www.astro.princeton.edu/~draine/dust/dust.diel.html.

Table 3. Chemical reactions. For the definition of the parameters below, refer to the original papers.

Number	Reaction	Rate coefficient or cross-section[a]	Reference
R1	$H_I + e^- \rightarrow p^+ + 2e^-$	$k_{R1} = \exp(-32.713\,967\,863\,75 + 13.536\,556\,090\,57\{\ln[T_{gas}(eV)]\} - 5.739\,328\,757\,388\{\ln[T_{gas}(eV)]\}^2 + 1.5631\,549\,820\,22\{\ln[T_{gas}(eV)]\}^3 - 2.877\,056\,004\,391 \times 10^{-1}\{\ln[T_{gas}(eV)]\}^4 + 3.482\,559\,773\,736\,999 \times 10^{-2}\{\ln[T_{gas}(eV)]\}^5 - 2.631\,976\,175\,59 \times 10^{-3}\{\ln[T_{gas}(eV)]\}^6 + 1.119\,543\,953\,861 \times 10^{-4}\{\ln[T_{gas}(eV)]\}^7 - 2.039\,149\,852\,002 \times 10^{-6}\{\ln[T_{gas}(eV)]\}^8)$, if $T_{gas}(eV) > 0.8$; otherwise $k_{R1} = 0$.	1
R2	$p^+ + e^- \rightarrow H_I + \gamma$	$k_{R2} = 2.753 \times 10^{-14} \frac{\lambda_{H_I}^{1.500}}{[1 + (\lambda_{H_I}/2.740)^{0.407}]^{2.242}}$, $\lambda_{H_I} = 2(157807/T_{gas})$.	2
R3	$H_2 + e^- \rightarrow 2H_I + e^-$	$k_{R3} = 4.38 \times 10^{-10} T_{gas}^{0.35} \exp(-102000/T_{gas})$	1
R4	$H_I + \gamma \rightarrow p^+ + e^-$	$\sigma_{H_I}(\nu) = 6.3 \times 10^{-18} \left(\frac{\nu}{\nu_1}\right)^{-4} \frac{\exp[4 - 4\tan^{-1}(\varepsilon)/\varepsilon]}{1 - \exp(-2\pi/\varepsilon)}$, $\varepsilon = \sqrt{\frac{\nu}{\nu_1} - 1}$, $h\nu_1 = 13.6\,eV$.	3
R5	$H_2 + \gamma \rightarrow 2H_I$	See text	4
R6	$H_2 + H_I \rightarrow 3H_I$	$k_{R6} = d \left(\frac{8E}{\pi\mu}\right)^{0.5} \frac{a E^{b-1} \Gamma(b+1) \exp(-E_0/E)}{(1 + cE)^{b+1}}$, $E = \frac{k_B T_{gas}}{27.21\,eV}$, $E_0 = 0.168$, $\mu = 2m_H/3$, $a = 54.1263$, $b = 2.5726$, $c = 3.4500$, $d = 1.849 \times 10^{-22}$.	5
R7	$H_2 + H_2 \rightarrow H_2 + 2H_I$	k_{R7} is obtained by the same formula used in k_{R6}, but with the following parameters: $E_0 = 0.1731$, $\mu = m_H$, $a = 40.1008$, $b = 4.6881$, $c = 2.1347$.	5
R8	$2H_I + \text{dust} \rightarrow H_2 + \text{dust}$	$k_{R8} = \sqrt{\frac{8k_B T_{gas}}{\pi m_H}} S_H f_a \sigma_{gr}$, $S_H = \frac{1}{[1+0.04(T_{gas}+T_{gr})^{0.5} + 0.002T_{gas} + 8\times10^{-6}T_{gas}^2]}$, $f_a = \begin{cases} 1 & 5\,K \le T_{gr} \le 20\,K \\ 0.2 & 20\,K < T_{gr} \le 500\,K \\ 0 & \text{otherwise} \end{cases}$.	6,7,8,9,10
R9	$3H_I \rightarrow H_2 + H_I$	$k_{R9} = 5.5 \times 10^{-29}/T_{gas}$	11
R10	$2H_I + H_2 \rightarrow 2H_2$	$k_{R10} = 6.875 \times 10^{-30}/T_{gas}$	11

References. – (1) Abel et al. (1997, we actually use the rate coefficients adopted in the T0D code, which is published in http://www.slac.stanford.edu/~tabel/PGas/codes.html); (2) Hui & Gnedin (1997); (3) Osterbrock & Ferland (2006); (4) Draine & Bertoldi (1996); (5) Martin, Keogh & Mandy (1998); (6) Hollenbach & McKee (1979); (7) Cazaux & Tielens (2004); (8) Cazaux & Spaans (2004); (9) Cazaux & Tielens (2010); (10) Hirashita & Ferrara (2002); (11) Palla, Salpeter & Stahler (1983).

[a] The rate coefficient is in $cm^3\,s^{-1}$ except for the reaction R9 and R10. They are in $cm^6\,s^{-1}$. The temperatures are in K unless otherwise stated. The cross-section is in cm^2. The definition of the formation efficiency f_a in the reaction R8 is based on the results of Cazaux & Spaans (2004).

average accommodation coefficient (Burke & Hollenbach 1983). As shown in fig. 4 in Burke & Hollenbach (1983), $\overline{\alpha}_T$ depends on T_{gr}, T_{gas}, dust composition, and gas composition. Because it is difficult to take into account all of these dependence, we assume $\overline{\alpha}_T = 0.4$ in this study.

We assume that dust is instantaneously settled in the thermal equilibrium. In this case, T_{gr} is determined by the following equation,

$$\int_0^\infty \frac{L_\nu}{4\pi r^2} \exp(-\tau_\nu(r)) \mathcal{Q}_{abs}(\nu, a) \pi a^2 n_{gr} d\nu - \int_0^\infty 4\pi a^2 \pi B_\nu(T_{gr}) \mathcal{Q}_{abs}(\nu, a) n_{gr} d\nu - \Lambda_{g-gr} = 0. \quad (26)$$

Table 4. Rates of the radiative processes and thermal processes. We shorten the name of the processes into symbols and their meanings are as follows: RC – case B recombination cooling; BC – Bremsstrahlung cooling of H_I; CIC_{H_I} – collisional ionization cooling of H_I; CEC_{H_I} – collisional excitation cooling of H_I; CEC_{H_2} – collisional excitation cooling of H_2 rovibrational lines; $Chem_{H_2}$ – chemical heating and cooling of H_2; GG – collisional gas–grain energy transfer.

Process	RC	BC	CIC_{H_I}	CEC_{H_I}	CEC_{H_2}	$Chem_{H_2}$	GG
Reference	1	7	4	4	2,3	2	6

References – (1) Hui & Gnedin (1997); (2) Hollenbach & McKee (1979); (3) Galli & Palla (1998); (4) Cen (1992); (5) Fukugita & Kawasaki (1994); (6) Burke & Hollenbach (1983); (7) Kellogg, Baldwin & Koch (1975).

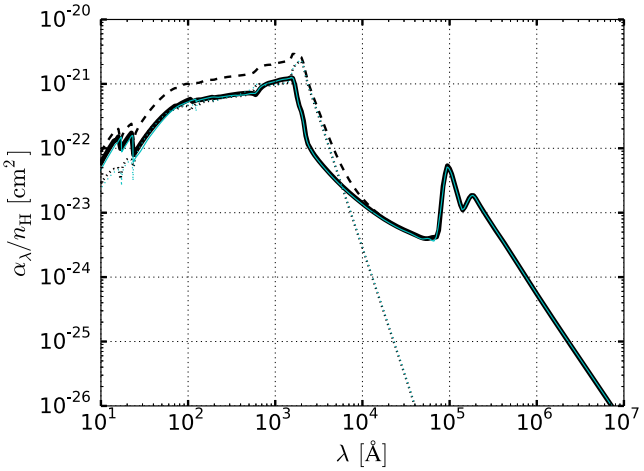

Figure 4. The wavelength dependence of the absorption coefficient per hydrogen nuclei for $a_{gr} = 0.05$ μm (thick black solid line). For reference, we also show the scattering coefficient per hydrogen nuclei (thin black dotted line) and the extinction coefficient per hydrogen nuclei (thin black dashed line). We express the extinction coefficient as the sum of the absorption coefficient and the scattering coefficient for simplicity. The absorption and scattering coefficients per hydrogen nuclei for $a_{gr} = 0.05$ μm used in the CLOUDY are shown thin cyan solid line and thin cyan dotted line, respectively (see Section 5.1.1).

For the adopted ISM model and AGN SED, we calculate the equilibrium temperatures and number fractions for various obscuring column densities, assuming $L_{bol} = 5 \times 10^{44}$ erg s^{-1} and $r = 50$ pc and the results are shown in Figs 5 and 6.

3 NUMERICAL METHODS

In this section, we explain the numerical method in detail.

3.1 Hydrodynamics and gravity

We use the pressure–energy smoothed particle hydrodynamics (SPH) formulation[3] proposed by Hopkins (2013) to solve hydrodynamics. We employ the M_4 cubic spline kernel (Monaghan & Lattanzio 1985; see also Springel 2005) with the kernel gradient modification used in Thomas & Couchman (1992). The artificial viscosity formulation proposed by Monaghan (1997) is used. To reduce artificial viscosity in smooth regions of the flow, we vary the viscous parameter α_{vis}^{SPH} within the range of $\alpha_{vis}^{SPH} \in [0.1, 1]$ according to Morris & Monaghan (1997). We also employ the Balsara switch (Balsara 1995). The density estimates are computed by using the 'gather' neighbours,[4] while we calculate the pressure gradient, the artificial viscosity, and the time derivative of the internal energy by using the 'gather-and-scatter' neighbours. The smoothing length is adjusted so that the number of the 'gather' neighbours $N_{nb}^{gat} = 50 \pm 2$.

The gravitational force is computed by the tree method with the opening angle of $\theta = 0.5$ (Barnes & Hut 1986). We take into count monopole components only. We adopt the optimal binary tree structure described in Anderson (1999). In the construction of the interaction lists, we use the group interaction list technique (Barnes 1990; Makino 1991) and use the maximum side lengths of each tree node to evaluate the opening criterion. The calculation of the gravitational force is accelerated by the Phantom-GRAPE libraries which use Streaming SIMD Extensions or Advanced Vector Extensions (AVX) instructions.[5]

The code is parallelized with the Message Passing Interface. The domain decomposition is done by the sampling method (e.g. Makino 2004). The time integration is performed by the standard leapfrog method.

3.2 Radiative transfer

We explain here our treatment of the radiative transfer (RT) calculation. First of all, we summarize the approximations used in this study. (1) We do not consider any scattering processes and effects of the Doppler-shift. In other words, we only take into account absorption processes in the simplest way, (2) we employ the so-called on-the-spot approximation for the ground state H_I recombination photons (Osterbrock & Ferland 2006), (3) we employ an approximate formula for the photodissociation rate of H_2 and (4) we assume optically thin for photons arisen from the radiative processes listed in Table 4. In the following, we explain the numerical treatment in more detail.

In the absence of scattering processes and Doppler-shift, the formal solution of the steady RT equation for a ray can be written as

$$I_\nu(r) = I_\nu(0) \exp\left(-\sum_i \sigma_{abs}^i(\nu) N_i(r)\right), \quad (27)$$

where $\sigma_{abs}^i(\nu)$ is the absorption cross-section of species i at the frequency ν and $N_i(r)$ is the column density of species i at a distance of r from the radiation source, respectively. Thus, the specific intensities at arbitrary positions are written as a function of the column densities. Using the point source approximation, the photoionization rate of H I, the photoheating rates of H I and dust, and the radiative

[3] This formulation is a variant of the density-independent formulation proposed by Saitoh & Makino (2013) and can treat contact discontinuity more accurately than the standard SPH formulation (e.g. Gingold & Monaghan 1977; Lucy 1977).

[4] The meanings of the 'gather' and the 'scatter' are referred to Hernquist & Katz (1989).

[5] In Cray XT4 system, we use the limited accuracy version of the Phantom-GRAPE library which is developed by Keigo Nitadori. Unfortunately, the detail of the library is not published as a paper, but we can find the detail description for the full accuracy version of the library in Nitadori, Makino & Hut (2006). In Cray XC30 system, we use the AVX version of the Phantom-GRAPE library which is developed by Tanikawa et al. (2013). The Phantom-GRAPE library for collisional N-body system is also developed and see Tanikawa et al. (2012) for details if you are interested in it.

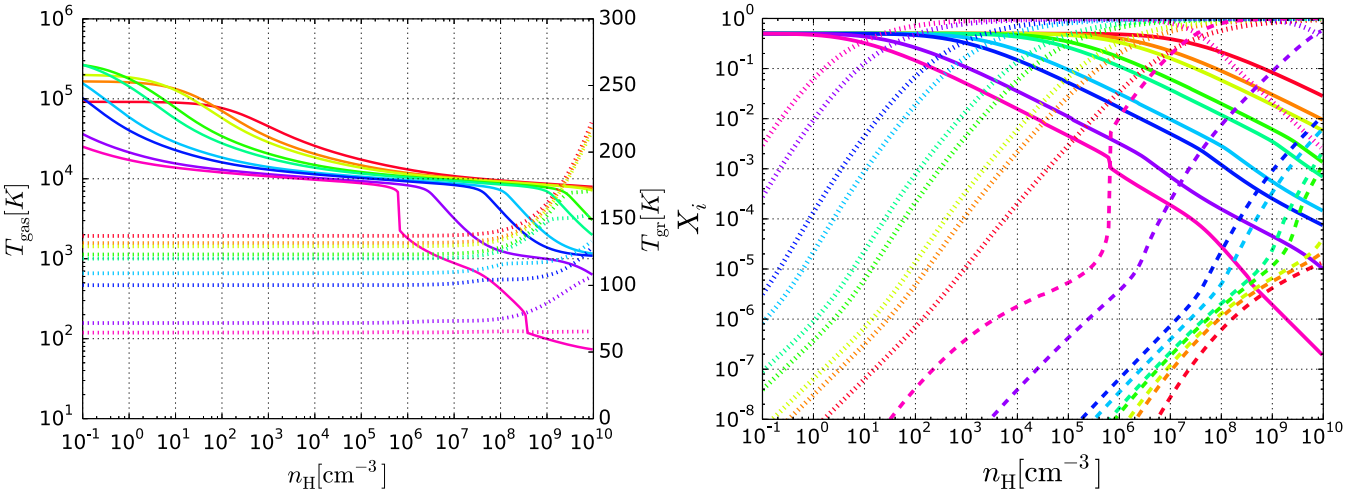

Figure 5. Equilibrium temperatures and number fractions in the adopted ISM model are plotted as a function of $n_{\rm H}$ for various $N_{\rm H_I}^{\rm obs}$ assuming a fixed radiation field ($L_{\rm bol} = 5 \times 10^{44}\,{\rm erg\,s^{-1}}$, $r = 50\,{\rm pc}$), where $N_{\rm H_I}^{\rm obs}$ is the obscuring H I column density. Obscuring gas contains dust with $f_{\rm gr} = 0.01$ and its column density is simply used to attenuate an incident radiation field. The ISM is assumed to be at the rest and therefore hydrodynamic effects such as thermal expansion cooling is not taken into account. In both panels, the line colours, in the order of red to magenta, correspond to $N_{\rm H_I}^{\rm obs} = 10^{18}$, 5×10^{18}, 10^{19}, 5×10^{19}, 10^{20}, 5×10^{20}, 10^{21}, 5×10^{21} and $10^{22}\,{\rm cm^{-2}}$. Left: the gas temperature (solid; left y-axis) in the logarithmic scale and dust temperatures (dotted; right y-axis) in the linear scale. Since the obscuring H I makes the incident spectrum hard by preferentially absorbing photons of energy near 13.6 eV and since the recombination cooling becomes inefficient in low density, $T_{\rm gas}$ becomes higher in low $n_{\rm H}$ regime. $T_{\rm gr}$ increases with $n_{\rm H}$ because the dust–gas coupling becomes tight. Right: the number fractions of e (solid), H I (dotted) and H_2 (dashed).

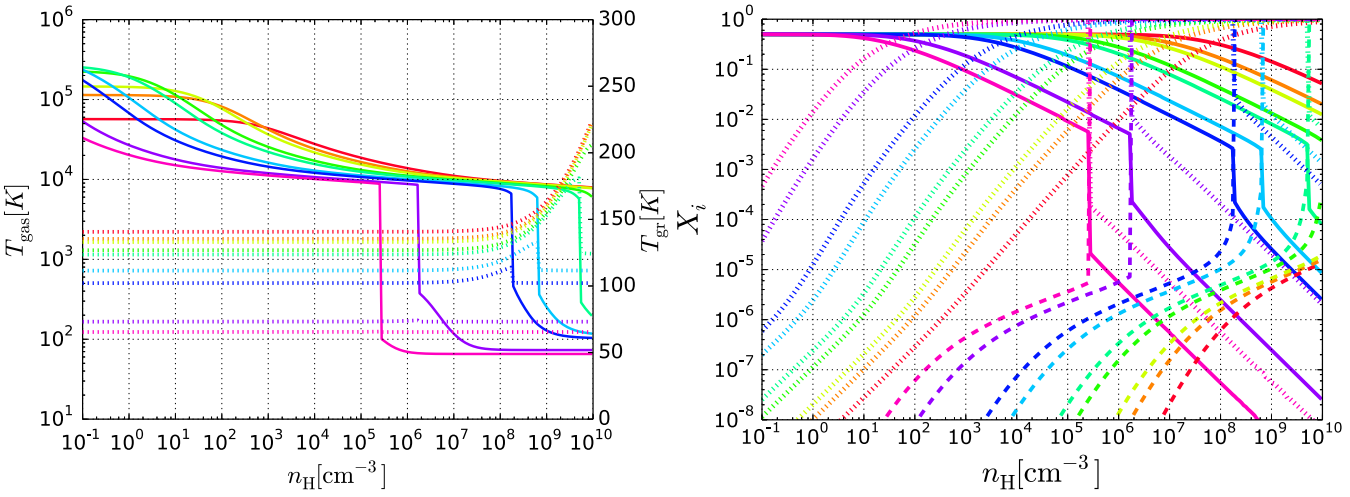

Figure 6. The same as Fig. 5, but for the case that the obscuring column consists of $N_{\rm H_I}^{\rm obs}$ and $N_{\rm H_2}^{\rm obs}$. In both panels, the line colours correspond to $N_{\rm H}^{\rm obs} = 10^{18}$, 5×10^{18}, 10^{19}, 5×10^{19}, 10^{20}, 5×10^{20}, 10^{21}, 5×10^{21} and $10^{22}\,{\rm cm^{-2}}$. In all cases, the ratio of $N_{\rm H_I}^{\rm obs}$ to $N_{\rm H_2}^{\rm obs}$ is unity. Because of the self-shielding of H_2, H_2 formation occurs in lower $n_{\rm H}$ compared to the cases in Fig. 5.

accelerations of H I and dust are given by

$$k_{\rm H_I}(r) = n_{\rm H_I} \int_{\nu_{\rm L}}^{\infty} \frac{L_\nu {\rm e}^{-\tau_\nu}}{4\pi r^2 h\nu} \sigma_{\rm abs}^{\rm H_I}(\nu)\,{\rm d}\nu, \tag{28}$$

$$\Gamma_{\rm H_I}(r) = n_{\rm H_I} \int_{\nu_{\rm L}}^{\infty} \frac{L_\nu {\rm e}^{-\tau_\nu}}{4\pi r^2 h\nu} (h\nu - h\nu_{\rm L}) \sigma_{\rm abs}^{\rm H_I}(\nu)\,{\rm d}\nu, \tag{29}$$

$$\Gamma_{\rm gr}(r) = n_{\rm gr} \int_{0}^{\infty} \frac{L_\nu {\rm e}^{-\tau_\nu}}{4\pi r^2} \sigma_{\rm abs}^{\rm gr}(\nu)\,{\rm d}\nu, \tag{30}$$

$$\boldsymbol{a}_{\rm H_I}(r) = n_{\rm H_I} \frac{1}{c\rho} \int_{\nu_{\rm L}}^{\infty} \frac{L_\nu {\rm e}^{-\tau_\nu}}{4\pi r^2} \sigma_{\rm abs}^{\rm H_I}(\nu)\,{\rm d}\nu, \tag{31}$$

$$\boldsymbol{a}_{\rm gr}(r) = n_{\rm gr} \frac{1}{c\rho} \int_{0}^{\infty} \frac{L_\nu {\rm e}^{-\tau_\nu}}{4\pi r^2} \sigma_{\rm abs}^{\rm gr}(\nu)\,{\rm d}\nu, \tag{32}$$

where $\nu_{\rm L}$ is the frequency at the Lyman limit, L_ν is the monochromatic luminosity of the radiation source, and $\tau_\nu = \sum_i \sigma_{\rm abs}^i(\nu) N_i(r)$.

As in Tajiri & Umemura (1998), Hasegawa & Umemura (2010) and Okamoto, Yoshikawa & Umemura (2012), we make look-up tables for the integrals in equation (28)–(32) except for the geometrical dilution factor $(4\pi r^2)^{-1}$ as a function of the column densities, before we start the simulations. The frequency dependences of the incident spectrum and relevant cross-sections are properly taken into account when making the look-up tables. In the simulations, we evaluate the photoionization rate and the rest by interpolating from these pre-computed look-up tables to specified column

densities and applying the geometrical dilution. The column densities of each species for each particle are computed by the tree-accelerated long characteristics method described in Appendix B. The photoionization rate of H I and others are evaluated by the method described in Appendix C. In this study, the look-up tables are made for $(N_{\rm H_I}, N_{\rm H})$-grid with 128 grid points in each dimension.

In order to evaluate the photodissociation rate of H_2 accurately, we should solve the frequency-dependent RT equation of the Lyman–Werner band photons coupled with the H_2 level population equations. However, such computation is too costly to be coupled with hydrodynamics except for one-dimensional (1D) calculation. Therefore, we use an approximation formula given by Draine & Bertoldi (1996). They performed detailed RT calculations of a plane-parallel stationary photodissociation region and derived simple analytic approximate formulae for the photodissociation rate of H_2 as a function of H_2 column density $N_{\rm H_2}$ and dust extinction. The approximate formula is written as

$$k_{\rm diss}(N_{\rm H_2}) = k_{\rm diss,0} n_{\rm H_2} \exp(-\tau_{\rm d}^{\rm LW}) f_{\rm sh}(N_{\rm H_2}), \tag{33}$$

where $k_{\rm diss,\,0}$ is unshielded photodissociation rate, $\tau_{\rm d}^{\rm LW}$ is the dust optical depth at the LW band, $f_{\rm sh}$ is the self-shielding function of H_2 and is defined as

$$f_{\rm sh}(N_{\rm H_2}) = \min\left[1, \left(\frac{N_{\rm H_2}}{10^{14}\,{\rm cm^{-2}}}\right)^{-0.75}\right]. \tag{34}$$

Following Abel et al. (1997), we adopt

$$k_{\rm diss,0} = 1.1 \times 10^8 F_\nu^{\rm LW}, \tag{35}$$

where $F_\nu^{\rm LW}$ is the radiation flux at $h\nu_{\rm LW} = 12.87\,{\rm eV}$. Draine & Bertoldi (1996) gave an another more accurate approximate formula. Also, Wolcott-Green, Haiman & Bryan (2011) propose recently an improved version of this second formula. In this study, we do not use these formulae, because they contain a Doppler broadening parameter and it is difficult to adjust the parameter to optimal value in inhomogeneous medium.

The radiative acceleration by absorption of the H_2 photodissociating photon is calculated by

$$|\boldsymbol{a}_{\rm rad,H_2}| = \frac{k_{\rm diss} h\nu_{\rm LW}}{c\rho}. \tag{36}$$

Finally, we note that our approximate treatment of dust and H_2 somewhat overestimates energy and momentum transfer from radiation to matter in the Lyman–Werner band, since the change of the incident spectrum shape by absorption of the Lyman–Werner photons is not taken into account when we make the look-up tables.

3.3 Non-equilibrium chemistry and radiative processes

We solve time-dependent chemical reaction equations for e^-, p^+, H_I, H_2 coupled with the internal energy equation of gas implicitly.

In the implicit method, a physical variable A is integrated by solving iteratively the following equation:

$$A^{t+\Delta t_{\rm g}} = A^t + \left(\frac{{\rm d}A}{{\rm d}t}\right)^{t+\Delta t_{\rm g}} \Delta t_{\rm g}, \tag{37}$$

where $\Delta t_{\rm g}$ is the global timestep with which the hydrodynamics is solved (defined later). However, the straightforward implicit integration of the coupled equations is numerical unstable, because time-scales of the chemical reactions and the internal energy are largely different from $\Delta t_{\rm g}$ in general. In order to solve the coupled equations efficiently and stably, we follow a similar approach adopted in Whalen & Norman (2006) and Okamoto et al. (2012). Our approach is shown in Algorithm 1. In the method, we divide $\Delta t_{\rm g}$ into subcycle. The number of subcycle is determined by dividing $\Delta t_{\rm g}$ by $\Delta t_{\rm sub} \equiv \min(\Delta t_{\rm chem}, \Delta t_{\rm engy})$, where $\Delta t_{\rm chem}$ and $\Delta t_{\rm engy}$ are the chemical timestep and the internal energy timestep, respectively (these are also defined later). If $\Delta t_{\rm sub}$ are longer than $\Delta t_{\rm g}$, the number of the subcycle is taken to be 1. In the subcycle, we solve the time-dependent chemical reaction equations and the internal energy equation alternately for a fixed radiation field. After updating the chemical abundance and the internal energy, we perform the RT calculation using the previously updated physical variables. Thus, we update the matter field and the radiation field alternatively. This procedure is repeated until $\boldsymbol{n}$, $T_{\rm gas}$, $T_{\rm gr}$ and $\boldsymbol{a}_{\rm rad}$ are converged, where $\boldsymbol{n}$ is the number density vector and $\boldsymbol{a}_{\rm rad}$ is the radiative acceleration. In this study, we decide that the convergence is achieved, if the maximum relative difference of these physical variables over all the particles is less than 10^{-2}. We do not find a significant difference between numerical results such as density distribution with this convergence criterion ($\epsilon_{\rm rel}^{\rm tol} = 10^{-2}$) and with a more strict one (e.g. $\epsilon_{\rm rel}^{\rm tol} = 10^{-3}$).

We use the α-QSS method (Mott, Oran & van Leer 2000) to solve the chemical reaction equations and the internal energy equation.

Algorithm 1: Non-equilibrium chemistry

Data: k is the iteration number,
$\mathcal{P}$ is the set of the particles,
$\mathcal{M}^{(k)} = \{p.\boldsymbol{n}^{(k)}, p.T_{\rm gas}^{(k)}, p.T_{\rm gr}^{(k)} | p \in \mathcal{P}\}$
is the matter variables,
$\mathcal{R}^{(k)} = \{p.k_{\rm ion}^{(k)}, p.\Gamma_{\rm ph}^{(k)}, p.\boldsymbol{a}_{\rm rad}^{(k)} | p \in \mathcal{P}\}$
is the radiation fields, and
$\mathcal{C}^{(k)} = \{p.\boldsymbol{n}^{(k)}, p.T_{\rm gas}^{(k)}, p.T_{\rm gr}^{(k)}, p.\boldsymbol{a}_{\rm rad}^{(k)} | p \in \mathcal{P}\}$
is the variables that we want to converge.

```
RT calculation and obtain R^(0);
save M^(0) ;
k = 0 ;
repeat
    k = k + 1 ;
    foreach p ∈ P do
        calculate Δt_sub;
        t = t_start ;
        while t < t_end do
            update chemical abundance ;
            update gas and dust temperatures ;
            t = t + Δt_sub ;
            update Δt_sub ;
        end
    end
    RT calculation and obtain R^(k);
    compare C^(k) with C^(k−1) and calculate the
    maximum relative difference ε_rel^max;
    if ε_rel^max ⩽ ε_rel^tol then
        exit the infinite loop;
    else
        save C^(k) ;
        reset P using M^(0) and R^(k);
    end
until convergence achieved;
```

The α-QSS method is a predictor–corrector type integrator and is originally developed to solve stiff chemical reaction equations. In actual calculations, we solve time evolution of the gas temperature rather than the internal energy. The conversion of the equation is performed assuming that a change of $\gamma_{\rm eff}$ is small. In the following, we describe the adopted method in terms of the number density and the gas temperature. In order to apply the α-QSS method, we split source terms into an increasing rate and a decreasing rate and rewrite the equations in the form of

$$\frac{{\rm d}n_i}{{\rm d}t} = C_i - D_i n_i, \tag{38}$$

$$\frac{{\rm d}T_{\rm gas}}{{\rm d}t} = C - DT_{\rm gas}, \tag{39}$$

where $n_i = \rho Y_i/m_i$, ρ is the mass density of gas, Y_i is the mass fraction of species i, m_i is the mass of species i. The index i is either of e^-, p^+, H_I, H_2 in our study. The C_i are the collective source terms responsible for the creation of species i. The second terms $D_i n_i$ in the equation (38) represent the destruction for species i. C and D are defined as such that C and $DT_{\rm gas}$ is the increasing and decreasing rate of the gas temperature, respectively. C_i, D_i, C and D are the functions of $T_{\rm gas}$, $T_{\rm gr}$, $\boldsymbol{n}$. But, hereafter, we omit dependence for brevity.

The integration scheme for the gas temperature is written as

$$T_{\rm gas}^p = T_{\rm gas}^0 + \frac{\Delta t(C^0 - D^0 T_{\rm gas}^0)}{1 + \alpha \Delta t D^0}, \quad \text{(Predictor)}, \tag{40}$$

$$T_{\rm gas}^c = T_{\rm gas}^0 + \frac{\Delta t(\widetilde{C} - \overline{D} T_{\rm gas}^0)}{1 + \overline{\alpha} \Delta t \overline{D}}, \quad \text{(Corrector)}, \tag{41}$$

where $T_{\rm gas}^0$ is the gas temperature at the present time, $C^0 \equiv C(T_{\rm gas}^0, T_{\rm gr}^0)$, $D^0 \equiv D(T_{\rm gas}^0, T_{\rm gr}^0)$, and α is defined as

$$\alpha(D\Delta t) = \frac{180r^3 + 60r^2 + 11r + 1}{360r^3 + 60r^2 + 12r + 1}, \tag{42}$$

where $r = 1/(D\Delta t)$. $\overline{D}$ and $\widetilde{C}$ in the corrector are defined as

$$\overline{D} = \frac{1}{2}(D^0 + D^p), \tag{43}$$

$$\widetilde{C} = \overline{\alpha} C^p + (1 - \overline{\alpha}) C^0, \tag{44}$$

where $C^p \equiv C(T_{\rm gas}^p, T_{\rm gr}^p)$, $D^p \equiv D(T_{\rm gas}^p, T_{\rm gr}^p)$, and $\overline{\alpha} = \alpha(\overline{D}\Delta t)$. $T_{\rm gr}^p$ and $T_{\rm gr}^c$ are computed by equation (26) using $T_{\rm gas}^p$ and $T_{\rm gas}^c$, respectively. The accuracy of the solution can be improved by the multiple corrections. In this study, we continue to correct until the relative difference becomes less than 10^{-5}. We note that equations (40) and (41) are also definitely positive. Finally, we note that we need to carefully classify the dust–gas energy transfer term into C or D, because its sign changes depending on $T_{\rm gas}$ and $T_{\rm gr}$.

The integration scheme of the number density used in this study is basically the same as that for the gas temperature. One difference is the existence of the normalization step: the predicted and corrected number densities, n_i^p and n_i^c, are scaled to satisfy $\rho = \sum_i m_i n_i^p = \sum_i m_i n_i^c$.

We determine the chemical timestep and the internal energy timestep by

$$\Delta t_{\rm chem} = 0.01 \min_i \frac{(n_i + n_{\rm min})}{\dot{n}_i}, \tag{45}$$

$$\Delta t_{\rm engy} = 0.01 \frac{e_{\rm th}}{\dot{e}_{\rm th}}, \tag{46}$$

where $e_{\rm th}$ is the internal energy per unit volume and $n_{\rm min} = 0.001 n_{\rm H}$. By introducing $n_{\rm min}$, we avoid a very small timestep, which occurs when the number density of a species is nearly zero.

3.4 Global timestep

Following Monaghan (1997), we determine the hydrodynamic timestep of particle i by

$$\Delta t_{{\rm hyd},i} = \frac{C_{\rm hyd} h_i}{v_i^{\rm sig}}, \tag{47}$$

where h_i is the smoothing length, $C_{\rm hyd} = 0.25$, and $v_i^{\rm sig}$ is the local maximum signal velocity, which is defined as

$$v_i^{\rm sig} = \max_j (c_{{\rm s},i} + c_{{\rm s},j} - 3w_{ij}), \tag{48}$$

where j denotes the indices of neighbour particles, $c_{{\rm s},i}$ and $c_{{\rm s},j}$ are the adiabatic sound speeds of particles i and j, and $w_{ij} = \min(0, \boldsymbol{v}_{ij} \cdot \boldsymbol{r}_{ij}/|\boldsymbol{r}_{ij}|)$ is the relative velocity projected on to the separation vector $\boldsymbol{r}_{ij} \equiv \boldsymbol{r}_i - \boldsymbol{r}_j$, where $\boldsymbol{v}_{ij} = \boldsymbol{v}_i - \boldsymbol{v}_j$.

We determine the gravitational timestep of particle i by

$$\Delta t_{{\rm grv},i} = \frac{C_{\rm grv} \max(|\boldsymbol{v}_i|, c_{{\rm s},i})}{|\boldsymbol{a}_i|}, \tag{49}$$

where $\boldsymbol{a}_i$ is the total acceleration and $C_{\rm grv} = 0.1$. The introduction of the sound speed in the numerator is intended to avoid $\Delta t_{{\rm grv},i} = 0$.

The global timestep $\Delta t_{\rm g}$ is calculated by $\min_i(\Delta t_{{\rm hyd},i}, \Delta t_{{\rm grv},i})$. However, if we use $\Delta t_{\rm g}$ directly, it often happens that the iteration in the calculation of the non-equilibrium chemistry is not converged, because $\Delta t_{\rm g}$ is usually much larger than the time-scales of chemical reactions and change of the internal energy. Therefore, we restrict $\Delta t_{\rm g}$ by $\Delta t_{\rm lim}$, which is calculated as

$$\Delta t_{\rm lim} = \Delta t_{\rm g}^{\rm prev} \times \begin{cases} 2^{1/8} & , N_{\rm iter} \leq 4, \\ 2^{-1/8} & N_{\rm iter} \geq 6, \end{cases} \tag{50}$$

where $\Delta t_{\rm g}^{\rm prev}$ is the global timestep at the previous step, $N_{\rm iter}$ is the iteration number at the previous step. This device adjusts the global timestep automatically so that the iteration number is close to 4−6.

3.5 Temperature floor

In the simulations, a dense shocked layer is formed in the gas cloud by the counteraction of the thermal expansion of the gas at the irradiation surface or the radiation pressure force acting on the irradiation surface. Insufficient mass resolution induces artificial self-gravitational fragmentation in the shocked layer. In order to avoid it, we impose a lower limit for the gas temperature on each particle according to

$$T_{\rm gas}^{\rm min}(\rho) = 6^{2/3} \frac{\mu m_{\rm H}}{k_{\rm B}} \left(\frac{G^3 \rho (2N_{\rm nb}^{\rm gat} \times m_{\rm SPH})^2}{\gamma_{\rm eff}^3 \pi^5} \right)^{1/3} {\rm K}, \tag{51}$$

where $m_{\rm SPH}$ is the mass of the SPH particle. The almost same temperature floor is used in Saitoh et al. (2006). We note that $\gamma_{\rm eff}$ in the right-hand side depends on the gas temperature and therefore we need an iteration to determine the minimum temperature and also note that we compute $\Delta t_{\rm sub}$ by $\Delta t_{\rm chem}$ only for the SPH particle at which the temperature floor is active.

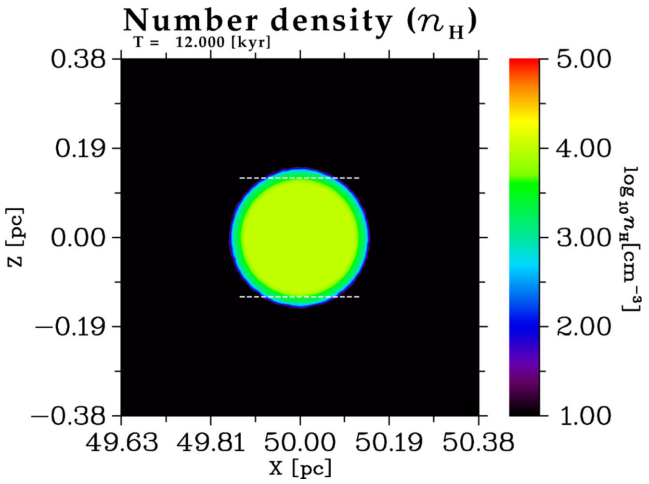

Figure 7. The number density distribution of model L05 at $t = 12$ kyr *without* AGN radiation. The white dotted lines show the initial cloud size.

3.6 Initial condition

Initial uniform SPH particle distributions are obtained by cutting a sphere of $\approx 2^{18}$ particles from hydrodynamically relaxed periodic cube, and scaling the mass and the position of each particle to fit the specified model parameters. Then, the cloud is shifted so that the cloud centre is located at $(x, y, z) = (50\,\mathrm{pc}, 0, 0)$.

In all the simulation runs, we assume (i) that the initial gas and dust temperatures are $T_{\rm gas} = 100\,\mathrm{K}$ and $T_{\rm gr} = 20\,\mathrm{K}$, respectively, and (ii) that the length of the gravitational softening is 50 au. In this resolution, the Strömgren length corresponds to $3\ell_{\rm mid}$ in the case of $\mathcal{N}_{\rm S} = 20$, where $\ell_{\rm mid}$ is the mean interparticle distance. The numerical results are not sensitive to the initial temperatures.

4 NUMERICAL RESULTS

Here, we first explain in Section 4.1 the time evolution of the clouds without the AGN radiation to make clear the effects of the AGN radiation. Next, we show the results of Low-$\mathcal{U}$ models in Section 4.2 and High-$\mathcal{U}$ models in Section 4.3, respectively. Then, the results of SC00-3D are shown in Section 4.4. Finally, in Section 4.5, we compare the time evolution of dense gas fraction in each model.

4.1 No-$\mathcal{U}$ models

Since their Jeans ratios are larger than unity (see Table 1), the clouds in models L05, L10, L20 and H05 expand by their thermal pressure without the AGN radiation. This will make it difficult to estimate the contribution of the photoheating in cloud expansion. In order to make clear the effects of the AGN radiation, we first perform a numerical simulation *without* the AGN radiation for the cloud model L05, which has the largest $r_{\rm J}$. The simulation is performed to $t = 12$ kyr, which are the same as the final calculation time shown in Section 4.2. Fig. 7 shows the number density slice of model L05 at $t = 12$ kyr. The initial cloud size is shown by the white dotted lines in the figure. We can see from this figure that the cloud radius is virtually constant until $t = 12$ kyr. Thus, the thermal expansion of the cloud is negligible.

4.2 Low-$\mathcal{U}$ models

Fig. 8 shows the time evolution of the number density distribution of Low-$\mathcal{U}$ models at the $y = 0$ plane. Immediately after the simulation starts, most of the molecular hydrogen from the irradiated face to a depth of $N_{\rm H} \approx 10^{22}\,\mathrm{cm}^{-2}$ is photodissociated and is turned into the atomic hydrogen. This atomic hydrogen is also rapidly ionized and the photoionization region forms at the irradiated face of the cloud. During this initial evolution, a distinct dense gas layer is formed at the depth of $N_{\rm H} \approx 5 \times 10^{21}\,\mathrm{cm}^{-2}$, which corresponds to the Strömgren length $l_{\rm S}$,

$$l_{\rm S} = 0.15\,\mathrm{pc}\left(\frac{L_{\rm ion}}{1.25\times10^{44}\,\mathrm{erg\,s^{-1}}}\right) \times \left(\frac{n_{\rm H}}{10^4\,\mathrm{cm^{-3}}}\right)^{-2}\left(\frac{r}{50\,\mathrm{pc}}\right)^{-2}. \quad (52)$$

Most of the H_I-photoionizing photons are absorbed by this layer. Because the photoheating rates are large in this layer, the photoevaporation flow occurs at the layer. The counteraction of the photoevaporation flow pushes the layer and convert it into the D-type shock (e.g. Fig. 8a). For model L20, the time-averaged velocity of the shocked layer, $\overline{v}_{\rm sh}$, is $\approx$18 km s^{-1} and is larger than the estimated value by the razor-thin approximation $v_{\rm sh}^{\rm app}(L_{\rm bol} = 1.25\times10^{44}) = 9.4\,\mathrm{km\,s^{-1}}$. This enhancement is due to the so-called rocket effect (Oort & Spitzer 1955). On the other hand, $\overline{v}_{\rm sh} \approx 20.8\,\mathrm{km\,s^{-1}}$ for model L05. Thus, the rocket effect is more effective for smaller $\mathcal{N}_{\rm S}$ model.

The direction of the photoevaporation flow is roughly spherically outwards and its back reaction, by necessity, points spherically inwards. Therefore, the shocked layer gradually bends and takes the shape of an circular cone (e.g. Fig. 8f). As the calculation advances, it continues to collapse and finally forms a very dense molecular filament (Figs 8d and h). In model L10, its number density is $n_{\rm H} \approx 10^5$–$10^8\,\mathrm{cm}^{-3}$ at $T = 28.5$ kyr (Figs 8h and 9). A part of the photoevaporation flow comes around behind the cloud and collides with itself. As a consequence, it takes part in the formation of the dense filament. Since self-shielding is effective in the filament, it promptly becomes neutral. After the dense filament is formed, the rate of the photoevaporation from the irradiated face decreases rapidly. It is mainly because the surface area of the filament is very small in this stage. The high density of the filament may be another factor, since the H_I recombination cooling and the H_2 formation becomes efficient and consequently $T_{\rm gas}$ and $X_{\rm H_I}$ becomes small. By this stage, a considerable fraction of the initial gas is evaporated. Thus, the evolution of the gas clouds are mainly determined by the photoevaporation in Low-$\mathcal{U}$ models.

In order to show the chemical structure in the photoevaporation flow, we show the time evolution of the number fraction X_i distribution of model L20 in Fig. 10. From the comparison Figs 10(a)–(d) with Figs 8(i)–(l), the low-density ($n_{\rm H} \lesssim 10^2\,\mathrm{cm}^{-3}$) gas that encloses the dense filament is ionized completely. The irradiated side of the shocked gas layer predominantly consists of H_I (Fig. 10e) and the opposite side of the shocked layer consists of H_I–H_2 mixtures.

Fig. 11 shows the time evolution of the velocity field at different plotting scales. The velocity field is almost spherical at an early time ($T < 27$ kyr). At later times, the evaporated gas drifts slightly towards the opposite direction to the AGN because of the radiation pressure. The velocity of the front of the photoevaporation flow is more than 100 km s^{-1} and is supersonic.

4.3 High-$\mathcal{U}$ models

Fig. 12 shows the time evolution of the number density distribution of High-$\mathcal{U}$ models at the $y = 0$ slice (enlarged views are shown in Fig. 13). As in the Low-$\mathcal{U}$ models, High-$\mathcal{U}$ models also show the

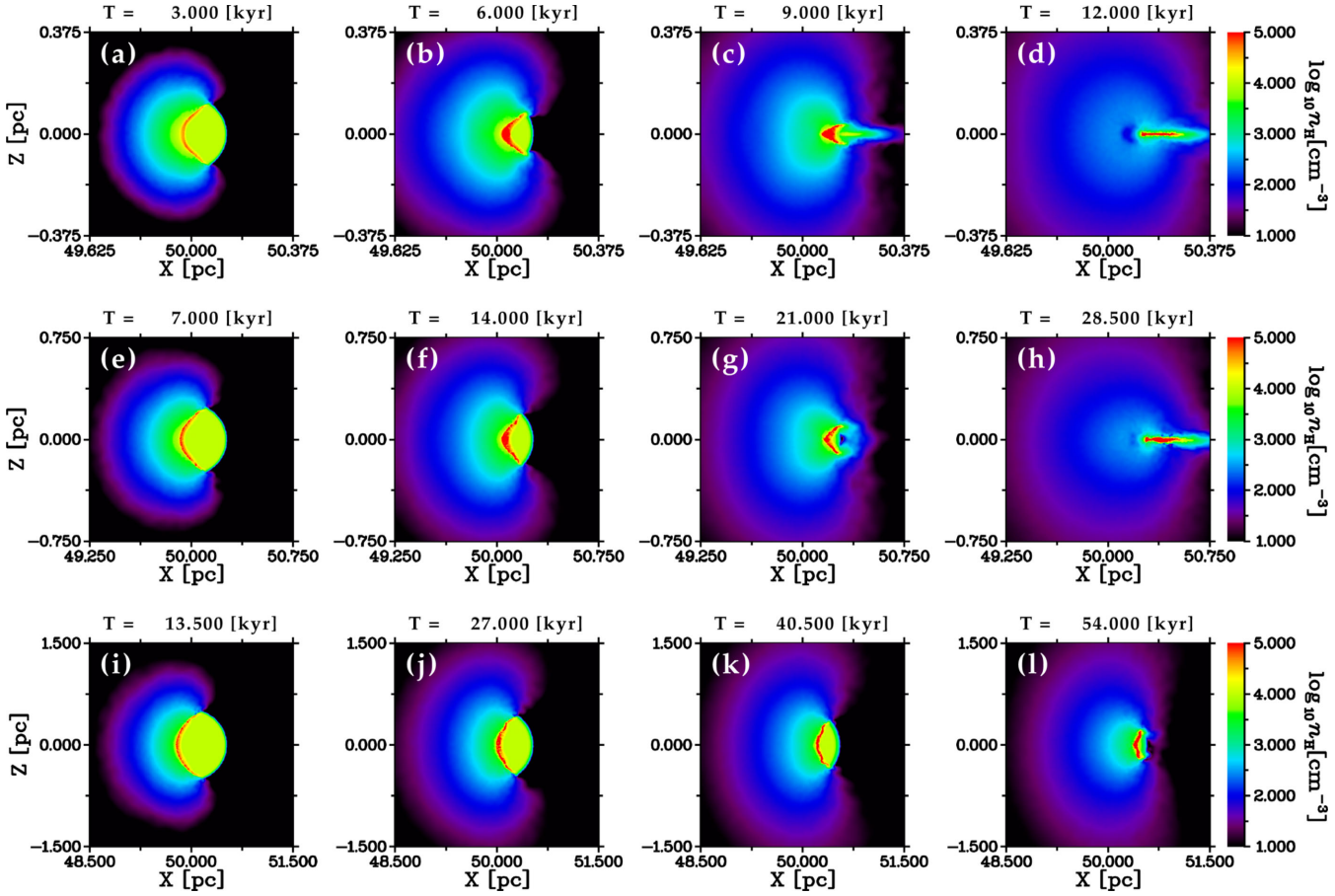

Figure 8. Time evolution of the number density distribution in Low-$\mathcal{U}$ models (from the top to the bottom, L05, L10, and L20 are plotted). The AGN, the radiation source, is located at $(x, y, z) = (0, 0, 0)$. The each panel shows the number density distribution at $y = 0$ slice. We show the calculation time on the top of each panel. For the spherical very low density regions found in models L10 and L05 at a later calculation time, see the text.

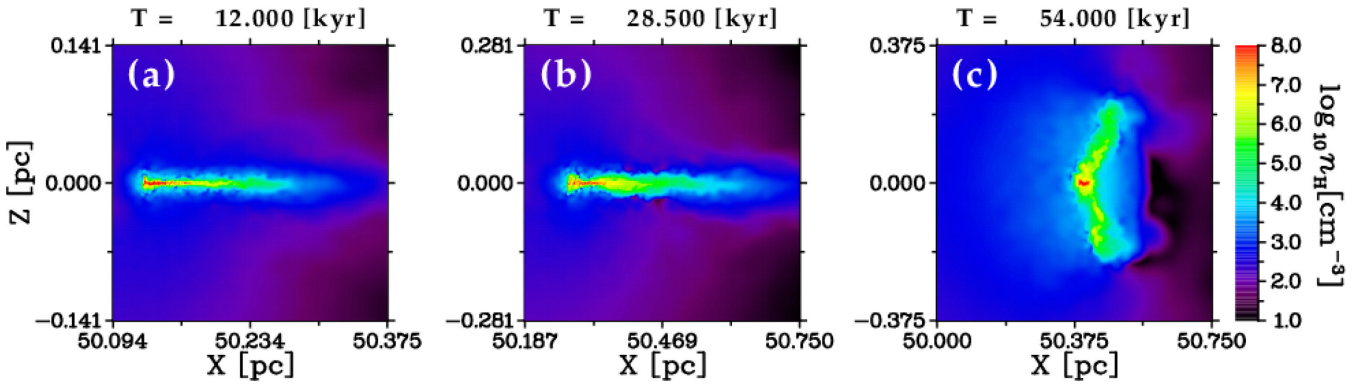

Figure 9. Enlarged views of Figs 8(d), (h) and (l). Note that the upper limit of the colour bar is different from Fig. 8.

formation of the shocked layer at a very early time. The photoevaporation flow launched from the shocked layer interacts with the incident photons. Since the total force, which is mainly sum of the pressure-gradient force and the radiation force (the self-gravity is much smaller than these), is parallel to the x-axis near the central part of the irradiated face, the photoevaporation flow cannot expand in the direction of the AGN. On the other hand, at the outskirts of the irradiated face (at the distance of $\approx r_{\rm cl}$ from the x-axis), the radiation force bends the photoevaporation flow in the opposite direction of the AGN (e.g. Fig. 12a). Thus, the radiation pressure stripping occurs. We can verify these things in the left-hand panel of Fig. 14 in which the acceleration fields of model H20 at $t = 90$ kyr is shown.

The shocked layer moves in the direction opposite to the AGN, keeping its shape almost flat except for $\mathcal{N}_{\rm S} = 5$ case, which shows an evolution similar to those of Low-$\mathcal{U}$ models. For model H20, $\overline{v}_{\rm sh}$ is almost constants until it crosses the cloud and is $\approx$22 km s^{-1}, which is roughly consistent with $v_{\rm sh}^{\rm app}(L_{\rm bol} = 5 \times 10^{44}) \approx 18.8$ km s^{-1}. For model H05, $\overline{v}_{\rm sh} \approx 21$ km s^{-1}. Thus, $\overline{v}_{\rm sh}$ is nearly independent of $\mathcal{N}_{\rm S}$ in High-$\mathcal{U}$ models and the rocket effect seems to not be effective compared to Low-$\mathcal{U}$ models.

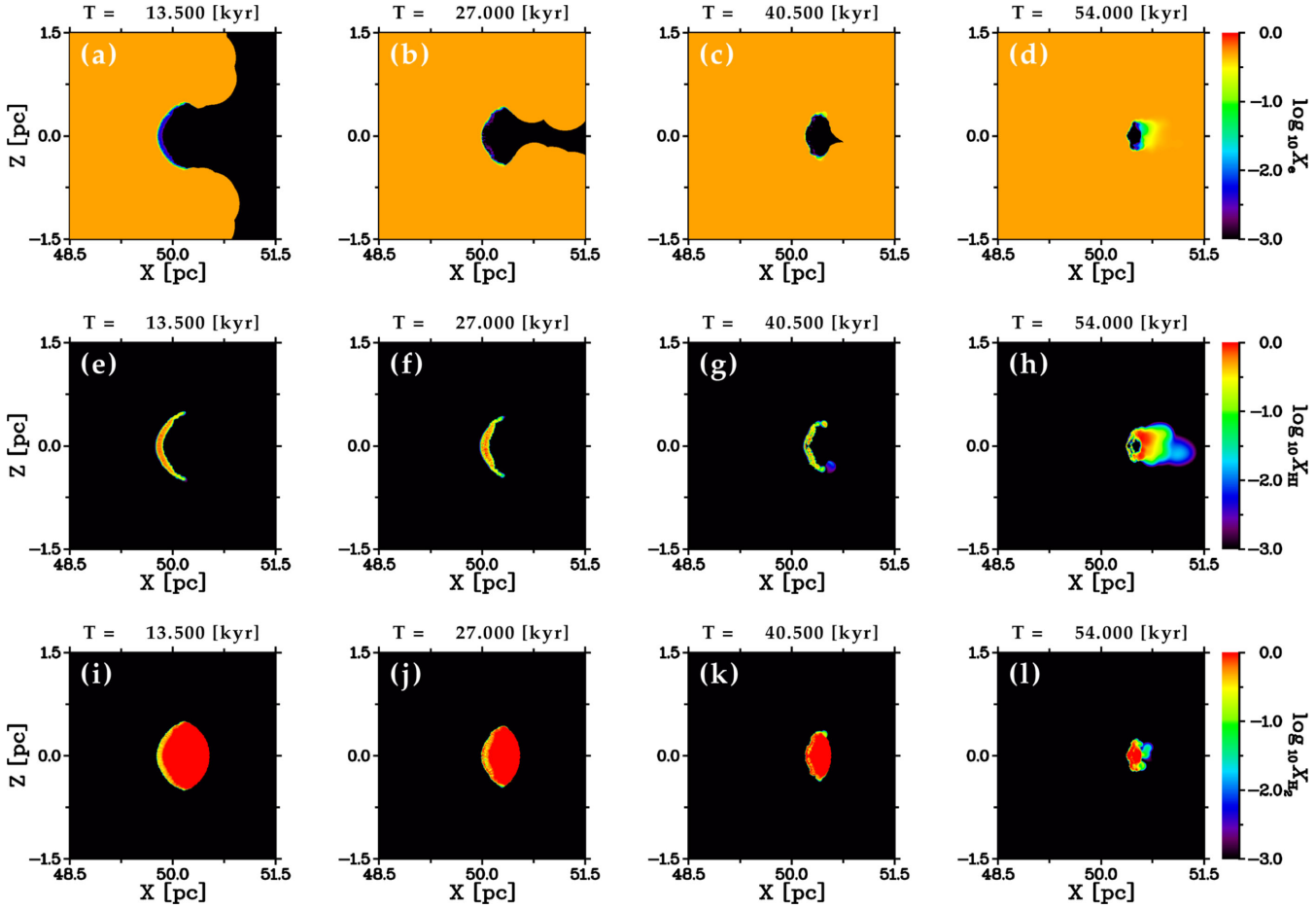

Figure 10. Time evolution of the number fraction X_i of model L20 at the $y = 0$ slice. From the tow row to the bottom row, X_e, $X_{\rm H_I}$ and $X_{\rm H_2}$ are shown.

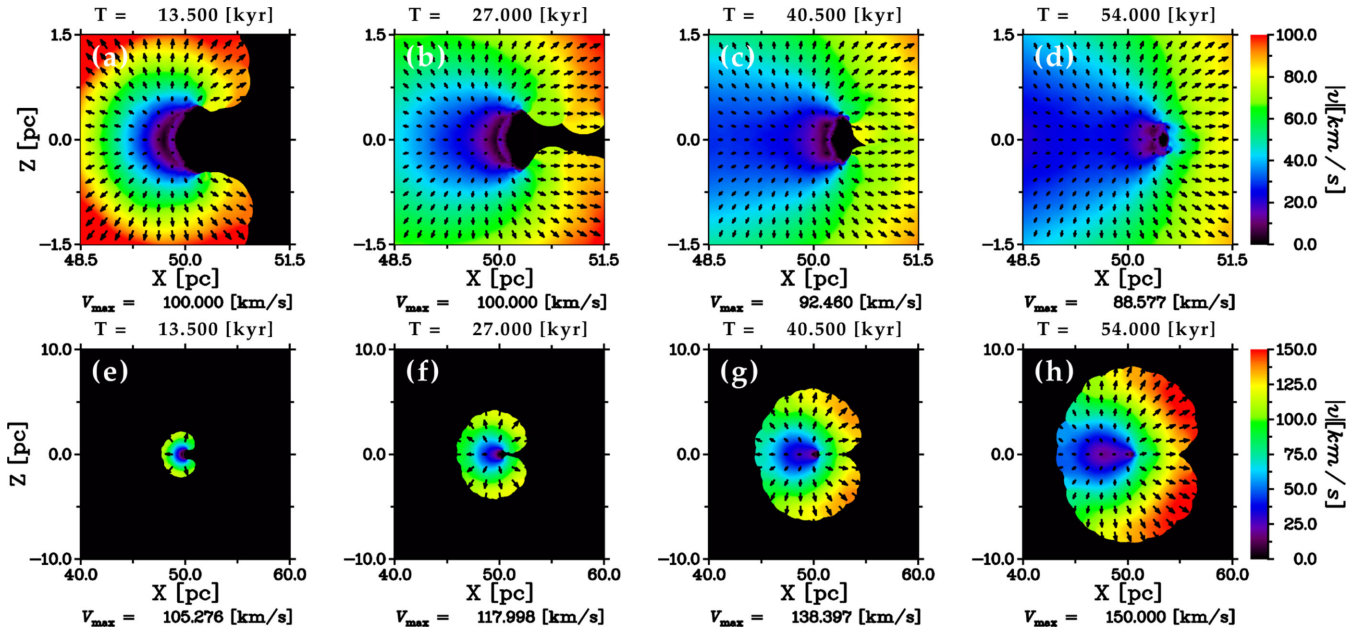

Figure 11. Time evolution of the velocity fields of model L20 at the $y = 0$ slice. The lower panels are extensive versions of the upper panels. The black arrow show the velocity vector projected on to the xz plane and the maximum arrow length corresponds to $v_{\rm max}$ which is described in the bottom of each panel.

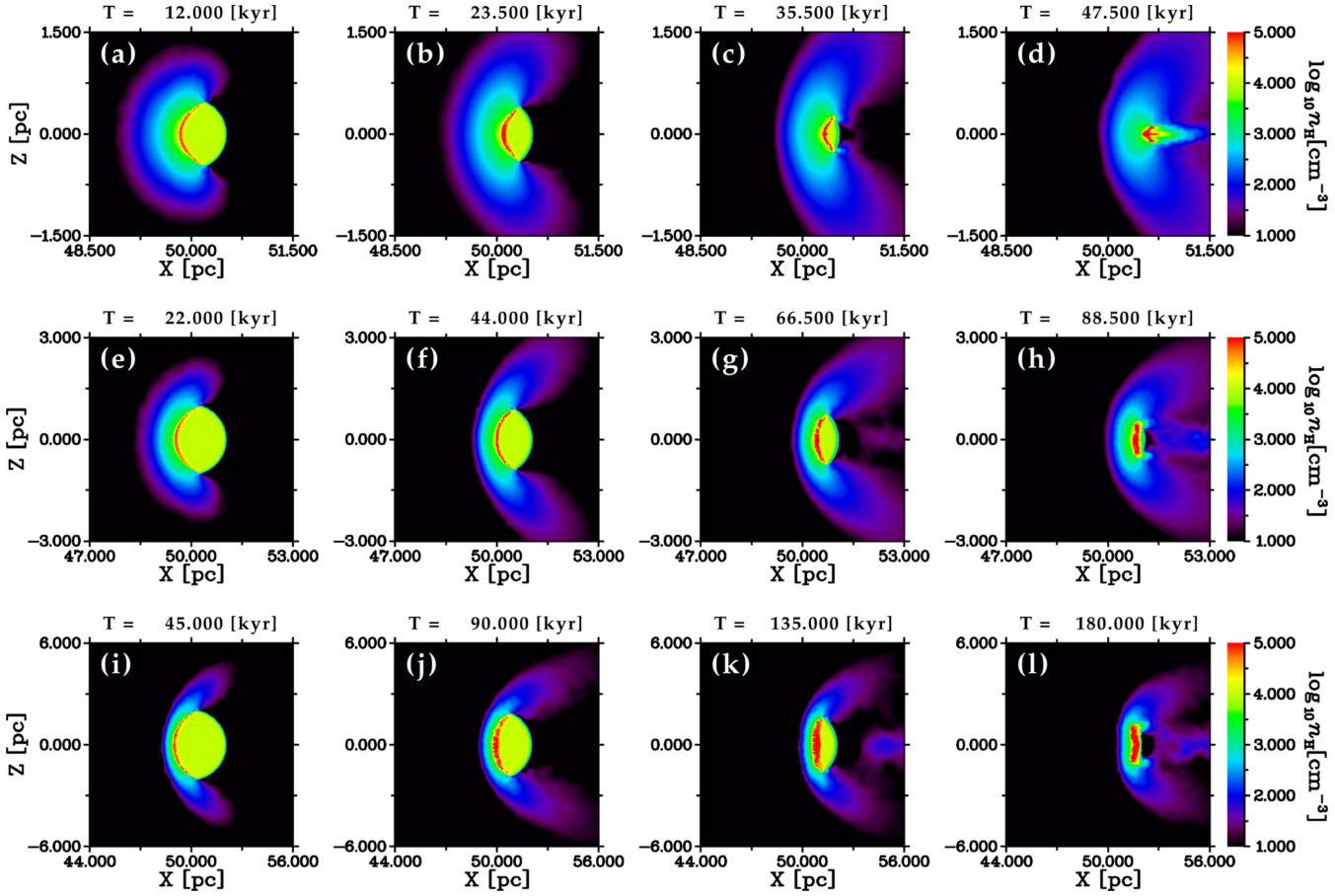

Figure 12. The same as Fig. 8, but for High-$\mathcal{U}$ models (top: H05, middle: H10, bottom: H20).

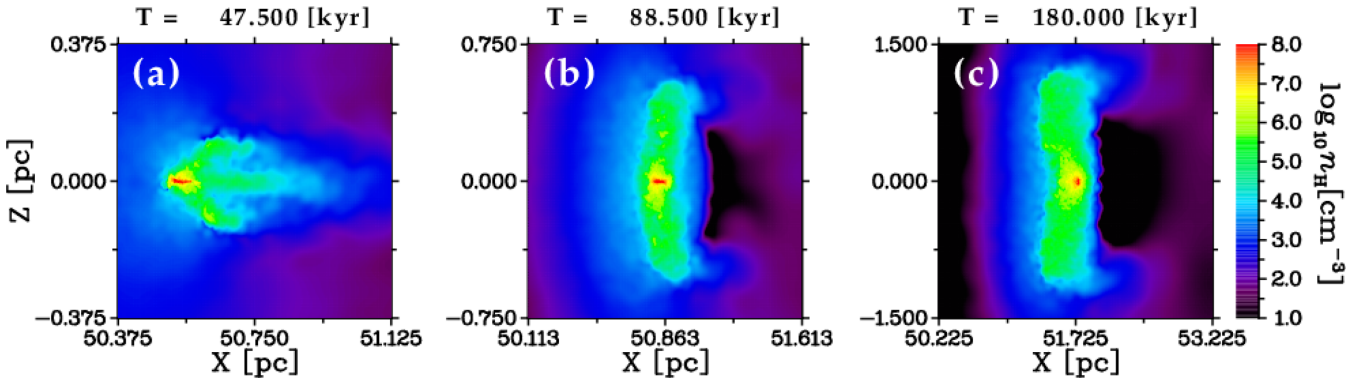

Figure 13. Enlarged views of Figs 12(d), (h) and (l). Note that the upper limit of the colour bar is different from Fig. 12.

The mass and thickness of the shocked layer gradually increases with time. At a later time, the unirradiated part of the shocked layer becomes self-gravitationally unstable and some part of gas start to collapse. This is seen in Fig. 15 which shows the time evolution of $n_{\rm H}-T_{\rm gas}$ plane of model H20. At $t = 180$ kyr, a part of gas move towards an upper-right direction in the $n_{\rm H}-T_{\rm gas}$ plane along the line that corresponds to the temperature floor equation (51). This migration occurs because the mass of the self-gravitationally unstable gas increases with time and therefore a higher pressure is progressively needed to support the cloud. All of the gas with $n_{\rm H} > 10^8\,{\rm cm}^{-3}$ concentrates into a single gas clump, which is located at (51.76 pc, 0, 0) and has a disc-like shape whose major axes lie in the yz plane. The total mass and the diameter of this clump are 211 $M_\odot$ and 0.084 pc, respectively. The hydrogen column density for the clump is $N_{\rm col}^{\rm H} > 5.5 \times 10^{24}\,{\rm cm}^{-2}$. Because of extremely high column densities, X-ray heating by the AGN, whose effect is not included in our simulations, will have little influence on the clump even if we take it into account. If we assume $T_{\rm gas} = 20$ K and $\mu = 2$ as in a normal pre-stellar core, the Jeans mass is $\approx$0.26 $M_\odot$ for $n_{\rm H} = 10^8\,{\rm cm}^{-3}$, which is much smaller than the total mass of the clump. Therefore, this clump will collapse and fragment into small subclumps if we remove the temperature floor.

The chemical structure and the velocity fields of model H20 are shown in Figs 16 and 17, respectively. The stripped flow is fully

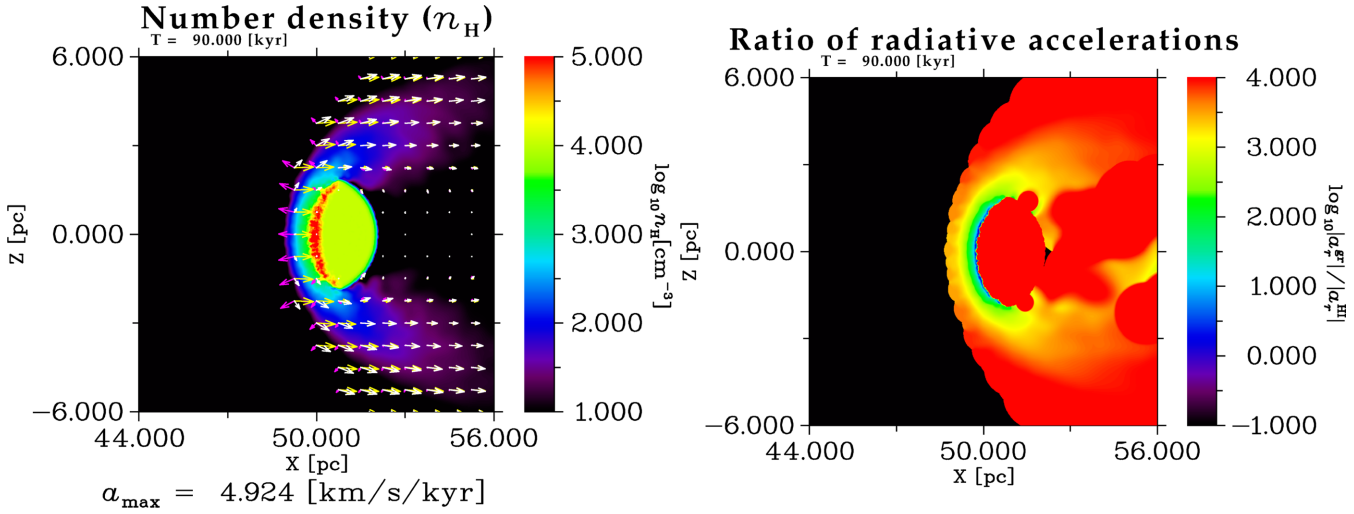

Figure 14. The acceleration fields (*left*) and $|\boldsymbol{a}_{\rm rad}^{\rm gr}|/|\boldsymbol{a}_{\rm rad}^{\rm H_I}|$ (*right*) at $t = 90$ kyr in model H20. In the left-hand panel, the arrows show the total acceleration (*white*), the pressure-gradient acceleration (*magenta*), and the radiative acceleration (*yellow*). The maximum arrow length corresponds to the value described on the bottom of the panel.

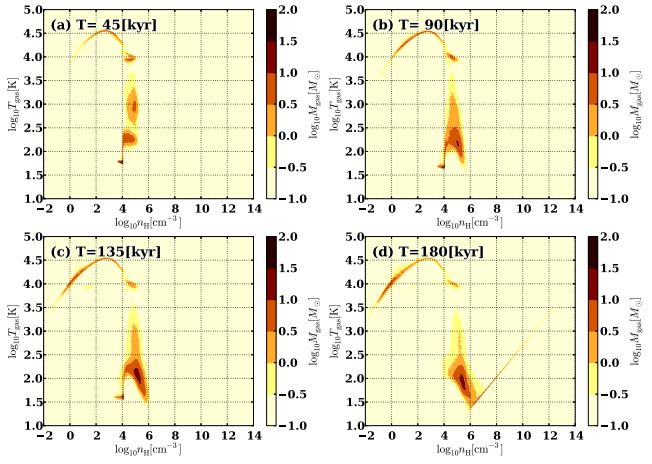

Figure 15. Time evolution of the $n_{\rm H}$–$T_{\rm gas}$ diagram of model H20. Each panel has 256^2 pixels and the colour of the pixel shows the gas mass contained in the pixel.

ionized and the velocity of the flow increases to $\approx$200 km s^{-1} by it reaches a distance of $\sim r_{\rm cl}$ from the cloud surface. In order to show contributions of H I-photoionization and dust absorption in accelerating the flow, we plot in the right-hand panel of Fig. 14 the spacial distribution of $|\boldsymbol{a}_{\rm rad}^{\rm gr}|/|\boldsymbol{a}_{\rm rad}^{\rm H_I}|$ of model H20 at $t = 90$ kyr. It is clear from the figure that the stripped flow is dominantly accelerated by the dust absorption. As in Low-$\mathcal{U}$ models, a part of the stripped flow comes around the shocked layer and becomes neutral. The velocity of the neutral flow is $\lesssim$100 km s^{-1}.

4.4 SC models

Here, we first explain the simulation conditions of model SC00-3D. The cloud has an uniform number density of 6×10^4 cm^{-3} and is located at a distance of 5 pc from an AGN. Its radius and mass are 1 pc and $\approx 6 \times 10^3$ M$_\odot$. We assume the same initial gas and dust temperatures, namely $T_{\rm gas} = 100$ K and $T_{\rm gr} = 20$ K. Given this temperature, the Jeans length $\lambda_{\rm J}$ is $\approx$0.55 pc. Therefore, the cloud is initially self-gravitationally unstable. The cloud is initially at rest.

After starting of the simulation, the cloud starts to fall towards a galactic centre (GC) in a fixed external gravitational potential of an SMBH and a nuclear star cluster (NSC). In this study, both components are modelled by the Plummer models as follows:

$$\Phi_{\rm ext}(r) = -\frac{GM_{\rm BH}}{\sqrt{r^2 + b_{\rm BH}^2}} - \frac{GM_{\rm NSC}}{\sqrt{r^2 + b_{\rm NSC}^2}}, \tag{53}$$

where G is the gravitational constant, $M_{\rm BH} = 8 \times 10^6$ M$_\odot$, $b_{\rm BH} = 0.1$ pc, $M_{\rm NSC} = 2.2 \times 10^8$ M$_\odot$, and $b_{\rm NSC} = 25$ pc. The simulation conditions described above are almost the same as those of SC00 in Schartmann et al. (2011).[6] In order to obtain a higher column density resolution, the number of SPH particles of 2^{21} is used in this model.

We first perform the numerical simulation of model SC00-3D *without* the external gravity to make clear the effect of it and to compare the result with those of Low-$\mathcal{U}$ and High-$\mathcal{U}$ models. Next, we perform the simulation with the external gravity. Hereafter, we call these runs SC00-3D-static and SC00-3D-ff, respectively. We note that in SC00-3D-static, the cloud does not move towards the GC because of no external gravity.

Figs 18 and 21 show the time evolution of the number density distribution of SC00-3D-static and SC00-3D-ff, respectively. From these figures, it is obvious that the radiation pressure plays a dominant role in the evolution of the cloud. Because of very intense radiation pressure, no photoevaporation occurs in both runs, although the gas stripped by the radiation pressure from the cloud edge is promptly photoionized.

In SC00-3D-static, the cloud is simply destroyed by the passage of the shock driven by the radiation pressure. The shocked layer keeps its shape flat until it reaches the end of the cloud. The time-averaged velocity of the shock is $\overline{v}_{\rm sh} \approx 37.7$ km s^{-1}, which is in good agreement with the estimated value by the razor-thin approximation, 35 km s^{-1} (equation 15). As the shock sweeps the gas, the mass of the post-shocked layer grows with time. Consequently, the

[6] The exception is the treatment of the gravitational potential of the SMBH. In their study, the SMBH is modelled by the Newtonian potential. The reason why we replace this by the Plummer potential is simply to avoid diverging the external gravity to infinity at the origin.

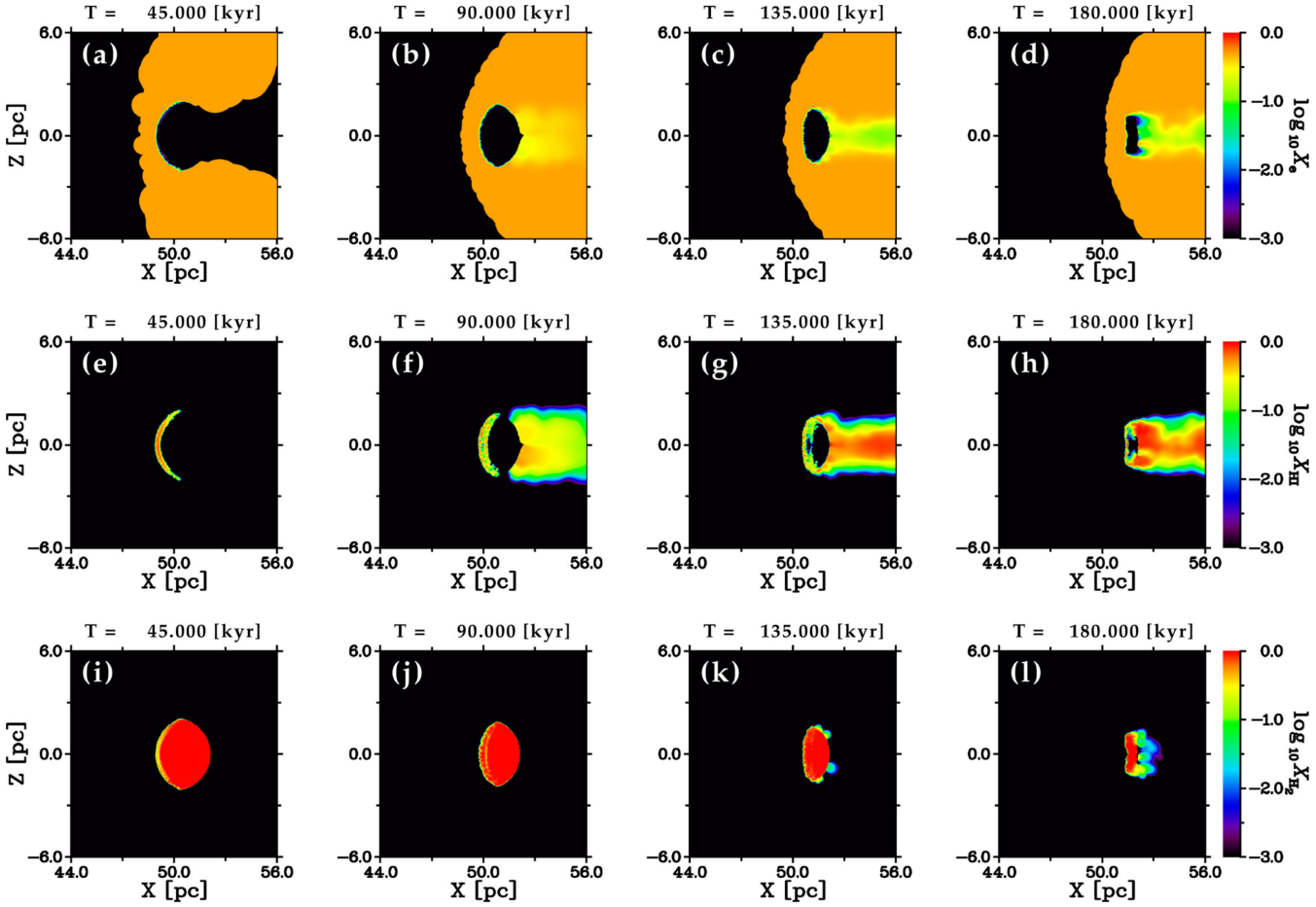

Figure 16. The same as Fig. 10, but for model H20.

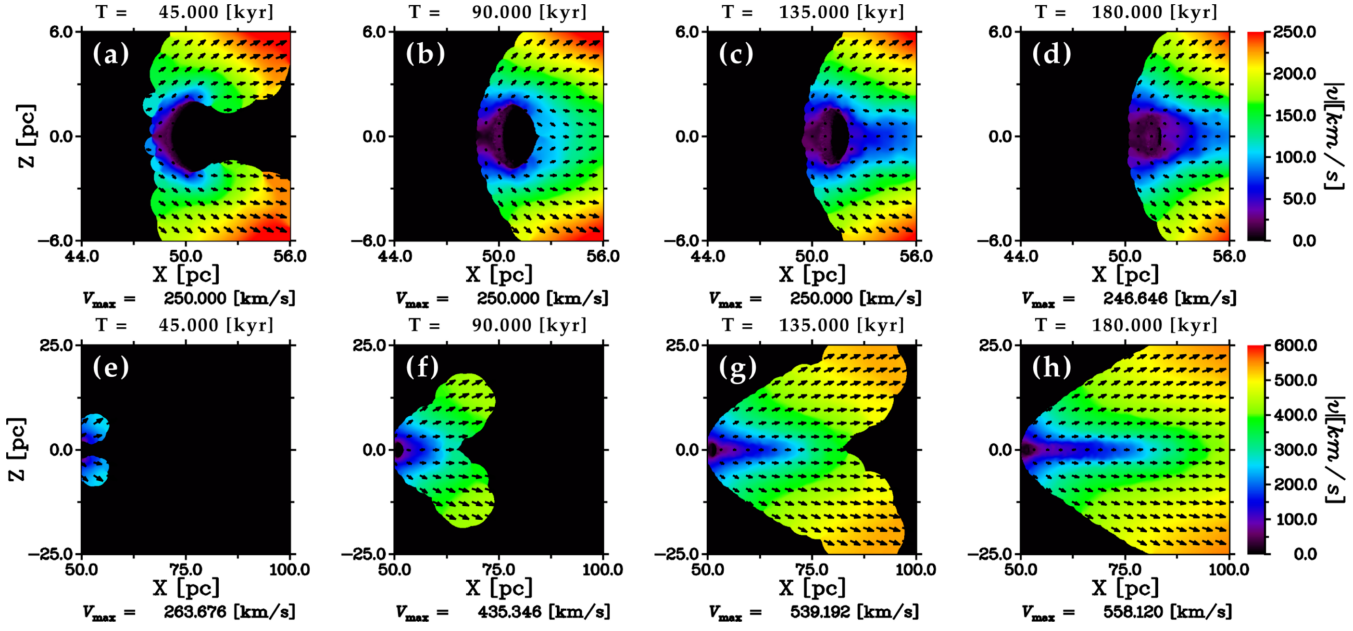

Figure 17. The same as Fig. 11, but for model H20.

shocked layer fragments into gas clumps and gas filaments by the self-gravitational instability (Figs 18c and d). This is more clearly seen in the column density distribution in the *yz* plane at $t = 53$ kyr (Fig. 19). The distinct filamentary structure is developed over the entire cloud. The points of junction of the filaments are beginning to collapse self-gravitationally at $t = 53$ kyr as shown by $n_{\rm H}$–$T_{\rm gas}$ diagram at $t = 53$ kyr (Fig. 20). It is interesting to examine further evolution of this filamentary structure, since the stellar IMF

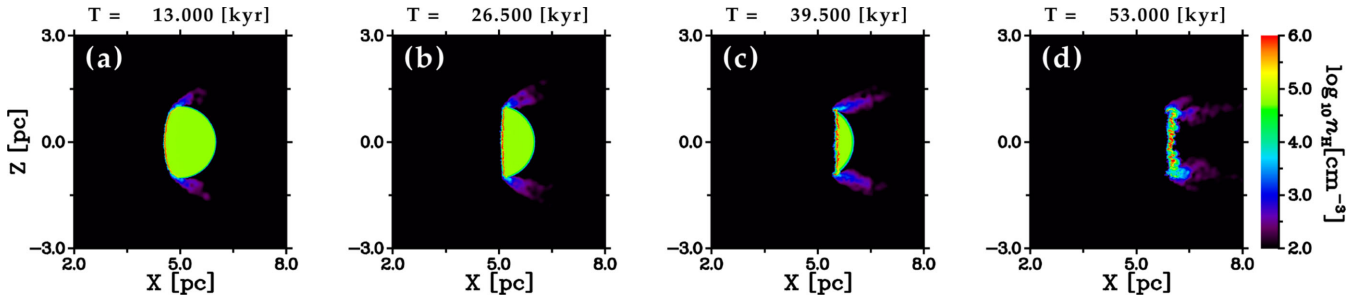

Figure 18. The same as Fig. 8, but for model SC00-3D-static.

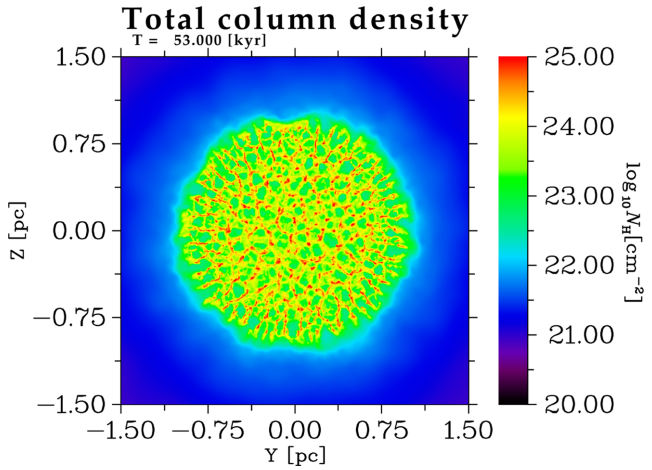

Figure 19. The column density distribution of model SC00-3D-static in the yz plane at $t = 53$ kyr.

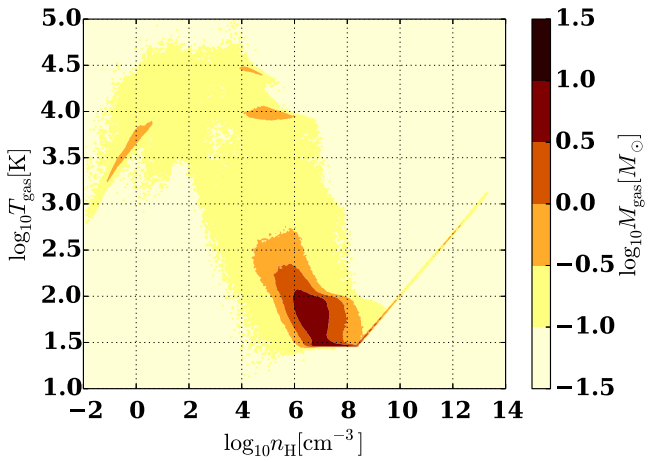

Figure 20. The $n_{\rm H}$–$T_{\rm gas}$ diagram of model SC00-3D-static at $t = 53$ kyr.

becomes potentially top heavy via the selective destruction of low column density regions due to the radiation pressure.

By contrast with SC00-3D-static, SC00-3D-ff shows a different evolution. During the initial 33 kyr, the evolution of the cloud is similar to that of SC00-3D-static, but the propagation of the shock in the cloud is slower than that of SC00-3D-static. This slowdown is more prominent in the later stage of the simulation (e.g. Figs 21e, f and g). Two mechanisms cause this slowdown. One is the radial component of the gravity and the other is the gravity in the traverse direction. Because the external gravity is stronger at smaller radius, the region between the shock (the near-side edge) and the far-side edge of the cloud is stretched as the cloud approaches the GC. In other words, the velocity of the shock is smaller in a comoving frame of the pre-shock gas than that in SC00-3D-static. In addition to this, the gradual increase of the averaged density of the cloud, which is caused by the transverse components of the total gravity, also becomes a factor for the slowness of the shock (see equation 15). As a result, there exists the pre-shock gas at $t = 66$ kyr in SC00-3D-ff, while all the gas is swept by the shock till $t = 53$ kyr in SC00-3D-static. In this sense, the slowdown of the shock propagation results in a slight increase of the longevity of the cloud (10–20 per cent in this particular model). However, the surviving pre-shock gas will be collapsed along the transverse direction eventually in a short time and star formation is expected to be unavoidable. What fraction of the gas is supplied to the AGN accretion disc depends on the star formation rate in the cloud.

Finally, we compare SC00-3D-ff with SC00 in Schartmann et al. (2011). The overall evolution of SC00-3D-ff is similar to SC00, but there are several differences between them. First, the stripped gas is more diffuse in SC00-3D-ff than SC00, because it is rapidly photoionized. By the same reason, long radial filaments found in SC00 are not formed in SC00-3D-ff. Secondly, because the stripped gas expands into a region behind the cloud, a tail-like gas structure is formed there in SC00-3D-ff (Fig. 21h), which is not seen in SC00. Thirdly, which is most important, owing to the self-gravity and three-dimensionality, a great deal of gas of the cloud concentrates into the central region of the cloud in SC00-3D-ff compared to SC00. This alters the density distribution of the cloud and enhances the slowdown of the shock. As a result, there are undamaged gas at $t = 66$ kyr. In contrast, in SC00, all the gas is affected by the AGN radiation by $t = 60$ kyr. Thus, the self-gravity and three-dimensionality will enhance the gas supply rate to the galactic centre.

4.5 Cloud evaporation and cloud destruction time-scale

In order to see the dependences of mass-loss rates on $\mathcal{U}$ and $\mathcal{N}_{\rm S}$ quantitatively, we plot in Fig. 22 the time evolution of dense gas fraction $f_{\rm dense} \equiv M_{\rm gas}(>n_{\rm H}/2)/M_{\rm cl}$, where $M_{\rm gas}(>n_{\rm H}/2)$ is the total mass of the gas that has a larger density than half of the initial density $n_{\rm H}$. $f_{\rm dense}$ decreases with time in all the models and the decreasing rate is smaller in larger $\mathcal{N}_{\rm S}$ model if $\mathcal{U}$ are the same. In Low-$\mathcal{U}$ models, the deceasing rates become small gradually with time, since the counteraction of the photoevaporation compresses the gas cloud three-dimensionally and the geometric surface area that irradiated directly by the AGN becomes small with time. Because of this, $f_{\rm dense}$ in models L05 and L10 saturate since $t = 1.2t_{\rm sc}$ and $1.4t_{\rm sc}$. At the end of the simulations, $f_{\rm dense} \approx 0.4$, 0.5, 0.6 for $\mathcal{N}_{\rm S} = 5$, 10, 20, respectively. In High-$\mathcal{U}$ models, $f_{\rm dense}$ also decrease but almost linearly with time except for $\mathcal{N}_{\rm S} = 5$ case. Main reason of the difference in the dependence of $f_{\rm dense}$ on $\mathcal{U}$ is the confinement

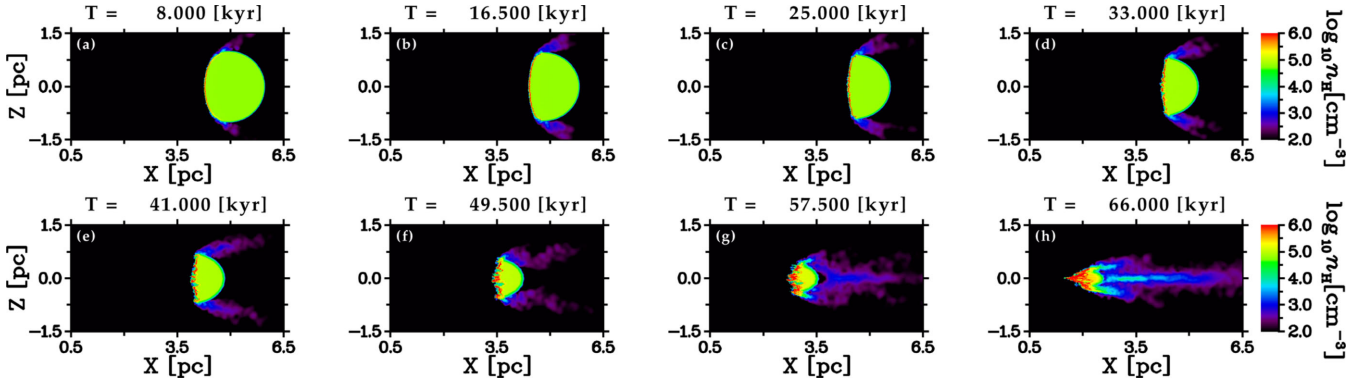

Figure 21. The same as Fig. 8, but for model SC00-3D-ff.

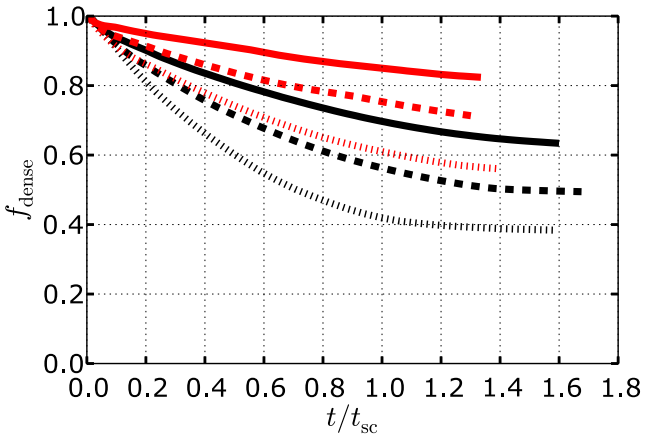

Figure 22. The time evolution of the mass fraction of dense gas (black dotted: L05, black dashed: L10, black solid: L20, red dotted: H05, red dashed: H10, red solid: H20). The calculation time is normalized by $t_{\rm sc}$.

effect by the radiation pressure as pointed out by Pier & Voit (1995). At the ends of the simulations, $f_{\rm dense} \approx 0.6, 0.7, 0.8$ for $\mathcal{N}_{\rm S} = 5$, 10, 20, respectively. Thus, the fractional mass-loss rates are smaller for High-$\mathcal{U}$ at least until $t \lesssim t_{\rm sc}$. However, $f_{\rm dense}$ in models H10 and H20 will decrease further for a while if we continue the simulations and then they will be saturated finally, because the clouds should be compressed by the counteraction of the stripped flow and their geometric cross-sections that absorb the AGN radiation should become small (compare, e.g. Fig. 12g and Fig. 12h).

Cloud destruction time-scale $t_{\rm dest}$ is determined by $2r_{\rm cl}/\overline{v}_{\rm sh}$. In higher $\mathcal{U}$ cases (High-$\mathcal{U}$ and SC00-3D models), $t_{\rm dest} \approx t_{\rm sweep}$ because of $\overline{v}_{\rm sh} \approx v_{\rm sh}^{\rm app}$. On the other hand, in lower $\mathcal{U}$ cases (Low-$\mathcal{U}$ models), $t_{\rm dest}$ is smaller than $t_{\rm sweep}$ because $\overline{v}_{\rm sh}$ is larger than $v_{\rm sh}^{\rm app}$ due to the rocket effect. In terms of $t_{\rm sc}$, $t_{\rm dest}/t_{\rm sc}$ is in the range of 1−2 (Fig. 22) for $(\mathcal{U}, \mathcal{N}_{\rm S})$ that is examined in this study.

5 DISCUSSIONS

In this section, we first discuss uncertainties in our numerical results in Section 5.1. Then, we compare our numerical results with previous studies in terms of cloud destruction process in Section 5.2. After that, in Section 5.3, we discuss the possibility of star formation in AGN-irradiated gas clouds. Finally, we give some implications for gas clumps in AGN tori in Section 5.4.

5.1 Uncertainties

In this paper, we used a highly simplified initial cloud model. In reality, gas clouds are not spherical and must have internal density structure and (turbulent) velocity fields. In addition, they should have orbital and spin angular momenta and be surrounded by a low-density gas if the clouds are initially in the pressure equilibrium. Furthermore, we neglected helium and metals for simplicity. Here, we discuss the possible effects on the evolution of the clouds, if these factors are taken into account.

5.1.1 Effects of chemical abundance and diffuse photons

In this study, we assumed that ISM consists of hydrogen and dust grains only and neglected helium and metals. However, actual ISM contains helium and metals. These elements enhance the cooling rate of gas significantly in a wide range of gas temperature. Therefore, the gas temperatures in the photoevaporation flow and in the shocked layer will be dropped to lower values compared to the cases presented in this paper. This may result in a decrease of photoevaporation rate and facilitate self-gravitational fragmentation of the shocked layer. Also, helium and metals increase the opacity of ISM by photon absorption by an enormous number of bound–bound/bound–free transitions. This enhancement may promote the confinement of the photoevaporation flow, which is seen in higher $\mathcal{U}$ cases. In addition, we did not take into account size distribution of dust grains and propagation of diffuse photons (scattered and re-emitted photons). These will also affect the evolution of the clouds to some extent. Especially, analytic and numerical studies pointed out that photon scattering is potentially capable of increasing radiative acceleration (e.g. Lamers & Cassinelli 1999; Roth et al. 2012). In the following, we examine the possibilities discussed above by using the photoionization calculation code CLOUDY (version C13.03, last described by Ferland et al. 2013). In all the photoionization calculations described below, we assume (1) that the gas is at the rest, (2) that the hydrogen number density distribution is the same as that along the x-axis of model L20 at $T = 54$ kyr and (3) that the incident radiation field is the same as that used for model L20.

Before doing the photoionization calculations, we first check if the dust absorption and scattering coefficients used in the CLOUDY is similar to those used in this study, since a difference affects the interpretation of the results. With this aim, we make the data of absorption and scattering coefficients for a silicate grain with $a_{\rm gr} = 0.05$ μm by the `compile grains` command of the CLOUDY. The coefficients are shown in Fig. 4 by the cyan lines. This figure

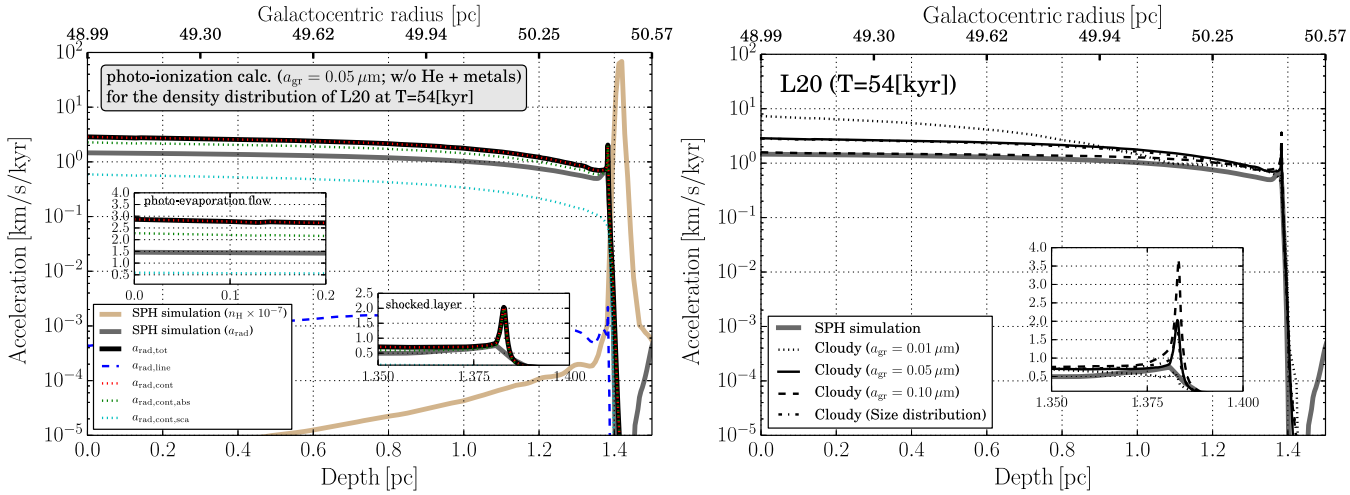

Figure 23. Left: a comparison of the radiative acceleration along the x-axis of model L20 at $T = 54$ kyr with that obtained by the photoionization calculation with the CLOUDY. Each component of the radiative acceleration are shown by different lines (thick black solid line: total radiative acceleration, blue dashed line: line radiative acceleration, red dotted line: continuum radiative acceleration, green dotted line: contribution of absorption for continuum radiative acceleration, cyan dotted line: contribution of scattering for continuum radiative acceleration). The hydrogen number density distribution used in the photoionization calculation is plotted by the brown solid line. Right: total radiative accelerations for different dust grain sizes. Four different dust size distributions are plotted (three are single-sized dust grains of $a_{gr} = 0.01, 0.05, 0.1$ μm and the other is the standard size distribution used in the CLOUDY). In both panels, the accelerations are plotted as a function of distance from the illuminated face (lower horizontal axis) or from the AGN (upper horizontal axis). The small insets in the figures are enlarged views and their vertical axes are linear scale. In the photoionization calculations, we assume that an ISM consists of hydrogen and silicate dust grains only and the dust abundance is adjusted so that $f_{gr} = 0.01$.

shows that the dust properties used in the CLOUDY is very similar to those in our study.

To discriminate the effects of the diffuse photons, we perform a photoionization calculation assuming that ISM consists of hydrogen and dust grains only. The spacial distribution of the radiative acceleration obtained by the calculation is shown, together with that in the SPH simulation, in the left-hand panel of Fig. 23. This figure shows that in the photoevaporation flow, the total radiative acceleration in the SPH simulation ($\approx$1.5 km s^{-1} kyr^{-1}) is a factor of $\approx$2 lower than that in the photoionization calculation ($\approx$3 km s^{-1} kyr^{-1}). A part of this difference ($\approx$0.5 km s^{-1} kyr^{-1}) is explained by a scattering component of the continuum radiative acceleration.[7] The remaining difference may be explained by absorption of diffuse photons. At the shocked layer, the SPH simulation underestimates the total radiative acceleration by a factor of 3−4. This is partly attributed to the deficiency of numerical resolution and the fact that our numerical scheme is not photon conservative. Another reason may be that we did not take into account the absorption of diffuse photons in the SPH simulations. These analyses suggest that $\overline{v}_{sh}$ becomes larger and the photoevaporation rate becomes smaller than those in the SPH simulations presented in Section 4 if the diffuse photons is taken into account.

Next, we perform the photoionization calculations for different grain size to check the effects of grain size. Three single-sized grains ($a_{gr} = 0.01$, 0.05 and 0.1 μm) and the standard size distribution used in the CLOUDY are assumed. The spacial distributions of the total radiative acceleration for different grain sizes are shown in the right-hand panel of Fig. 23. This figure shows that the total radiative acceleration for the $a_{gr} = 0.05$ μm case is almost identical to that for the standard size distribution. This is probably because a mean grain size $\langle a_{gr}\rangle$ of 0.05 μm approximately satisfies the following relation:

$$n(\langle a_{gr}\rangle)\int \frac{L_\nu}{4\pi r^2}\mathcal{Q}_{abs}(\nu,\langle a_{gr}\rangle)\pi\langle a_{gr}\rangle^2 d\nu$$

$$= \iint \frac{L_\nu}{4\pi r^2}\mathcal{Q}_{abs}(\nu,a_{gr})\pi a_{gr}^2 n(a_{gr})d\nu da_{gr}, \quad (54)$$

where $n(a_{gr})da_{gr}$ is the number density of dust grain between a_{gr} and $a_{gr} + da_{gr}$ and $n(\langle a_{gr}\rangle) \equiv \int(\frac{4}{3}\pi a_{gr}^3\rho_{gr}n(a_{gr}))/(\frac{4}{3}\pi\langle a_{gr}\rangle^3\rho_{gr})da_{gr}$. Assuming that $\int \frac{L_\nu}{4\pi r^2}\mathcal{Q}_{abs}(\nu,a_{gr})d\nu$ depends weakly on a_{gr} and introducing $\overline{a_{gr}^n} = \int a_{gr}^n n(a_{gr})da_{gr}/\int n(a_{gr})da_{gr}$, equation (54) can be rewritten as

$$\langle a_{gr}\rangle \approx \overline{a_{gr}^3}/\overline{a_{gr}^2}. \quad (55)$$

For the standard size distribution used in the CLOUDY, $\overline{a_{gr}^3}/\overline{a_{gr}^2} = 0.0354$ μm, which is close to 0.05 μm. Thus, the $a_{gr} = 0.05$ μm model, which is assumed in the SPH simulations in this paper, is a good approximation at least in respect of radiative acceleration and the evolution of the clouds will not be altered largely if we adopt a standard size distribution.

Finally, we examine the effects of helium and metals. To this end, we perform a photoionization calculation taking into account these elements, but assuming a single-sized silicate grain of $a_{gr} = 0.05$ μm. The gas-phase abundance assumed in the calculation is shown in Table 5. This abundance pattern is similar to the CLOUDY's abundance set `ISM` except that (1) the abundance is increased by a factor of 1.75 so that $f_{gr} = 0.01$ and (2) carbon locked up in graphite grains is returned to the gas phase (no graphite grains is assumed). The spacial distribution of the radiative acceleration and gas and dust temperatures are shown in Fig. 24. By comparing the left-hand panel of Fig. 24 with that of Fig. 23, we can see that the radiative acceleration is smaller than that in the zero-metallicity case. This is mainly because (1) the mean molecular weight of ISM is increased by introducing helium and metals and (2) line

[7] In order to obtain absorption and scattering components of the continuum radiative acceleration, we customized `wind.h`, `pressure_total.cpp`, `parse_save.cpp` and `save_do.cpp` in the CLOUDY code.

Table 5. Elemental abundance in gas phase assumed in the photoionization calculation.

Element	Abundance[a]	Element	Abundance[a]
H	0.0	S	−4.246 462
He	−0.765 762	Cl	−6.756 962
Li	−10.02 456	Ar	−5.306 762
B	−9.807 562	K	−7.715 562
C	−3.033 152	Ca	−9.144 162
N	−3.857 162	Ti	−8.993 562
O	−3.256 613	V	−9.756 962
F	−7.455 962	Cr	−7.756 962
Ne	−3.667 062	Mn	−7.395 262
Na	−6.257 262	Fe	−9.614 866
Mg	−4.678 865	Co	−7.986 062
Al	−6.857 162	Ni	−7.496 862
Si	−5.353 955	Cu	−8.580 862
P	−6.552 862	Zn	−7.455 962

[a]$\log_{10}(n_X/n_{\rm H})$, where n_X is the number density of element X.

absorption by metals saturates easily without a large velocity gradient. The right-hand panel of Fig. 24 shows a comparison of the gas and dust temperatures between the SPH simulation and the photoionization calculation. Near the shocked layer, the gas temperature in the SPH simulation is a factor of 1.3 larger than that in the photoionization calculation. In the photoevaporation flow, the SPH simulation underestimates the gas temperature. To examine the source of these differences, we plot in Fig. 25 the spacial profile of the fraction of cooling (heating) rate of important processes to the total cooling (heating) rate. Near the shocked layer, emission lines by oxygen, neon and sulphur contributes largely to the total cooling rate. Helium plays a role in heating the ISM (Depth ≈1.38 pc). On the other hand, the photoevaporation flow is predominantly heated by the photoelectric heating by dust grains. Thus, metals decreases the pressure gradient in the ionized region at the irradiated face of the cloud and the photoevaporation rate will be smaller than those in the SPH simulations. For further details, RHD simulations taking into account helium and metals are necessary and we will address this in the future.

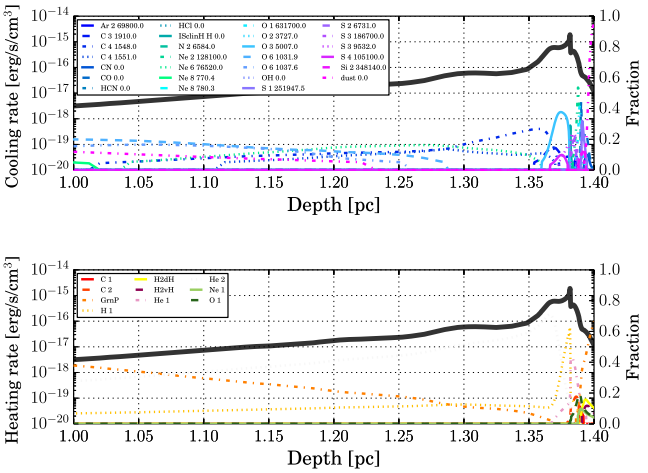

Figure 25. Spacial profiles of cooling rate and heating rate (thick dark grey lines in both panels) in the photoionization calculation shown in Fig. 24. The proportion of cooling (heating) rate of each process to the total cooling (heating) rate is shown by a coloured line. In the upper panel, if a label that starts with an element name, an integral number and a real number following the element name indicate the ionization stage and the wavelength of the emission, respectively. The labels that start with a molecular name indicates cooling by emissions from that molecule. The meaning of the other labels in the upper panel is as follows: `dust 0.0` is the thermal emission from dust grains; `ISclinH H 0.0` is a cooling due to the H isoelectronic sequence; in the lower panel, photoelectric heating by an element is indicated by a label beginning with the element name and followed by an integral number that indicates its ionization stage. The meaning of the other labels in the lower panel is as follows: `GrnP` is the photoelectric heating by dust grains; `H2dH` is the heating due to H_2 dissociation; `H2vH` is the heating due to collisions with H_2.

5.1.2 *Effects of surrounding medium*

In this study, we neglected the surrounding medium of the gas clouds. However, the gas clouds are actually confined by the surrounding medium if they are in the pressure equilibrium. The presence of the surrounding medium may affect the photoevaporation rates from the gas clouds. In order to check this possibility, we perform 1D spherically symmetric RHD simulations for different

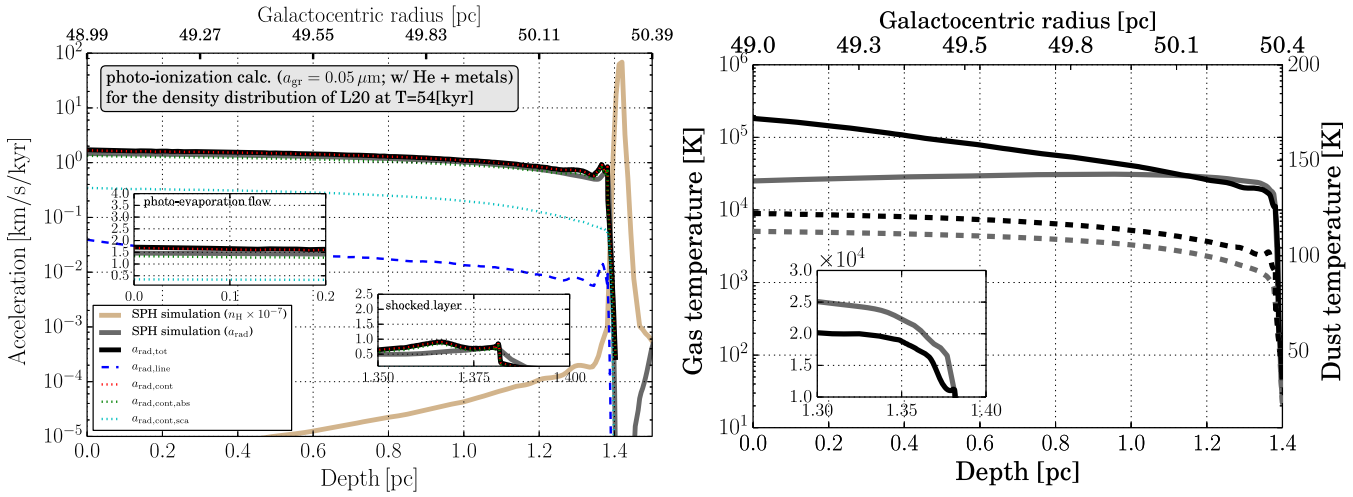

Figure 24. Left: the same as the left-hand panel of Fig. 23, but helium and metals are taken into account in this case. Right: a comparison of gas and dust temperature distributions between the SPH simulation (grey) and the photoionization calculation (black). The gas and dust temperatures are plotted by the solid lines and the dashed lines, respectively.

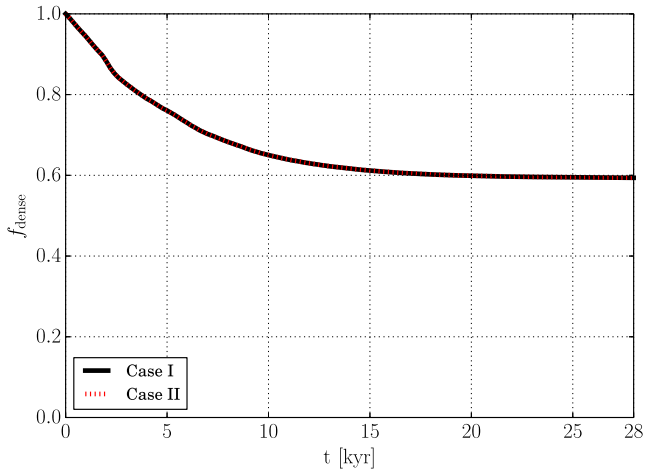

Figure 26. Time evolution of $f_{\rm dense}$ in the 1D spherically symmetric RHD simulations described in Section 5.1.2. The black solid line and the red dotted line indicate Case I and II, respectively. The 1D RHD simulations are stopped if the shock reaches the centre of the gas cloud.

densities of the surrounding medium. The details of the 1D RHD code will be presented elsewhere (Namekata et al., in preparation). Here, the following two cases are examined.

Case I: $n_{\rm H} = 10^{-4}\,{\rm cm}^{-3}$. This case mimics the vacuum condition assumed in the SPH simulations.

Case II: $n_{\rm H} \approx 8.33\,{\rm cm}^{-3}$. In this case, the gas cloud is initially in the pressure equilibrium with the ambient gas.

In both cases, the surrounding medium is assumed to be fully ionized gas. Its initial gas temperature and $f_{\rm gr}$ are set to be 3×10^4 K and 10^{-10}, respectively. The physical conditions of the gas cloud is the same as those of model L20.

Fig. 26 shows time evolution of $f_{\rm dense}$, which is defined in Section 4.5, in the 1D RHD simulations. $f_{\rm dense}$ in both cases are very similar to each other. Thus, the surrounding medium has little impact on the evolution of the gas clouds. Similarly, the results of the 1D RHD simulations for the other models listed in Table 1 do not depend on the density of the surrounding medium. However, if the surrounding medium contains dust grains with a normal abundance, a dusty gaseous shell, which will be formed at the front of the photoevaporation flow, would stop the photoevaporation when it becomes optically thick. A time for the photoevaporation to stop depends on the physical conditions of the surrounding medium, which should be determined by more realistic simulations.

5.1.3 *Effects of orbital and spin motions*

As we have shown in Section 4, the clouds are compressed in a time-scale $t_{\rm sc}$ for Low-$\mathcal{U}$ case or $t_{\rm sweep}$ for High-$\mathcal{U}$ case. We can neglect the orbital and spin motion of the clouds, if these time-scales are much shorter than the orbital and spin periods. In a typical galaxy, circular velocity $v_{\rm orb}$ is roughly $200\,{\rm km\,s}^{-1}$, if the cloud is far from the SMBH. Then, the orbital period is $t_{\rm orb} = 2\pi r/v_{\rm orb} \approx 1.57 \times 10^6\,{\rm yr}(r/50\,{\rm pc})$. For the clouds located at $r = 50\,{\rm pc}$, $t_{\rm orb}$ is much larger than both $t_{\rm sc}$ and $t_{\rm sweep}$ (see equation 14 and 17). The spin period $t_{\rm spin}$ has possibly the same order as the orbital period, if the cloud's spin is originated in the galactic shear,[8] although it is possible that the cloud spins up in the process of formation. Near an SMBH, these time-scales can be estimated as equation (69), (71), and (72) for a particular AGN case (see Section 5.4) and $t_{\rm orb}$ is larger than $t_{\rm sc}$ and $t_{\rm sweep}$ at $r = 1\,{\rm pc}$ (see also Fig. 30). Therefore, we conclude that the orbital motion and spin of the clouds do not affect largely the global evolution of the clouds. But, we note that the infall motion towards a galactic centre can affect the evolution of the cloud, if the cloud is initially located near the SMBH, because the tidal force increases significantly as the cloud approaches the galactic centre (see Section 4.4).

5.1.4 *Effects of density structure and velocity fields*

The shape of the cloud as well as the internal density structure and velocity fields are likely to have a great impact on how the cloud deformation occurs. Since we have assumed the spherical uniform cloud in this study, the counteraction of the photoevaporation flow direct towards the centre of the cloud in Low-$\mathcal{U}$ case, leading to formation of a dense filament along the symmetric axis of the cloud (x-axis in the simulation coordinate; see Figs 8d and h). This result likely changes if the cloud has a different shape and/or a density structure. The internal velocity fields also affect spin angular momenta of subclumps which will be formed by the self-gravitational instability in a later phase of the cloud evolution, which we cannot follow in this study because of very small timestep. The effects of these factors on the evolution of the clouds should be explored in the future.

5.1.5 *Other uncertainties*

In Low- and High-$\mathcal{U}$ models, we used the same SED assumed in Nenkova et al. (2008a); see equation (18). The extreme-UV part of this spectrum is steeper than average spectrum of radio-quiet quasi-stellar objects derived by Telfer et al. (2002). In order to check the effects of SED, we performed 1D spherically symmetric RHD simulations assuming the SED described by equation (19), which is more similar to the average spectrum. We found that the numerical results are hardly different from those in which the Nenkova SED is assumed. Therefore, we conclude that the shape of the SED does not affect the evolution of the gas clouds at least for the range of $(\mathcal{U}, \mathcal{N}_{\rm S})$ that are investigated in this paper.

5.2 Comparison to previous studies

Evolution of an irradiated gas cloud have been studied extensively by many authors in various fields other than the field of AGN. For early phase of galaxy formation, photoevaporation of a minihalo or a dwarf galaxy by the reionization photons have been discussed (e.g. Barkana & Loeb 1999; Shapiro, Iliev & Raga 2004; Susa & Umemura 2004a,b; Iliev, Shapiro & Raga 2005). In the context of star formation, photoevaporation of a gas clump or a protoplanetary disc that is exposed to a nearby massive young star is a subject of research (e.g. Oort & Spitzer 1955; Kahn 1969; Zel'dovich & Syunyaev 1969; Bertoldi 1989; Bertoldi & McKee 1990; Lefloch & Lazareff 1994; Draine & Bertoldi 1996; Johnstone, Hollenbach & Bally 1998; Störzer & Hollenbach 1999; Richling & Yorke 2000; Gorti & Hollenbach 2002; Susa & Umemura 2006; Motoyama,

[8] According to Kim, Ostriker & Stone (2002), the galactic shear velocity can be written as $\boldsymbol{v}_0 = -q\Omega x\,\hat{\boldsymbol{y}}$ in a local Cartesian reference frame, where Ω is the orbital frequency and $q = (4 - \kappa^2/\Omega^2)/2$ and $\kappa \equiv \{r\frac{{\rm d}\Omega^2}{{\rm d}r} + 4\Omega^2\}^{1/2}$ is the epicyclic frequency. Because of $q \sim \mathcal{O}(1)$, $t_{\rm spin} \approx 2\pi r_{\rm cl}/|-q\Omega r_{\rm cl}| \approx 2\pi/\Omega = t_{\rm orb}$.

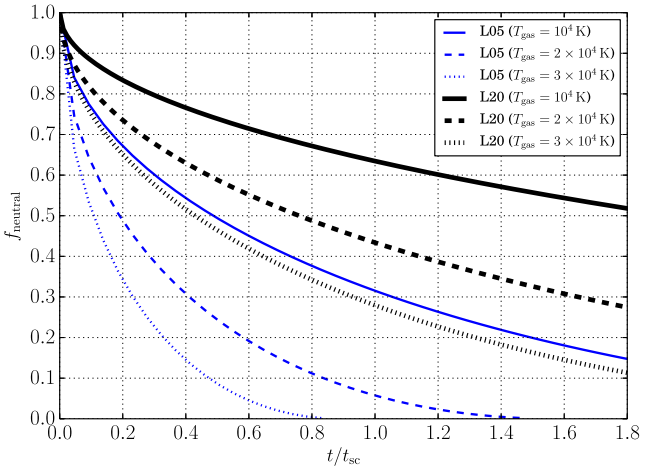

Figure 27. Time evolution of mass fraction of the neutral gas predicted by equation (58). Time is normalized by the sound crossing time, equation (14). The blue and black lines denote the predictions for models L05 and L20, respectively. The different line styles indicate the gas temperature of the ionized gas (see the legend in the figure for details). The ranges of both axis are adjusted to coincide with those of Fig. 22.

Umemoto & Shang 2007; Susa 2007; Susa, Umemura & Hasegawa 2009; Hasegawa, Umemura & Susa 2009). Here, we briefly compare the results of our study with those of some of previous studies in terms of cloud destruction time-scale.

Zel'dovich & Syunyaev (1969) derived a self-similar solution of outflow of ionized gas from an ionization front for the case when the optical thickness of the outflowing gas becomes important. The self-similar solution is written as

$$v = \frac{c_{\rm T}}{\sqrt{2}} + \frac{x}{t}, \tag{56}$$

$$n = \sqrt{\frac{\sqrt{2}F_{\rm ion}}{\alpha_{\rm B} c_{\rm T}}} t^{-1/2} \exp\left(-\frac{x}{\sqrt{2} c_{\rm T} t}\right), \tag{57}$$

where v is the velocity of the ionized gas, n is the number density of proton, $c_{\rm T}$ is the isothermal sound speed, $F_{\rm ion}$ is the number flux of ionizing photon, $\alpha_{\rm B}$ is the case B recombination coefficient, x is the distance from the ionization front and t is the time. The mass outflow rate at the front is given by

$$\rho v|_{\rm IF} = m_{\rm H} \frac{c_{\rm T}}{\sqrt{2}} \left(\frac{\sqrt{2}F_{\rm ion}}{\alpha_{\rm B} c_{\rm T}}\right)^{1/2} t^{-1/2}. \tag{58}$$

Using equation (58) and assuming that the outflowing gas streams along lines that connect between the radiation source and the front, we can estimate the photoevaporation rate for the cloud models described in Table 1. Fig. 27 shows the time evolution of the mass fraction of the *neutral* gas, $f_{\rm neutral}$. For a given gas cloud, $f_{\rm neutral}$ monotonically decreases with time and its decreasing rate is larger for higher gas temperature. Also, a smaller gas cloud loses neutral gas more rapidly as expected. The comparison of Fig. 27 with Fig. 22 shows that the time evolution of $f_{\rm neutral}$ is in disagreement with that of $f_{\rm dense}$. Especially, $f_{\rm neutral}$ does not saturate unlike $f_{\rm dense}$ and the mass of the neutral gas is underestimated. Thus, we should only use the self-similar solution by Zel'dovich & Syunyaev (1969) to obtain a rough estimate of photoevaporation time-scale from an spherical cloud that is irradiated from one direction.

Table 6. Comparison of $t_{\rm IS}$ with $t_{\rm end}$.

Model name	$t_{\rm IS}$ [a] (kyr)	$t_{\rm end}$ [b] (kyr)
L05	12.1	12
L10	28.9	28.5
L20	68.7	54
H05	48.6	47.5
H10	115	88.5
H20	274	180
SC00-3D	132	53

[a]The IS-front crossing time-scale defined by equation (59) where we assumed $c_{{\rm s},i} = 11.4\,{\rm km\,s^{-1}}$ as with Bertoldi (1989). A higher $c_{{\rm s},i}$ results in a lower $t_{\rm IS}$ because of $t_{\rm IS} \propto c_{{\rm s},i}^{-0.5}$.
[b]The times when the SPH simulations are stopped.

Bertoldi (1989) investigated the structure and evolution of a gas clump that is exposed to a nearby early-type star for a wide range of conditions by solving the steady-state hydrodynamic equations coupled with the ionization equations for hydrogen and helium. The clouds in Low- and High-$\mathcal{U}$ cases belong to the region III in his study (the clouds in our study have $\log\Gamma = -1.886$ to -1.284 and $\delta' = 0.2$ to 0.05 and see Fig. 1 in his study) and have the photoevaporation parameter $\psi \equiv \alpha_{\rm B} F_{\rm ion} r_{\rm cl}/c_{{\rm s},i}^2 > 10^6$, where $c_{{\rm s},i}$ is the gas temperature of ionized gas. Although a result for the case of $\psi > 10^6$ was not shown in his study, a simple extrapolation of the result for $\psi = 10^3$ and $\delta' = 10^{-0.5}$ (his fig. 8c) suggests that for such clouds a strong ionization-shock (IS) front forms at the irradiated face and it sweeps the neutral gas into the symmetry axis of the cloud, resulting in a cylindrical accretion shock. Such evolution is exactly seen in the numerical results for Low-$\mathcal{U}$ cases (Figs 9a and b). He also estimated the IS-front crossing time for the case of $\psi > 10$,

$$t_{\rm IS} = 2 \times 10^5\,{\rm yr}\,\psi^{-1/4} \left(\frac{M_{\rm cl}}{{\rm M}_\odot}\right)^{1/2}. \tag{59}$$

Table 6 lists $t_{\rm IS}$ for our cloud models (Table 1), together with $t_{\rm end}$, which is the time when the SPH simulation is stopped and corresponds to the actual shock crossing time. $t_{\rm IS}$ is in very good agreement with $t_{\rm end}$ for small $\mathcal{N}_{\rm S}$ or small $\mathcal{U}$ models (L05, L10 and H05). For larger $\mathcal{N}_{\rm S}$ models (H20 and SC00-3D), $t_{\rm IS}$ is poorly matched with $t_{\rm end}$. A large difference between $t_{\rm IS}$ and $t_{\rm end}$ for model SC00-3D is certainly due to that radiation pressure is not taken into account in the Bertoldi formula $t_{\rm IS}$. Thus, $t_{\rm IS}$ is a good estimator for shock crossing time only for smaller $\mathcal{N}_{\rm S}$ and $\mathcal{U}$ cases.

Finally, we comment on the relation between the radiation pressure stripping described in Section 4.3 and the derimming process described in Mathews (1986), in which he studied the structure and stability of a broad emission line cloud nearby a quasar semi-analytically and estimated that the periphery (rim region) of a flatten cloud is preferentially stripped off in a time-scale of $<10t_{\rm sc}$ in a typical environment nearby a quasar because column density-averaged radiative acceleration, $\overline{|\boldsymbol{a}_{\rm rad}|}$, is larger in the periphery than the central part of the cloud. A difference of $\overline{|\boldsymbol{a}_{\rm rad}|}$ also exists in our simulations and this derimming process plays a role in stripping the

gas of the cloud. But, unlike the pure derimming process, a part of the stripped gas comes from the central part of the cloud in the radiation pressure stripping by the effect of the photoevaporation (Fig. 14).

5.3 Star formation

Star formation in AGN-irradiated gas clouds plays important roles in determining the gas supply rate for the following reasons. First, once gas is converted into stars, it is very difficult to supply the gas locked in the stars into an SMBH unless the stars are located at a distance enough close to the SMBH that the tidal disruption mechanism works. Then, what fraction of the gas in the cloud is converted into stars is quite important. Secondly, it could affect self-gravitational stability of the shocked layer via stellar feedback processes such as molecular outflow and stellar radiation. If the stellar feedback is strong enough that part of the shocked layer is brown off into the direction to the AGN, the photoevaporation might be enhanced, changing longevity of the cloud.

Star formation probably occurs in a gas cloud having the same $(\mathcal{U}, \mathcal{N}_S)$ that is investigated in this study, if the initial cloud is sufficiently massive, since density of a dense filament or a shocked layer is quite high. For example, a self-gravitating dense clump is formed in model H20 as already discussed in Section 4.3. The density in the centre of the clump increases as large as $10^{12}\,\mathrm{cm}^{-3}$ (Fig. 15), although we do not include metal line cooling and the gas is artificially heated by the temperature floor. The thermal pressure in the centre of the clump is comparable to that of first core in low-mass star formation simulations (e.g. see ρ–$T_{\rm gas}$ planes in Masunaga, Miyama & Inutsuka 1998; Masunaga & Inutsuka 2000; Tomida et al. 2013). This suggests that the dense clump is eligible to form stars. If we take into account line cooling (e.g. CO, C II, O I) and remove the temperature floor, this clump will fragment into subclumps rapidly and collapse dynamically. Such process is reminiscent of current massive star formation scenario (e.g. Bergin & Tafalla 2007; Zinnecker & Yorke 2007). Unlike model H20, a different type of star formation will be expected in model SC00-3D-static, although the initial cloud properties other than $\mathcal{U}$ are similar each other (see Table 1). In model SC00-3D-static, the shock velocity is higher than model H20. Consequently, the surface density of the post-shock layer increases rapidly compared to model H20, resulting in the self-gravitational fragmentation in the course of the passage of the shock. On the other hand, in model H20, the gas in the post-shock layer falls into the centre of the layer. Thus, there can be two types of star formation depending on the increasing rate of the surface density (Fig. 28).

In connection with the current discussion, Hocuk & Spaans (2010, 2011) recently investigate the influence of X-ray emitted by an AGN on the IMF in a gas cloud by performing three-dimensional hydrodynamic simulations with the X-ray transfer calculation. They assume that the cloud is in a location where most of the optical/UV lights are blocked by many intervening clouds and the X-ray only illuminates the cloud. Their cloud shows similar evolution with that of the lower $\mathcal{U}$ cases in this study. They show that the X-ray heating makes gaseous fragments more massive and the resulting IMF becomes top-heavy compared to the Salpeter IMF. In contrast, the gas clouds that are investigated in this study are irradiated directly by an AGN and in this sense our study is complementary with their studies, although we do not take into account star formation at this time. It is very interesting to examine the star formation properties in a directly irradiated gas clouds and we will address this issue in a future study.

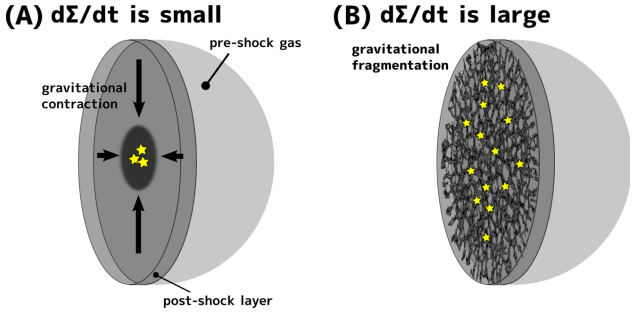

Figure 28. A schematic illustration of two types of star formation in a gas cloud exposed to AGN radiation. If an increasing rate of surface density of a post-shock layer, $\dot{\Sigma}_{\rm gas}$, is small, star formation occurs in a dense gas core at the centre of the post-shock layer, which is formed by global gravitational collapse of the post-shock layer (left). On the other hand, when $\dot{\Sigma}_{\rm gas}$ is sufficiently large, star formation will begin in dense gas filaments in the post-shock layer, which are formed by (two-dimensional) self-gravitational instability of the post-shock layer (right).

5.4 Implications for gas clumps in AGN tori

Here, we discuss possible effects of the AGN radiation on the evolution of gas clumps in AGN tori and mass supply process based on our results. To this end, we first derive the physical properties of the gas clumps in the AGN tori. They can be estimated by considering stabilities against both the tidal shearing by the SMBH and the internal pressure (see appendix in Kawaguchi & Mori 2011). For the sake of completeness, we re-derive a part of the results relevant to our study employing the following assumptions: (1) any external pressures are ignored, and (2) we consider the gravity of the SMBH alone.

From the tidal stability condition, we can determine uniquely the mass density of the clump that located at a distance of r from the SMBH as,

$$\rho_{\rm cl} = 3.54\times10^{-16}\,\mathrm{g\,cm^{-3}}\left(\frac{M_{\rm BH}}{10^7\,\mathrm{M_\odot}}\right)\left(\frac{r}{1\,\mathrm{pc}}\right)^{-3}. \tag{60}$$

The corresponding number density of the hydrogen nuclei is

$$n_{\rm H,cl} = 2.12\times10^{8}\,\mathrm{cm^{-3}}\left(\frac{M_{\rm BH}}{10^7\,\mathrm{M_\odot}}\right)\left(\frac{r}{1\,\mathrm{pc}}\right)^{-3}. \tag{61}$$

The radius of the clump can be determined by the balance between its internal pressure and self-gravity, namely by the Jeans length, as

$$r_{\rm cl} = 0.0182\,\mathrm{pc}\left(\frac{M_{\rm BH}}{10^7\,\mathrm{M_\odot}}\right)^{-0.5}\left(\frac{r}{1\,\mathrm{pc}}\right)^{1.5}\left(\frac{c_{\rm s}}{3\,\mathrm{km\,s^{-1}}}\right), \tag{62}$$

where the normalization of the sound speed is based on the result of Krolik & Lepp (1989), in which they showed that the gas temperature of the clump is mainly determined by the X-ray radiation and is $\approx 10^3$ K, leading to $c_{\rm s}\approx 3\,\mathrm{km\,s^{-1}}$. We can take into account the magnetic pressure by replacing $c_{\rm s}$ by $c_{\rm eff}\equiv(c_{\rm s}^2+c_{\rm A}^2)^{0.5}$, where $c_{\rm A}$ is the Alfvén velocity, although the strength of the magnetic fields inside the clump is currently unknown. The mass and hydrogen column density of the clump are

$$M_{\rm cl} = 120\,\mathrm{M_\odot}\left(\frac{M_{\rm BH}}{10^7\,\mathrm{M_\odot}}\right)^{-0.5}\left(\frac{r}{1\,\mathrm{pc}}\right)^{1.5}\left(\frac{c_{\rm s}}{3\,\mathrm{km\,s^{-1}}}\right)^{3}, \tag{63}$$

$$N_{\rm H,cl} = 1.2\times10^{25}\,\mathrm{cm^{-2}}\left(\frac{M_{\rm BH}}{10^7\,\mathrm{M_\odot}}\right)^{0.5}\left(\frac{r}{1\,\mathrm{pc}}\right)^{-1.5}\left(\frac{c_{\rm s}}{3\,\mathrm{km\,s^{-1}}}\right), \tag{64}$$

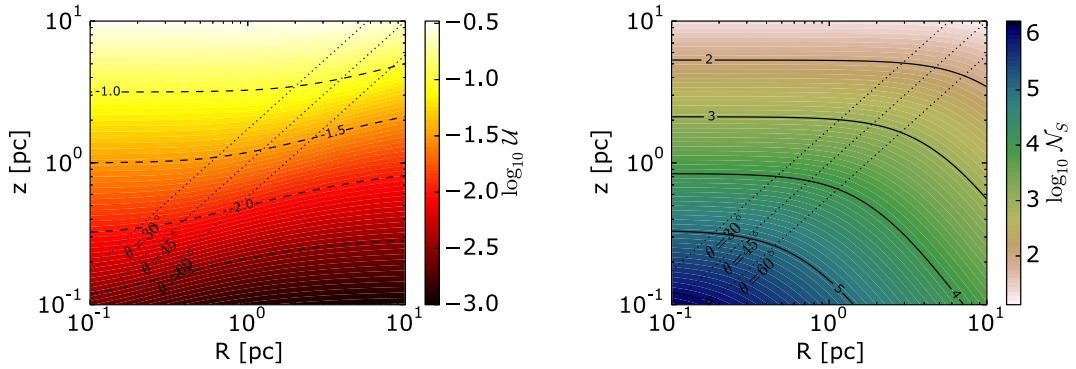

Figure 29. The spacial distributions of $\mathcal{U}$ and $\mathcal{N}_{\rm S}$ for unshielded gas clumps in an AGN torus in the case of $L_{\rm bol} = 10^{45}\,{\rm erg\,s^{-1}}$ and $M_{\rm BH} = 10^7\,{\rm M}_\odot$ (This value of $L_{\rm bol}$ is almost the same as the classical Eddington luminosity). The z-axis is the symmetric axis of the accretion disc and R is the distance from the SMBH along the equatorial plane of the AGN torus. We assume the symmetric axis of the accretion disc is aligned with the symmetric axis of the AGN torus. We also assume that the radiation from the accretion disc is anisotropic (Netzer 1987). For simplicity, we assume that the X-ray, which is isotropically radiated from the accretion disc corona, has the same flux distribution as Netzer (1987). The dotted lines show $z = \tan(\pi/2 - \theta)R$, where θ is the angle measured from the symmetric axis of the accretion disc. In the calculations of $\mathcal{U}$ and $\mathcal{N}_{\rm S}$, we used the equations (61) and (62).

The size, mass and column density of the clump can be smaller values if the clump is confined by the external pressure. Note that the values above are just rough estimates, because we ignore dynamical effects. For example, if the creation and the destruction of the clumps are repeatedly occurred in the AGN torus and the clumps are merely transient objects, we cannot necessarily consider the clumps are stable against the tidal shear.

Using these values and assuming the isotropic AGN radiation, we can obtain the ionization parameter $\mathcal{U}$ and the Strömgren number $\mathcal{N}_{\rm S}$ for the clump that is directly irradiated by the AGN as

$$\mathcal{U} = 1.3\times10^{-2}\left(\frac{L_{\rm bol}}{10^{45}\,{\rm erg\,s^{-1}}}\right)\left(\frac{M_{\rm BH}}{10^7\,{\rm M}_\odot}\right)^{-1}\left(\frac{r}{1\,{\rm pc}}\right), \approx 1.3\times10^{-2}\left(\frac{r}{1\,{\rm pc}}\right)\left(\frac{\lambda_{\rm Edd}}{1}\right), \quad (65)$$

$$\mathcal{N}_{\rm S} = 1.67\times10^{4}\left(\frac{L_{\rm bol}}{10^{45}\,{\rm erg\,s^{-1}}}\right)^{-1}\left(\frac{M_{\rm BH}}{10^7\,{\rm M}_\odot}\right)^{-0.5} \times\left(\frac{r}{1\,{\rm pc}}\right)^{-2.5}\left(\frac{c_{\rm s}}{3\,{\rm km\,s^{-1}}}\right), \quad (66)$$

where we assume the SED shown in equation (18) and $\lambda_{\rm Edd}$ is the Eddington ratio. The Strömgren length of the clumps $l_{\rm s}$ is

$$l_{\rm S} = 0.45\,{\rm au}\left(\frac{L_{\rm bol}}{10^{45}\,{\rm erg\,s^{-1}}}\right)\left(\frac{M_{\rm BH}}{10^7\,{\rm M}_\odot}\right)^{-2}\left(\frac{r}{1\,{\rm pc}}\right)^{4}, \quad (67)$$

where we $\alpha_{\rm B} = 2.59\times10^{-13}\,{\rm cm^3\,s^{-1}}$ (Hui & Gnedin 1997). Thus, the clumps in the AGN torus are extremely optically-thick if the clumps are stable for the tidal shear and the self-gravity. Fig. 29 shows the spacial distributions of $\mathcal{U}$ and $\mathcal{N}_{\rm S}$ of *unshielded* gas clumps in the AGN torus in the case of $L_{\rm bol} = 10^{45}\,{\rm erg\,s^{-1}}$ and $M_{\rm BH} = 10^7\,{\rm M}_\odot$. In the calculations, we assume the SED described in Section 2.2 and take into account the anisotropy of the radiation from the accretion disc. The range of $\mathcal{U}$ that is investigated in this study is $(1.3{-}5.2)\times10^{-2}$, which corresponds to the surface layer of the AGN torus at $r = 1\,{\rm pc}$. Based on our numerical results, the photoevaporation flow may be launched from the surface layer of the AGN torus and then the flow are blown off by the radiation force on the dust. If the AGN torus is sufficiently clumpy, the AGN radiation might drive the photoevaporation of the clumps that lie deep in the torus. Such evaporation flow may contribute the obscuration of the AGN and affect the mass supply rate to the galactic centre as with the simulations by Wada (2012).

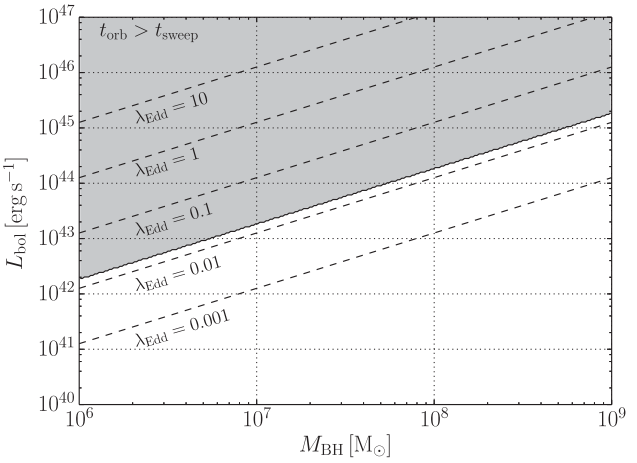

Figure 30. A parameter space of $(M_{\rm BH}, L_{\rm bol})$ where $t_{\rm orb} > t_{\rm sweep}$ at $r = 1\,{\rm pc}$ (the filled region). The dashed lines show bolometric luminosities for $\lambda_{\rm Edd} = 10^{-3}{-}10$.

For the clump located at r, we can estimate the velocity of the shocked layer and the sweep time as

$$v_{\rm sh}^{\rm app} = 9.04\,{\rm km\,s^{-1}}\left(\frac{L_{\rm bol}}{10^{45}\,{\rm erg\,s^{-1}}}\right)^{0.5}\left(\frac{M_{\rm BH}}{10^7\,{\rm M}_\odot}\right)^{-0.5}\left(\frac{r}{1\,{\rm pc}}\right)^{0.5}, \quad (68)$$

$$t_{\rm sweep} = 4016\,{\rm yr}\left(\frac{L_{\rm bol}}{10^{45}\,{\rm erg\,s^{-1}}}\right)^{-0.5}\left(\frac{r}{1\,{\rm pc}}\right)\left(\frac{c_{\rm s}}{3\,{\rm km\,s^{-1}}}\right), \quad (69)$$

where we again assume the AGN radiates isotropically. This razor-thin approximation breaks down if $v_{\rm sh}^{\rm app} < c_{\rm s}$, because the shock does not form. If $c_{\rm s} \approx 3\,{\rm km\,s^{-1}}$ throughout the torus, the critical radius is

$$r_{\rm cr} = 0.1\,{\rm pc}\left(\frac{L_{\rm bol}}{10^{45}\,{\rm erg\,s^{-1}}}\right)^{-1}\left(\frac{M_{\rm BH}}{10^7\,{\rm M}_\odot}\right), \quad (70)$$

which is coincidentally close to the dust sublimation radius for this AGN model that we are looking at. At $r < r_{\rm cr}$, the clumps

are simply pushed by the radiation force if $\mathcal{U}$ is high. For small $\mathcal{U}$ cases, $v_{\rm sh}^{\rm app}$ may not be a good approximation according to the results of Low-$\mathcal{U}$ models and therefore $r_{\rm cr}$ may be different from equation (70). In order to investigate the evolution of clouds with small $\mathcal{U}$ and high $\mathcal{N}_{\rm S}(>10^3)$, Namekata et al. (in preparation) have performed 1D spherically symmetric RHD simulation for the cloud having $\mathcal{U}\approx 1.3\times10^{-2}$ and $\mathcal{N}_{\rm S}\approx 1300$, and have found that the shock velocity averaged over the cloud evolution is roughly close to $v_{\rm sh}^{\rm app}$ because the photoevaporation flow is finally confined by the radiation pressure and the rocket effect becomes inefficient. Therefore, $t_{\rm sweep}$ is a good approximation for the cloud destruction time if $\mathcal{N}_{\rm S}$ is extremely high. For this reason, we expect that the clumps are not destroyed at $r < r_{\rm cr}$ if $\mathcal{U}$ is small. It is useful to compare $t_{\rm sweep}$ with other various time-scales. The orbital time and the sound crossing time are

$$t_{\rm orb} = 2.98\times10^4\ {\rm yr}\left(\frac{M_{\rm BH}}{10^7\ {\rm M}_\odot}\right)^{-0.5}\left(\frac{r}{1\ {\rm pc}}\right)^{1.5}, \tag{71}$$

$$t_{\rm sc}=\frac{2r_{\rm cl}}{c_{\rm s}^{\rm irr}}=1.27\times10^3\ {\rm yr}\left(\frac{M_{\rm BH}}{10^7\ {\rm M}_\odot}\right)^{-0.5}\left(\frac{r}{1\ {\rm pc}}\right)^{1.5}\left(\frac{c_{\rm s}}{3\ {\rm km\ s^{-1}}}\right), \tag{72}$$

where $c_{\rm s}^{\rm irr}$ is the sound speed of fully ionized pure hydrogen gas of $T_{\rm gas}=30\,000$ K. Thus, both $t_{\rm sweep}$ and $t_{\rm sc}$ are much smaller than $t_{\rm orb}$ and the gas clumps should be compressed in a short time if they are directly irradiated. This may suggest that the AGN tori with $\lambda_{\rm Edd}\approx 1$ can be short-lived compared to the orbital time-scale. Because $t_{\rm sweep}\propto\mathcal{U}^{-0.5}$ (see equations 16 and 17), $t_{\rm sweep}$ remains smaller than $t_{\rm orb}$ even for the AGN with $\lambda_{\rm Edd}\approx 0.1$, which is a typical Eddington ratio (e.g. Lusso et al. 2012). Fig. 30 shows combinations of $(M_{\rm BH}, L_{\rm bol})$ where $t_{\rm orb} > t_{\rm sweep}$ at $r = 1$ pc.

On the other hand, if the actual AGN torus maintains its clumpy structure for long period, there are the following possibilities:

(I) The most of the clumps in the torus are exposed to sufficiently weak radiation field (small $\mathcal{U}$) and therefore the shock does not occur in the clumps. The causes to reduce $\mathcal{U}$ include (i) the anisotropy of the AGN radiation, (ii) the higher averaged density of the clumps than the critical density with respect to the tidal shear and (iii) extinction by the interclump medium. Another interesting possibility is that a dusty wind that launched from the inner edge of the torus shields the main body of the torus as if the hitch-hiking gas does in the accretion disc wind model (Murray et al. 1995). This possibility seems to be compatible with the recent numerical study (Wada 2012) and observational studies (Czerny & Hryniewicz 2011; Hönig et al. 2012, 2013; Tristram et al. 2012).

(II) The clumps are destroyed by the shock in short time-scales, but, the creation of the clumps are continuously occurred to offset the destruction of the clumps by some mechanism. The stellar feedback-driven turbulence might be a candidate mechanism.

Obviously, further studies are needed to examine these possibilities.

6 SUMMARY

In this paper, we have performed 3D RHD simulations of the gas clouds exposed to the AGN radiation varying the ionization parameter $\mathcal{U}$ and the Strömgren number $\mathcal{N}_{\rm S}$ to investigate combined effects of the photoevaporation and the radiation pressure force on the evolution of the cloud. We have found that the evolution of the clouds can be classified into two cases depending on $\mathcal{U}$.

(i) In Low-$\mathcal{U}$ case ($\mathcal{U}\approx 1.3\times10^{-2}$), the photoevaporation determines the evolution of the cloud independent of $\mathcal{N}_{\rm S}$. The photoevaporation flow is launched from the irradiated face. The flow is almost spherical and its velocity is $\approx$100 km s^{-1}. The mass-loss is realized as this photoevaporation flow and the gas clouds are compressed by the counteraction of the flow. The compression is completed in a time-scale comparable with $t_{\rm sc}$.

(ii) In High-$\mathcal{U}$ case ($\mathcal{U}\gtrsim 5.2\times10^{-2}$), the radiation pressure turn the photoevaporation flow that launched from the outskirt of the irradiated face into the direction opposite to the AGN, outwards from the galactic centre, while it confines the flow that launched from the central part of the irradiated face. Because of this, fractional mass-loss rate is smaller than Low-$\mathcal{U}$ case, at least until $t\lesssim t_{\rm sc}$. The shocked layer that is formed by both the radiation pressure and the counteraction of the photoevaporation flow sweep the main body of the cloud in a time-scale of $t_{\rm sweep}$.

In both cases of $\mathcal{U}$, mass fraction of dense gas is larger for larger $\mathcal{N}_{\rm S}$. Star formation will occurs in the compressed part of the cloud, if the cloud has initially sufficient mass to form stars. We have analysed a self-gravitating dense clump formed at the centre of the shocked layer in model H20 and have found that the clump has physical properties similar to those in high-mass star-forming region in the Galaxy. We speculate high-mass star formation occurs in this clump.

We also have performed simulations of more higher-$\mathcal{U}$ case ($\mathcal{U}\approx 0.17$; models SC00-3D-static and SC00-3D-ff) in order to investigate the evolution of the cloud under a more stronger radiation field as well as the dependence on the initial condition. In model SC00-3D-static, the cloud is simply destroyed by the passage of the shock driven by the intense radiation pressure and no photoevaporation occurs. On the other hand, in model SC00-3D-ff, which models a cloud that infalls in an external gravitational potential of an SMBH and an NSC, the propagation speed of the shock is decreased by the effects of the tidal force. As a result, the pre-shock gas survives longer than that in SC00-3D-static. However, it is expected that the cloud collapses by the transverse component of the total gravity before it reaches the galactic centre. In order to elucidate the gas supply process to the galactic centre by a low-angular-momentum cloud such as the cloud in SC00-3D-ff, we have to investigate how the star formation proceeds in the cloud.

Based on the numerical results, we have discussed the properties of the gas clumps in the AGN torus with high Eddington ratio in Section 5.4. A simple estimate suggests that the clumps are destroyed in time-scales that are shorter than the orbital period. For the clumpy structure to be maintained over long period, the incident radiation field needs to be sufficiently weaken $\mathcal{U}$ for most of the clumps, or, some mechanism that creates the clumps continuously is needed.

ACKNOWLEDGEMENTS

We thank Ataru Tanikawa for his advice about the implementation of the Phantom-GRAPE library, and Toshihiro Kawaguchi for helpful discussions about properties of AGN tori. We would also like to thank Nitadori Keigo for publication of the Phantom-GRAPE library on the web. We also thank the anonymous referee for his/her helpful suggestions that improved our manuscript. Finally, we thank Akitoshi Oshima who greatly improved the computing environments of the medium-scale PC clusters installed at Center for Computational Astrophysics (CfCA) of National Astronomical Observatory of Japan (NAOJ) to meet our difficult requests,

and the developers of the software packages DISLIN, MATPLOTLIB and ASYMPTOTE, with which we visualized our numerical results. The numerical simulations were carried out on Cray XT4, Cray XC30 and the medium-scale PC clusters at CfCA of NAOJ, and FIRST and T2K Tsukuba at Center for Computational Sciences (CCS) in University of Tsukuba. This work was supported by the Ministry of Education, Culture, Sports, Science and Technology (MEXT) Grant-in-Aid for Scientific Research (S)20224002 (MU), MEXT Grant-in-Aid for Young Scientists (B)25800100 (DN) and by MEXT SPIRE Field 5 and JICFuS.

REFERENCES

Abel T., Anninos P., Zhang Y., Norman M. L., 1997, New Astron., 2, 181
Anderson R. J., 1999, SIAM J. Comput., 28, 1923
Antonucci R., 1993, ARA&A, 31, 473
Athanassoula E., 1992, MNRAS, 259, 345
Balsara D. S., 1995, J. Comput. Phys., 121, 357
Barkana R., Loeb A., 1999, ApJ, 523, 54
Barnes J. E., 1990, J. Comput. Phys., 87, 161
Barnes J. E., Hernquist L. E., 1991, ApJ, 370, L65
Barnes J. E., Hut P., 1986, Nature, 324, 446
Benson A., Bower R., Frenk C., Lacey C., Baugh C., Cole S., 2003, ApJ, 599, 38
Bergin E. A., Tafalla M., 2007, ARA&A, 45, 339
Bertoldi F., 1989, ApJ, 346, 735
Bertoldi F., McKee C. F., 1990, ApJ, 354, 529
Blumenthal G. R., Mathews W. G., 1979, ApJ, 233, 479
Bonnell I., Rice W., 2008, Science, 321, 1060
Burke J. R., Hollenbach D., 1983, ApJ, 265, 223
Cattaneo A., Blaizot J., Devriendt J., Guiderdoni B., 2005, MNRAS, 364, 407
Cazaux S., Spaans M., 2004, ApJ, 611, 40
Cazaux S., Tielens A., 2004, ApJ, 604, 222
Cazaux S., Tielens A., 2010, ApJ, 715, 698
Cen R., 1992, ApJS, 78, 341
Croom S. M., Boyle B., Loaring N., Miller L., Outram P., Shanks T., Smith R., 2002, MNRAS, 335, 459
Czerny B., Hryniewicz K., 2011, A&A, 525, L8
Dietrich M., Hamann F., 2002, ApJ, 581, 912
Draine B., Bertoldi F., 1996, ApJ, 468, 269
Draine B., Lee H. M., 1984, ApJ, 285, 89
Draine B., Salpeter E., 1979, ApJ, 231, 77
Dullemond C., van Bemmel I., 2005, A&A, 436, 47
Ferland G. et al., 2013, Rev. Mex. Astron. Astrofís., 49, 137
Fukugita M., Kawasaki M., 1994, MNRAS, 269, 563
Fukunaga M., 1983, PASJ, 35, 173
Fukunaga M., 1984a, PASJ, 36, 417
Fukunaga M., 1984b, PASJ, 36, 433
Galli D., Palla F., 1998, A&A, 335, 403
Gingold R., Monaghan J., 1977, MNRAS, 181, 375
Gorti U., Hollenbach D., 2002, ApJ, 573, 215
Hasegawa K., Umemura M., 2010, MNRAS, 407, 2632
Hasegawa K., Umemura M., Susa H., 2009, MNRAS, 395, 1280
Hernquist L., 1989, Nature, 340, 687
Hernquist L., Katz N., 1989, ApJS, 70, 419
Hirashita H., Ferrara A., 2002, MNRAS, 337, 921
Hobbs A., Nayakshin S., 2009, MNRAS, 394, 191
Hocuk S., Spaans M., 2010, A&A, 522, A24
Hocuk S., Spaans M., 2011, A&A, 536, A41
Hollenbach D., McKee C. F., 1979, ApJS, 41, 555
Hopkins P. F., 2013, MNRAS, 428, 2840
Hui L., Gnedin N. Y., 1997, MNRAS, 292, 27
Hönig S., Beckert T., Ohnaka K., Weigelt G., 2006, A&A, 452, 459
Hönig S., Kishimoto M., Antonucci R., Marconi A., Prieto M., Tristram K., Weigelt G., 2012, ApJ, 755, 149
Hönig S. et al., 2013, ApJ, 771, 87
Iliev I. T., Shapiro P. R., Raga A. C., 2005, MNRAS, 361, 405
Iliev I. T. et al., 2006, MNRAS, 371, 1057
Johnstone D., Hollenbach D., Bally J., 1998, ApJ, 499, 758
Kahn F., 1969, Physica, 41, 172
Kawaguchi T., Mori M., 2011, ApJ, 737, 105
Kawakatu N., Wada K., 2008, ApJ, 681, 73
Kawakatu N., Wada K., 2009, ApJ, 706, 676
Kellogg E., Baldwin J., Koch D., 1975, ApJ, 199, 299
Kendall P., Magorrian J., Pringle J., 2003, MNRAS, 346, 1078
Kim W.-T., Ostriker E. C., Stone J. M., 2002, ApJ, 581, 1080
Krolik J. H., Begelman M. C., 1988, ApJ, 329, 702
Krolik J. H., Lepp S., 1989, ApJ, 347, 179
Krolik J. H., McKee C. F., Tarter C. B., 1981, ApJ, 249, 422
Lamers H. J., Cassinelli J. P., 1999, Introduction to Stellar Winds. Cambridge Univ. Press, Cambridge
Landau L., Lifshitz E., 1980, Statistical Physics. Butterworth-Heinemann, Oxford
Laor A., Draine B. T., 1993, ApJ, 402, 441
Lefloch B., Lazareff B., 1994, A&A, 289, 559
Lucy L., 1977, AJ, 82, 1013
Lusso E. et al., 2012, MNRAS, 425, 623
McKee C. F., Tarter C. B., 1975, ApJ, 202, 306
Makino J., 1991, PASJ, 43, 621
Makino J., 2004, PASJ, 56, 521
Martin P., Keogh W., Mandy M., 1998, ApJ, 499, 793
Masunaga H., Inutsuka S., 2000, ApJ, 531, 350
Masunaga H., Miyama S. M., Inutsuka S., 1998, ApJ, 495, 346
Mathews W. G., 1974, ApJ, 189, 23
Mathews W. G., 1976, ApJ, 207, 351
Mathews W. G., 1982, ApJ, 252, 39
Mathews W. G., 1986, ApJ, 305, 187
Mathews W. G., Blumenthal G. R., 1977, ApJ, 214, 10
Mihos J. C., Hernquist L., 1996, ApJ, 464, 641
Milosavljević M., 2004, ApJ, 605, L13
Monaghan J., 1997, J. Comput. Phys., 136, 298
Monaghan J., Lattanzio J., 1985, A&A, 149, 135
Morris J., Monaghan J., 1997, J. Comput. Phys., 136, 41
Motoyama K., Umemoto T., Shang H., 2007, A&A, 467, 657
Mott D. R., Oran E. S., van Leer B., 2000, J. Comput. Phys., 164, 407
Murray N., Chiang J., Grossman S., Voit G., 1995, ApJ, 451, 498
Namekata D., Habe A., 2011, ApJ, 731, 57
Nayakshin S., Cuadra J., Springel V., 2007, MNRAS, 379, 21
Nenkova M., Ivezić Ž., Elitzur M., 2002, ApJ, 570, L9
Nenkova M., Sirocky M. M., Ivezić Ž., Elitzur M., 2008, ApJ, 685, 147
Nenkova M., Sirocky M. M., Nikutta R., Ivezić Ž., Elitzuer M., 2008, ApJ, 685, 160
Netzer H., 1987, MNRAS, 225, 55
Nitadori K., Makino J., Hut P., 2006, New Astron., 12, 169
Okamoto T., Yoshikawa K., Umemura M., 2012, MNRAS, 419, 2855
Oort J. H., Spitzer L., Jr, 1955, ApJ, 121, 6
Osterbrock D. E., Ferland G. J., 2006, Astrophysics of Gaseous Nebulae and Active Galactic Nuclei, 2nd edn. University Science Books, Mill Valley, CA
Palla F., Salpeter E., Stahler S. W., 1983, ApJ, 271, 632
Pier E. A., Voit G. M., 1995, ApJ, 450, 628
Proga D., Jiang Y.-F., Davis S. W., Stone J. M., Smith D., 2014, ApJ, 780, 51
Richling S., Yorke H. W., 2000, ApJ, 539, 258
Roth N., Kasen D., Hopkins P. F., Quataert E., 2012, ApJ, 759, 36
Saitoh T. R., Makino J., 2013, ApJ, 768, 44
Saitoh T. R., Wada K., 2004, ApJ, 615, L93
Saitoh T. R., Koda J., Okamoto T., Wada K., Habe A., 2006, ApJ, 640, 22
Sanders R., 1998, MNRAS, 294, 35
Schartmann M., Meisenheimer K., Camenzind M., Wolf S., Henning T., 2005, A&A, 437, 861
Schartmann M., Meisenheimer K., Klahr H., Camenzind M., Wolf S., Henning T., 2009, MNRAS, 393, 759

Schartmann M., Burkert A., Krause M., Camenzind M., Meisenheimer K., Davies R., 2010, MNRAS, 403, 1801
Schartmann M., Krause M., Burkert A., 2011, MNRAS, 415, 741
Shapiro P. R., Iliev I. T., Raga A. C., 2004, MNRAS, 348, 753
Smith J., Young S., Robinson A., Corbett E., Giannuzzo M., Axon D., Hough J., 2002, MNRAS, 335, 773
Smith J. D., Robinson A., Alexander D., Young S., Axon D., Corbett E. A., 2004, MNRAS, 350, 140
Smith J., Robinson A., Young S., Axon D., Corbett E. A., 2005, MNRAS, 359, 846
Springel V., 2005, MNRAS, 364, 1105
Störzer H., Hollenbach D., 1999, ApJ, 515, 669
Susa H., 2006, PASJ, 58, 445
Susa H., 2007, ApJ, 659, 908
Susa H., Umemura M., 2004a, ApJ, 600, 1
Susa H., Umemura M., 2004b, ApJ, 610, L5
Susa H., Umemura M., 2006, ApJ, 645, L93
Susa H., Umemura M., Hasegawa K., 2009, ApJ, 702, 480
Tajiri Y., Umemura M., 1998, ApJ, 502, 59
Taniguchi Y., 1999, ApJ, 524, 65
Tanikawa A., Yoshikawa K., Okamoto T., Nitadori K., 2012, New Astron., 17, 82
Tanikawa A., Yoshikawa K., Nitadori K., Okamoto T., 2013, New Astron., 19, 74
Telfer R. C., Zheng W., Kriss G. A., Davidsen A. F., 2002, ApJ, 565, 773
Thomas P., Couchman H., 1992, MNRAS, 257, 11
Tomida K., Tomisaka K., Matsumoto T., Hori Y., Okuzumi S., Machida M. N., Saigo K., 2013, ApJ, 763, 6
Tristram K., Schartmann M., Burtscher L., Meisenheimer K., Jaffe W., Kishimoto M., Hönig S., Weigelt G., 2012, J. Phys.:Conf. Ser., 372, id.012035
Urry C. M., Padovani P., 1995, PASP, 107, 804
Wada K., 2002, ApJ, 566, L21
Wada K., 2012, ApJ, 758, 66
Wada K., Papadopoulos P. P., Spaans M., 2009, ApJ, 702, 63
Wardle M., Yusef-Zadeh F., 2008, ApJ, 683, L37
Weymann R., 1976, ApJ, 208, 286
Whalen D., Norman M. L., 2006, ApJS, 162, 281
Williams R. E., 1972, ApJ, 178, 105
Wolcott-Green J., Haiman Z., Bryan G., 2011, MNRAS, 418, 838
Yoshida N., Omukai K., Hernquist L., Abel T., 2006, ApJ, 652, 6
Young S., Hough J., Axon D., Bailey J., Ward M., 1995, MNRAS, 272, 513
Young S., Hough J., Efstathiou A., Wills B., Bailey J., Ward M., Axon D., 1996, MNRAS, 281, 1206
Zel'dovich Y. B., Syunyaev R., 1969, Sov. Phys. – JETP, 29, 1118
Zinnecker H., Yorke H. W., 2007, ARA&A, 45, 481

APPENDIX A: DOPPLER-SHIFT AND DUST–GAS COUPLING

In this study, we ignored the effects of the Doppler shift and assumed that dust is tightly coupled with gas. Here, we discuss these assumptions briefly. The inclusion of the Doppler shift does not change our results largely as far as the motion of photoevaporation flow is mainly determined by the absorption of continuum photons by neutral hydrogen and dust grains, because the shape of incident spectrum keeps almost unchanged even if we take into account the Doppler shift (the wavelength shift is at most $\approx$1 Å at $\lambda = 10^3$ Å for $v = 300\,\mathrm{km\,s^{-1}}$). However, in a situation that the motion of photoevaporation flow is controlled by the absorption of line photons, the Doppler shift must play important roles to determine the velocity structure of the flow, as in the case of accretion disc wind (e.g. Murray et al. 1995). Such situation is realized if dust is completely destroyed by thermal sputtering process and metal opacities become important. The dust destruction by the thermal sputtering was studied by Draine & Salpeter (1979). Based on their results, the dust destruction time-scale $\tau_{\rm gr}^{\rm dest}$ is given by

$$\tau_{\rm gr}^{\rm dest} \sim \begin{cases} 100\,\mathrm{Myr}\left(\frac{T_{\rm gas}}{56\,000\,\mathrm{K}}\right)^{-3} & \\ \quad \times \left(\frac{n_{\rm H}}{1\,\mathrm{cm^{-3}}}\right)^{-1}\left(\frac{a_{\rm gr}}{0.01\,\mu\mathrm{m}}\right) & T_{\rm gas} \leq 10^6\,\mathrm{K} \\ 20\,\mathrm{kyr}\left(\frac{n_{\rm H}}{1\,\mathrm{cm^{-3}}}\right)^{-1}\left(\frac{a_{\rm gr}}{0.01\,\mu\mathrm{m}}\right) & T_{\rm gas} > 10^6\,\mathrm{K}. \end{cases} \quad \text{(A1)}$$

The typical gas temperature and number density of the photoevaporation flow in our simulations are $T_{\rm gas} = 30\,000$ K and $n_{\rm H} = 10^2$–$10^3\,\mathrm{cm^{-3}}$. For $a_{\rm gr} = 0.05\,\mu$m, $\tau_{\rm gr}^{\rm dest} \gtrsim 3.25$ Myr. Therefore, the thermal sputtering is not important for our simulations. But, the thermal sputtering can be effective in a denser photoevaporation flow, which may occur in the inner part of an AGN torus where average gaseous density is expected to be high.

APPENDIX B: TREE-ACCELERATED LONG CHARACTERISTIC METHOD

In this section, we explain tree-accelerated long characteristic method in detail. First of all, we introduce some terminology. For a given radiation source s and a target particle i to which we want to evaluate the column densities, we define *upstream particles* as particles that obscure the target particle at least partially. Conversely, the particles that are obscured by a target particle at least partially for a given radiation source are called *downstream particles*.

B1 Column density calculation

Here, we explain calculation method of obscuring column density due to particle j to particle i. As shown in Fig. B1, if the line segment $\overline{i-s}$ that connects between particle i and radiation source s passes through the SPH kernel of particle j, obscuring column density due to particle j, $\delta N_{\rm col}^{(k)}(j \to i)$, can be computed by

$$\delta N_{\rm col}^{(k)}(j \to i) = 2\int_0^{\sqrt{h_j^2 - d^2}} Y_j^{(k)} m_j W(r, h_j)\mathrm{d}z, \quad \text{(B1)}$$

where k denotes species, $Y_j^{(k)}$ is the mass abundance of species k of particle j, d is the distance between particle j and the line $\overline{i-s}$, W

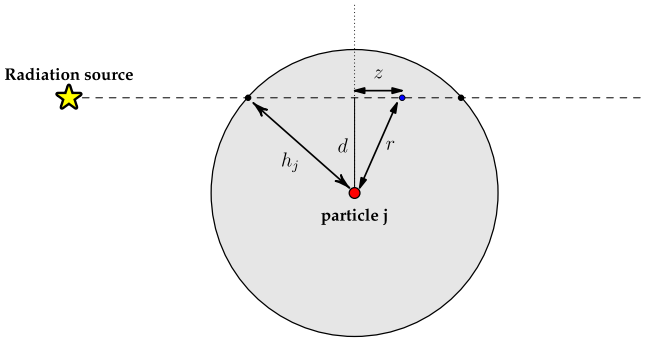

Figure B1. A schematic illustration of the calculation of the column density. The dashed line shows the line that connects between radiation source s and particle i to which we want to evaluate the column density. The red point represents one of the upstream particles of particle i. Here, we call it particle j. It is located at a distance d from the line $\overline{i-s}$ and its smoothing length is h_j. Particle i is located outside the figure.

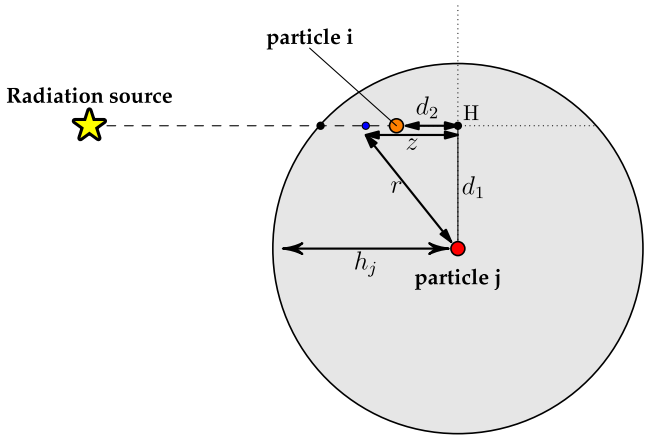

Figure B2. The same as Fig. B1 but for the case that particle i is located within the SPH kernel of particle j and is nearer to the radiation source s than the point H. d_1 is the same as d in Fig. B1, while d_2 is the distance between the point H and particle i.

is the SPH kernel function. Using normalized variables $\tilde{d} = d/h_j$, $\tilde{r} = r/h_j$ and $\tilde{z} = z/h_j$ and the relation $W(r, h) = h^{-3}w(\tilde{r})$, we can rewrite the equation above into

$$\delta N_{\rm col}^{(k)}(j \rightarrow i) = Y_j^{(k)} m_j h_j^{-2} F(\tilde{d}), \tag{B2}$$

where

$$F(\tilde{d}) = 2\int_0^{\sqrt{1-\tilde{d}^2}} w(\tilde{r}){\rm d}\tilde{z}. \tag{B3}$$

Thus, we calculate $\delta N_{\rm col}^{(k)}(j \rightarrow i)$ easily using the physical quantities of particle j and a look-up table for $F(\tilde{d})$.

In the cases that either of particle i or radiation source s is located within the SPH kernel of particle j, $\delta N_{\rm col}^{(k)}(j \rightarrow i)$ can be calculated using a two-dimensional table. As an example, we consider the situation shown in Fig. B2, in which particle i is in the SPH kernel of particle j and its position is nearer to the radiation source s than the point H. In this case, $\delta N_{\rm col}^{(k)}(j \rightarrow i)$ is computed by

$$\delta N_{\rm col}^{(k)}(j \rightarrow i) = \int_{d_2}^{\sqrt{h_j^2-d_1^2}} Y_j^{(k)} m_j W(r, h_j){\rm d}z, \tag{B4}$$

$$= Y_j^{(k)} m_j h_j^{-2} G(\tilde{d}_1, \tilde{d}_2), \tag{B5}$$

where

$$G(\tilde{d}_1, \tilde{d}_2) = \int_{\tilde{d}_2}^{\sqrt{1-\tilde{d}_1^2}} w(\tilde{r}){\rm d}\tilde{z}. \tag{B6}$$

When particle i is farther to the radiation source s than the point H, $\delta N_{\rm col}^{(k)}(j \rightarrow i)$ is computed using the same two-dimensional table but by replacing $G(\tilde{d}_1, \tilde{d}_2)$ in the equation (B5) by $2G(\tilde{d}_1, 0) - G(\tilde{d}_1, \tilde{d}_2)$. The same method is applicable to the cases that radiation source s is located within the SPH kernel of particle j. The situations not discussed so far are the cases that *both* the radiation source s and particle i are contained in the SPH kernel of particle j (there are three cases depending on the relative positions of s and i to the point H). In these cases, we calculate $\delta N_{\rm col}^{(k)}(j \rightarrow i)$ by using a linear combination of $G(\tilde{d}_1, 0)$, $G(\tilde{d}_1, \tilde{d}_2^s)$, and $G(\tilde{d}_1, \tilde{d}_2^i)$, where $\tilde{d}_2^s$ and $\tilde{d}_2^i$ are normalized distances between the point H and s/i, respectively.

B2 Acceleration of column density calculation

In the original long characteristic method, we seek all of the upstream particles for a target particle i and compute $N_{{\rm col},i}^{(k)} = \sum_j \delta N_{\rm col}^{(k)}(j \rightarrow i)$. This calculation is repeated for all the particles. However, such calculation is numerically expensive and a simulation does not end within a realistic time. Therefore, we need to reduce the computational cost keeping its accuracy reasonable. To achieve it, we use a tree structure in this paper.

Let us consider a small number ($< n_{i_G}^{\rm crit}$) of the particles that are close each other. We call these particles the target particles or simply group i_G and evaluate the column densities at their locations for a given radiation source s which is placed at $\boldsymbol{x}_{\rm s}$. Because each of the target particles has almost the same upstream particles, we calculate column densities for particle $i \in i_G$ using the same list of the upstream particles. This approach is the same as the group interaction list technique used in the N-body calculation (Barnes 1990; Makino 1991) and i_G is chosen from the group nodes. The list of the upstream particles is constructed by making the node list according to the procedure described in Algorithm 2,[9] and then expanding it.

[9] Here, we explain Algorithm 2 in more detail. This procedure is a recursive one and makes a list of tree nodes that intersects either of the line segments that connect the radiation source s and particle $i \in i_G$. For a given node id, we first investigate the number of the particle contained in this node, which is represented by $\mathcal{T}.n_{\rm ptcl}(id)$ in the figure ($\mathcal{T}$ is a data structure for the tree and $n_{\rm ptcl}()$ is a member array of $\mathcal{T}$). If $\mathcal{T}.n_{\rm ptcl}(id) = 1$, node id is added to the list unconditionally. If $\mathcal{T}.n_{\rm ptcl}(id) > 1$, several tests are performed to see if node id has upstream particles of the particles contained in node i_G:

(1) Disjoint test. This test investigates whether node id and group node i_G are disjoint each other or not and the result is stored into $f_{\rm disjoint}$,

(2) Enclose test. This test examines whether node id contains the radiation source s or not and the result is stored into $f_{\rm enclose}$,

(3) Intersection test. If $f_{\rm disjoint}$ is `True` and $f_{\rm enclose}$ is `False`, an additional test is performed, in which we check whether some particles in node id can be upstream particles of the particles $i \in i_G$. A straightforward way to examine this possibility is to check whether the SPH kernel of particle j in node id intersects the line segment $\overline{s-i}$ for all combinations of (i,j). However, it is inefficient. Instead, we use the geometric information of the nodes. More specifically, as shown in Fig. B3, we investigate the positional relations between the vertices and the geometric centre of node id and the line segments that connect the radiation source s and the vertices and the geometric centre of node i_G.

We decide that node id is an upstream node of node i_G if $0 \le t_{ij,\,\rm H} \le 1$ and $d_{ij} \le d_{\rm crit}$ are satisfied by at least one combination of (i, j). $t_{ij,\,\rm H}$ and d_{ij} are defined as

$$t_{ij,{\rm H}} = \frac{\boldsymbol{x}_{is} \cdot \boldsymbol{x}_{js}}{|\boldsymbol{x}_{is}|^2}, \tag{B8}$$

$$d_{ij} = |t_{\rm H}\boldsymbol{x}_{is} - \boldsymbol{x}_{js}|, \tag{B9}$$

where s indicates the radiation source, i and j take A_{19} and B_{19}, respectively (see Fig. B3). $t_{ij,\,\rm H}$ represents the position of the foot of the perpendicular of the point j on to the line that passes through s and i. $0 \le t_{ij,\,\rm H} \le 1$ means that the foot is laid in the line segment $\overline{s-i}$. d_{ij} is the distance between the point j and $\overline{s-i}$. $d_{\rm crit} \equiv \max(l_{i_G}, l_{j_G})$ and l_α is defined as

$$l_\alpha = \sqrt{1.05(l_{x,\alpha}^2 + l_{y,\alpha}^2 + l_{z,\alpha}^2)}. \tag{B10}$$

If $f_{\rm intersect}$ = `False`, we return the process to the parent node. If (i) either of $f_{\rm disjoint}$ = `False` or $f_{\rm enclose}$ = `True` is satisfied, and (ii) $\mathcal{T}.n_{\rm ptcl}(id) < n_{j_G}^{\rm crit}$, node id is added to the list. Otherwise, we descend the tree further.

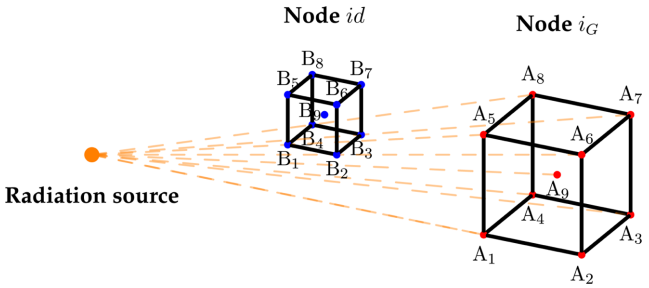

Figure B3. A schematic illustration of the intersection test. The two cubes represent tree nodes and node *id* is the node that exposed to the intersection test. For brevity, we do not plot the SPH particles contained in the nodes. The red and blue points indicate the vertices of the nodes (A_1-A_8, B_1-B_8) and the geometric centres of the nodes (A_9, B_9). The orange dashed line segments connect the radiation source and the points $\{A_i\}$.

In order to speed up the calculation further, we approximate obscuring column densities due to an upstream particle j to all the particles $i \in i_G$ by a common value of $\delta N_{\rm col}^{(k)}(j \to i_G)$, if the upstream particle j satisfies the following two conditions:

(i) the SPH kernel of particle j does not overlap group node i_G,
(ii) particle j satisfies the inequality,

$$\theta \equiv \frac{\max(l_x, l_y, l_z)}{r} < \theta_{\rm RT}, \tag{B7}$$

where l_i is the physical size of group node i_G in each dimension, r is the distance between the geometric centre of group i_G, $\boldsymbol{x}_{{\rm cen},i_G}$ and $\boldsymbol{x}_j$, and $\theta_{\rm RT}$ is a tolerance parameter which determines the accuracy. In this study, we use $\theta_{\rm RT} = 1$ for all the simulations.

$\delta N_{\rm col}^{(k)}(j \to i_G)$ is calculated using $\boldsymbol{x}_j$ and $\boldsymbol{x}_{{\rm cen},i_G}$ according to the method described in Appendix B1. Otherwise, we compute $\delta N_{\rm col}^{(k)}(j \to i)$ individually for all the particle $i \in i_G$.

Thus, this method can reduce the calculation cost by a factor of n_{i_G} in the best case. In our computational environments, optimal choice were $n_{i_G}^{\rm crit} = n_{j_G}^{\rm crit} = 32$. Further speed-up can be possible if we replace a group of *upstream* particles by a virtual particle or cell based on some criterion. This will reduce the cost by a factor of n_{j_G}. But, a care must be taken because a density structure of upstream region is smoothed out.

Algorithm 2: MAKENODELIST

```
input  : x_min,iG, x_max,iG, x_s, T, id
output: a list of nodes
if T.n_ptcl(id) > 1 then
    f_disjoint ← Disjoint test ;
    f_enclose ← Enclose test ;
    if f_disjoint = True and f_enclose = False then
        f_intersect ← Intersection test ;
        if f_intersect = False then
            Return ;
        end
    end
    if T.n_ptcl(id) < n_jG^crit then
        Append id to the list ;
    else
        foreach a child node, cid, of the node id do
            MakeNodelist(x_min,iG, x_max,iG, x_s, T, cid)
            ;
        end
    end
else if T.n_ptcl(id) = 1 then
    Append id to the list ;
end
```

B3 Tests

In order to check the accuracy of our method described in the previous sections, we perform the same tests as Test 1 and Test 2 in Iliev et al. (2006), which are the calculations of an expansion of an H II region in an uniform static medium. We use the same physical parameters and settings as Iliev et al. (2006) except for the size of the computational box and the numerical resolution. Here, a 13.2 kpc cubic computational box is assumed. We place an ionizing radiation source at the centre of the box. The uniform medium is realized by a glass-like distribution of 128^3 SPH particles. Therefore, the numerical resolution is two times lower than that used in Iliev et al. (2006).

The time evolution of H I fraction, $X_{\rm H_I}$, in Test 1 is shown in Fig. B4. The result at $t = 500$ Myr is in good agreement with those shown in fig. 6 of Iliev et al. (2006). In order to see the accuracy more quantitatively, we show in Fig. B5 the time evolution of the

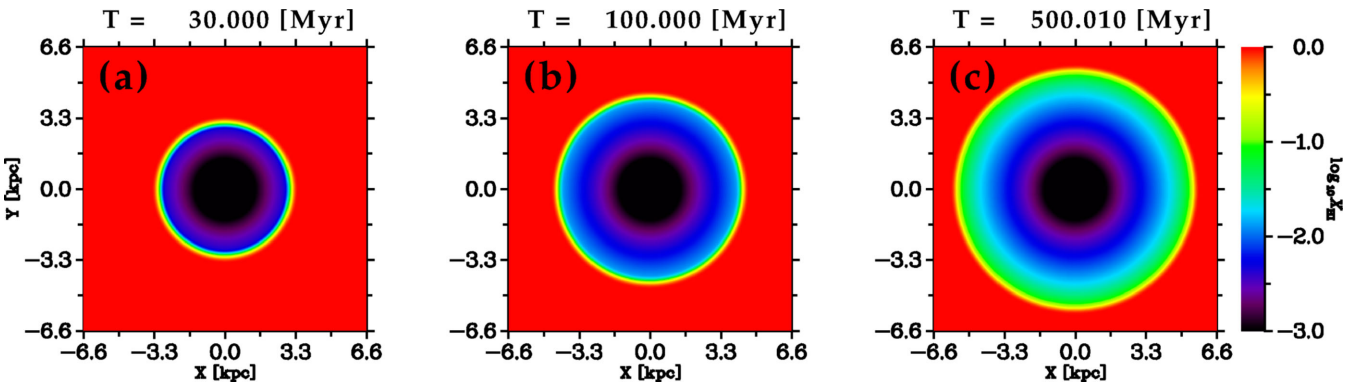

Figure B4. H I fraction at different times in Test 1 of Iliev et al. (2006). All the snapshots are slices at $z = 0$.

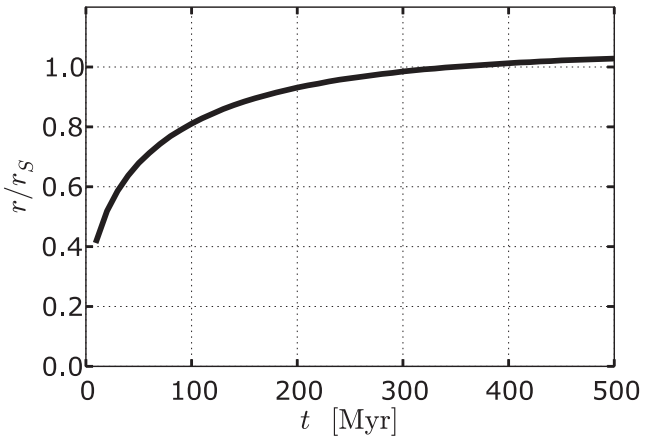

Figure B5. The propagation of the ionization front in Test 1 of Iliev et al. (2006). The radius of the ionization front is normalized by the initial Strömgren radius r_S, which is 5.4 kpc in this case.

radius of the ionization front (IF), which is defined as the radius at which $X_{\rm H\,I} = 0.5$. The IF saturates at a value of $r \approx 1.03 r_S$, where r_S is the initial Strömgren radius. Ideally, the saturation value should be $r = r_S$. This small overestimation of the IF position is due to a drawback of our method that the ionization of particle i located at r_i causes a decrease of the column densities over a range of $r = r_i - h_i \sim r_i + h_i$. Thus, the spatial resolution of the column density calculation in our method is at most of the order of h. Finally, we show the results of Test 2 in Fig. B6, which are also in good agreement with figs 11, 12, 13, 14 of Iliev et al. (2006).

APPENDIX C: RT IN OPTICALLY THICK MEDIUM

In optically thick medium, it becomes difficult to follow the propagation of an ionization front properly because the photoionization rates at the centres of SPH particles become very small although the incident radiation field is strong enough to ionize the SPH particles. In order to avoid this problem, Susa (2006) used volume-averaged photoionization rate instead of photoionization rate evaluated at the centre of an SPH particle. Following this, we use volume-averaged photoionization rate in the simulations in this study. In this study, the volume-averaged photoionization rate of H I, $\overline{k}_{\rm H\,I}(r)$, is calculated as follows:

$$\overline{k}_{\rm H\,I}(r) \equiv \frac{\int_{r-\Delta r/2}^{r+\Delta r/2} 4\pi r^2 k_{\rm H\,I}(r)\,{\rm d}r}{\int_{r-\Delta r/2}^{r+\Delta r/2} 4\pi r^2\,{\rm d}r}, \tag{C1}$$

$$= \frac{\int_{r-\Delta r/2}^{r+\Delta r/2} \left[\int_{\nu_{\rm L}}^{\infty} \frac{L_\nu {\rm e}^{-\tau_\nu}}{h\nu} n_{\rm H\,I}\sigma_{\rm abs}^{\rm H\,I}(\nu)\,{\rm d}\nu\right] {\rm d}r}{\int_{r-\Delta r/2}^{r+\Delta r/2} 4\pi r^2\,{\rm d}r}, \tag{C2}$$

$$\approx \frac{1}{1+\frac{1}{12}\left(\frac{\Delta r}{r}\right)^2} \times \frac{1}{2}\left[k_{\rm H\,I}(r-\Delta r/4) + k_{\rm H\,I}(r+\Delta r/4)\right], \tag{C3}$$

where we assumed that $n_{\rm H\,I}$ is constant over the interval of $[r - \Delta r/2,\ r + \Delta r/2]$ along a ray and used an approximate

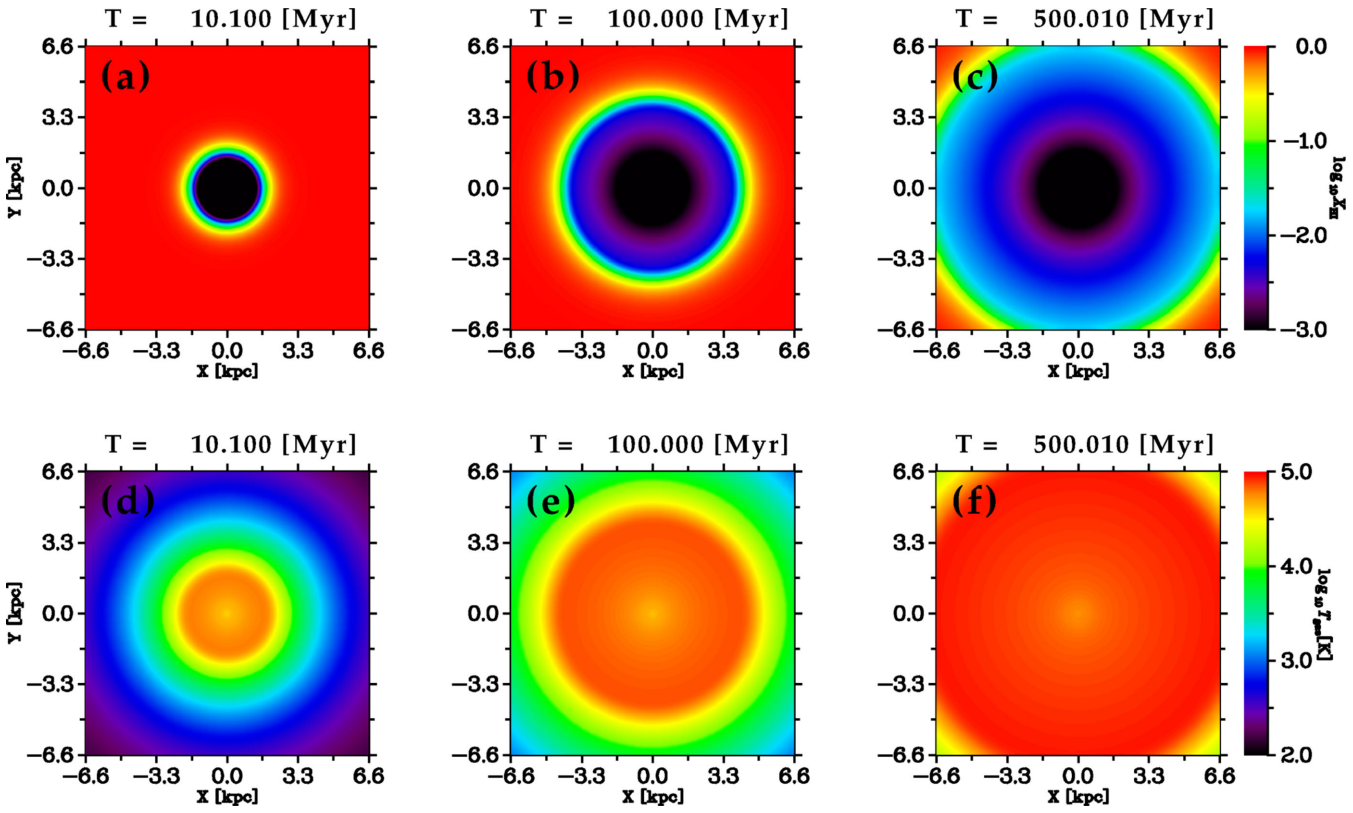

Figure B6. H I fraction (upper panels) and gas temperature (lower panels) at different times in Test 2 of Iliev et al. (2006). All the snapshots are slices at $z = 0$.

relation

$$\int_{r-\Delta r/2}^{r+\Delta r/2} \mathrm{e}^{-\tau_\nu} \mathrm{d}r \approx \frac{\Delta r}{2} \mathrm{e}^{-\tau_\nu (r=r-\frac{\Delta r}{4})} + \frac{\Delta r}{2} \mathrm{e}^{-\tau_\nu (r=r+\frac{\Delta r}{4})}. \quad \text{(C4)}$$

The photoheating rates and radiative accelerations (equations 28–33 and 36) are also evaluated in this method and we use $\Delta r_i = 2h_i$, where h_i is the smoothing length of SPH particle i. Note that this method is not photon-conservation scheme unlike the method in Susa (2006).[10]

[10] In order to make the method photon conservative, we have to calculate the integrals in equations (28)–(32) at each timestep.

This paper has been typeset from a TEX/LATEX file prepared by the author.